universität wien

MASTERARBEIT | MASTER'S THESIS

Titel | Title

The role of the enzymatic function of histone deacetylase 1 (HDAC1) in cutaneous lipid metabolism

verfasst von | submitted by

lic. Paula-Izabela Paşca

angestrebter akademischer Grad | in partial fulfilment of the requirements for the degree of

Master of Science (MSc)

Wien | Vienna, 2026

Studienkennzahl lt. Studienblatt | Degree programme code as it appears on the student record sheet:	UA 066 865
Studienrichtung lt. Studienblatt | Degree programme as it appears on the student record sheet:	Masterstudium Molecular Biology
Betreut von | Supervisor:	DI Dr. Heinz Fischer

ACKNOWLEDGEMENT

I would like to thank my supervisor Heinz Fischer for giving me the opportunity to work on this fascinating project and for his continuous support, patience, and guidance throughout my research and thesis writing. His mentorship has been very important in my development as a scientist, and I am grateful to have been part of his laboratory group.
I want to thank Christian Seiser for his support and encouragement, for sharing his extensive knowledge whenever I had technical or methodological questions, and for the ice cream breaks that made the long days more enjoyable.
I am deeply grateful to the entire Fischer/Seiser lab and for all of the other office and lab colleagues for providing such an inspiring and collaborative research environment. In particular, I want to thank Jelena Marjanovic, Sophie Wolfger, Justin Trowbridge, Magdalena Reif, Mary Crystal McFadden, and Anna Litwinschuh for their colleagueship, encouragement, and scientific discussions, which have made this experience both productive and enjoyable.
I thank the Törőcsik lab at the University of Debrecen for providing the early passage SZ95 sebocytes used in this study. I am also grateful for the technical support and collaboration provided by the Mouse Facility and Department of Dermatology at MUW, the MUW Genomics Core Facility, and the University of Heidelberg Lipidomics Facility.
I would like to express my deepest gratitude to my boyfriend Lukas Streibl, my sister, and my parents for always believing in me, for their unconditional love and support, and for enabling me to pursue this degree. And lastly, I want to thank my little furry friend Mocca for supervising me throughout the writing process of this thesis.

ABSTRACT

Sebaceous gland lipogenesis is regulated by the interplay of hormonal, metabolic, and epigenetic mechanisms, with the balance between histone acetylation and deacetylation at lipogenic gene promoters serving as a critical regulatory axis. Previous work in our lab demonstrated that class I histone deacetylase (HDAC) inhibition induces accumulation of neutral lipids and transcriptional upregulation of lipid-associated genes in human SZ95 sebocytes. However, the specific contribution of HDAC1 catalytic activity, as distinct from its structural and scaffolding functions within co-repressor complexes, remained unresolved. This study investigated the role of HDAC1 enzymatic activity in the epigenetic regulation of lipid metabolism in SZ95 sebocytes through three complementary approaches: pharmacological perturbation, genetic engineering, and chromatin-level profiling.

Combined treatment of SZ95 cells with insulin, the liver X receptor (LXR) agonist TO901317, and the class I HDAC inhibitor MS-275 (entinostat) produced the strongest induction of lipid droplet formation, as quantified by Oil Red O (ORO) staining, and upregulated the lipid-associated proteins sterol regulatory element-binding protein 1 (SREBP-1), stearoyl-CoA desaturase (SCD), and fatty acid synthase (FAS) at the protein level. The p300/CBP histone acetyltransferase inhibitor A-485 partially rescued the MS-275-induced lipid accumulation, reducing it to levels comparable to insulin+TO901317 treatment alone, thereby demonstrating that the enhanced lipogenesis driven by HDAC inhibition is dependent on p300 catalytic activity.

siRNA-mediated knockdown of HDAC1, HDAC2, and HDAC3 was validated at the protein level by Western blotting, revealing a reciprocal compensatory upregulation between HDAC1 and HDAC2 upon depletion of either paralog. Despite successful knockdown, ORO quantification showed only minor increases in lipid accumulation, and combined HDAC1+HDAC2 knockdown did not produce an additive effect. This blunted response could reflect a putative co-repressor complex-dependent mutual stabilization of HDAC1 and HDAC2, whereby loss of one paralog elevates the other, potentially through increased incorporation into Sin3, NuRD, and CoREST scaffolds, partially sustaining deacetylase activity.

To overcome these limitations, stable SZ95 cell lines expressing FLAG-tagged wild-type HDAC1 or the catalytically inactive HDAC1 H141A variant were generated via CRISPR/Cas9-mediated knock-in at the *AAVS1* safe-harbor locus. In total, 20 clones and subclones were produced, representing, to our knowledge, the first report of SZ95 sebocyte cell lines engineered to stably express a gene of interest. Transgene integration and expression were confirmed by FLAG immunofluorescence, nested PCR, and Sanger sequencing against the *Mus musculus* HDAC1 reference sequence (NCBI: NM_008228.3). Deacetylase activity assays on FLAG-immunoprecipitated samples demonstrated that WT clones retained robust enzymatic activity, while H141A clones displayed significant reduced but residual activity, consistent with the heterozygous nature of the system and co-immunoprecipitation of endogenous HDAC1 and HDAC2. Co-immunoprecipitation of Sin3A, CoREST, MTA2, and Sap30 with FLAG-HDAC1 H141A protein confirmed that the catalytic mutation preserves co-repressor complex assembly. Importantly, the compensatory HDAC2 upregulation observed upon siRNA-mediated HDAC1 knockdown was not triggered by expression of the catalytically inactive allele, demonstrating that this compensation is driven by loss of HDAC1 protein rather than loss of catalytic activity. Immunofluorescence staining for H2BK5ac and H3K27ac showed no global changes in histone acetylation between H141A and control clones, consistent with partial rather than complete reduction of HDAC1 activity. FAS protein levels increased upon insulin+TO901317 stimulation in H141A clones, with enhanced induction compared to FLAG-

negative controls, indicating that partial reduction of HDAC1 catalytic activity is sufficient to amplify the lipogenic transcriptional response.
CUT&RUN chromatin profiling using an antibody against H3K4me3, a histone mark associated with transcriptionally active promoters, was established in SZ95 sebocytes and revealed locus-specific changes in promoter-associated chromatin states under lipogenic stimulation. At the *SREBF1* locus, combination treatment induced a second H3K4me3-enriched region downstream of the constitutively active canonical *SREBP-1a* promoter, consistent with activation of the alternative LXR-responsive *SREBP-1c* promoter. At the *FASN* and *SCD* loci, H3K4me3 signal was enhanced above already active baselines, indicating further transcriptional activation. At the *ABCA1* locus, a sharp de novo H3K4me3 peak was induced from a near-absent baseline, representing the clearest example of treatment-dependent promoter activation. Three control loci (*DLX2*, *ZNF713*, *EOLA2*) displayed reduced H3K4me3 occupancy under treatment, confirming that the observed chromatin changes were locus-specific and not attributable to global chromatin remodeling.
These findings support a convergent epigenetic model in which HDAC1 catalytic activity normally restrains histone acetylation at lipogenic gene promoters in human sebocytes. Perturbation of this activity, whether through chemical inhibition, siRNA-mediated knockdown, or partial catalytic inactivation via the H141A allele, permits p300-dependent acetylation to persist at these loci, establishing a transcriptionally permissive chromatin state that supports activation of the SREBP-1 driven lipogenic program. This study positions HDAC1 as an epigenetic gatekeeper of sebaceous lipogenesis whose partial inactivation is sufficient to shift the balance toward a hyperacetylated, pro-lipogenic chromatin state at key regulatory loci, with potential relevance for the pathogenesis and future therapeutic targeting of sebaceous gland disorders such as acne vulgaris.

ZUSAMMENFASSUNG

Die Lipogenese in den Talgdrüsen wird durch das Zusammenspiel hormoneller, metabolischer und epigenetischer Mechanismen reguliert, wobei das Gleichgewicht zwischen Histonacetylierung und -deacetylierung an den Promotoren lipogener Gene als entscheidender Regulationsmechanismus fungiert. Frühere Arbeiten haben gezeigt, dass die Hemmung von Histon-Deacetylasen (HDAC) der Klasse I in menschlichen SZ95-Sebozyten eine Lipidakkumulation und eine transkriptionelle Hochregulation von Lipid-assoziierten Genen induziert. Der spezifische Beitrag der katalytischen Aktivität von HDAC1, im Unterschied zu seinen strukturellen und gerüstbildenden Funktionen innerhalb von Co-Repressor-Komplexen, blieb jedoch ungeklärt. Diese Studie untersuchte die Rolle der enzymatischen Aktivität von HDAC1 bei der epigenetischen Regulation des Lipidstoffwechsels in SZ95-Sebozyten anhand von drei sich ergänzenden Ansätzen: pharmakologische Intervention, gentechnische Manipulation und chromatinbasiertes Profiling.

Die kombinierte Behandlung von SZ95-Zellen mit Insulin, dem Leber-X-Rezeptor (LXR)-Agonisten TO901317 und dem Klasse-I-HDAC-Inhibitor MS-275 (Entinostat) führte zu einer starken Induktion der Lipidtröpfchenbildung, wie durch Oil-Red-O-Färbung (ORO) quantifiziert, und bewirkte eine Hochregulation der lipidassoziierten Proteine Sterol-Regulatory-Element-Binding-Protein 1 (SREBP-1), Stearoyl-CoA-Desaturase (SCD) sowie die Fettsäuresynthase (FAS) auf Proteinebene. Der p300/CBP-Histonacetyltransferase-Inhibitor A-485 konnte die durch MS-275 induzierte Lipidakkumulation teilweise aufheben und auf ein Niveau reduzieren, das mit der Behandlung mit Insulin + TO901317 allein vergleichbar war. Dies zeigt, dass die durch die HDAC-Inhibition verstärkte Lipogenese von der katalytischen Aktivität von p300 abhängig ist.

Der siRNA-vermittelte Knockdown von HDAC1, HDAC2 und HDAC3 wurde auf Proteinebene mittels Western Blot validiert, wobei sich nach Depletion eines der beiden Paraloge eine wechselseitige kompensatorische Hochregulation zwischen HDAC1 und HDAC2 zeigte. Trotz des erfolgreichen Knockdowns ergab die ORO-Quantifizierung nur geringfügige Anstiege der Lipidakkumulation, und der kombinierte Knockdown von HDAC1 und HDAC2 bewirkte keinem additiven Effekt. Diese abgeschwächte Reaktion könnte eine putative Co-Repressor-Komplex-abhängige gegenseitige Stabilisierung von HDAC1 und HDAC2 widerspiegeln, wobei der Verlust eines Paralogs zu einer Erhöhung des jeweils anderen führt, möglicherweise infolge einer verstärkten Integration in Sin3-, NuRD- und CoREST-Komplexe, wodurch die Deacetylase-Aktivität teilweise erhalten bleibt.

Um diese Einschränkungen zu überwinden, wurden stabile SZ95-Zelllinien generiert, die mittels CRISPR/Cas9 vermittelten Knock-in am *AAVS1* Safe Harbour Locus FLAG-getaggtes Wildtyp-HDAC1 beziehungsweise die katalytisch inaktive HDAC1-H141A-Variante exprimieren. Insgesamt wurden 20 Klone und Subklone erzeugt, was unseres Wissens die erste Beschreibung von SZ95-Sebozyten-Zelllinien darstellt, die so konstruiert wurden, dass sie ein bestimmtes Gen stabil exprimieren. Die Integration und Expression des Transgens wurden mittels FLAG-Immunfluoreszenz, Nested-PCR sowie Sanger-Sequenzierung anhand der Mus musculus HDAC1-Referenzsequenz (NCBI: NM_008228.3) bestätigt. Deacetylase-Aktivitätstests an FLAG-immunpräzipitierten Proben zeigten, dass HDAC1WT-Klone eine robuste enzymatische Aktivität beibehielten, während HDAC1H141A-Klone eine deutlich reduzierte, aber verbleibende Aktivität aufwiesen, was mit der heterozygoten Natur des Systems und der Co-Immunpräzipitation von endogenem HDAC1 und HDAC2 erklärbar ist. Die Co-Immunpräzipitation von Sin3A, CoREST, MTA2 und Sap30 mit dem FLAG-H141A-Protein bestätigte, dass die katalytische Mutation die Assemblierung beziehungsweise strukturelle

Integrität der Co-Repressor-Komplexe nicht beeinträchtigt. Entscheidend ist, dass die kompensatorische HDAC2-Hochregulation, die bei siRNA-vermitteltem HDAC1-Knockdown beobachtet wurde, nicht durch die Expression des katalytisch inaktiven Allels ausgelöst wurde, was zeigt, dass diese Kompensation durch den Verlust des HDAC1-Proteins und nicht durch den Verlust der katalytischen Aktivität bedingt ist. Die Immunfluoreszenzfärbung für H2BK5ac und H3K27ac zeigte keine globalen Unterschiede in der Histonacetylierung zwischen den H141A- und den Kontrollklonen, was mit einer teilweisen, jedoch nicht vollständigen Reduktion der HDAC1-Aktivität vereinbar ist. Die FAS-Proteinkonzentrationen stiegen nach Stimulation mit Insulin+TO901317 in den HDAC1H141A-Klonen an, wobei die Induktion im Vergleich zu FLAG-negativen Kontrollen verstärkt war. Dies deutet darauf hin, dass bereits eine teilweise Reduktion der katalytischen Aktivität von HDAC1 ausreicht, um die lipogene Transkriptionsreaktion zu verstärken.
Zur Etablierung der Chromatinprofilierung mittels CUT&RUN wurde ein Antikörper gegen H3K4me3 verwendet, eine Histonemarkierung transkriptionell aktiven Promotoren. Dabei zeigte sich, dass es in SZ95-Sebozyten nach lipogener Stimulation es zu lokusspezifischen Veränderungen der Promotor-assoziierten Chromatinzustände kommt. Am *SREBF1*-Locus führte die Kombinationsbehandlung mit Insulin, TO901317 und MS-275 zu Ausbildung einer zweiten H3K4me3-angereicherte Region des konstitutiv aktiven kanonischen *SREBP-1a*-Promotors, was mit der Aktivierung des alternativen LXR-responsiven *SREBP-1c*-Promotors vereinbar ist. An den *FASN*- und *SCD1*-Loci war das H3K4me3-Signal über die bereits aktiven Ausgangswerte hinaus verstärkt, was auf eine weitere transkriptionelle Aktivierung hindeutet. Am *ABCA1*-Locus führte die Behandlung zur ausgeprägten *de novo* H3K4me3- Peaks ausgehend von einer nahezu nicht vorhandenen Ausgangsbasis, was das deutlichste Beispiel für eine behandlungsabhängige Promotoraktivierung darstellt. Drei Kontroll-loci (*DLX2*, *ZNF713*, *EOLA2*) zeigten unter der Behandlung eine verringerte H3K4me3-Belegung, was bestätigt, dass die beobachteten Chromatinveränderungen lokusspezifisch waren und nicht auf eine globale Chromatin-Umgestaltung zurückzuführen sind.
Diese Ergebnisse stützen ein konvergentes epigenetisches Modell, wonach die katalytische Aktivität von HDAC1 normalerweise die Histonacetylierung an den Promotoren lipogener Gene in menschlichen Sebozyten hemmt. Eine Störung dieser Aktivität – sei es durch chemische Inhibition, siRNA-vermittelten Knockdown oder partielle katalytische Inaktivierung über das H141A-Allel – ermöglicht das Fortbestehen der p300-abhängige Acetylierung an diesen Loci und begünstigt dadurch die Ausbildung eines transkriptionell permissiver Chromatinzustand, der die Aktivierung des SREBP-1-gesteuerten lipogenen Programms unterstützt. Diese Studie positioniert HDAC1 als epigenetischen Gatekeeper der TalgdrüsenlLipogenese, dessen partielle Inaktivierung ausreicht, um das Gleichgewicht an wichtigen regulatorischen Loci zugunsten eines hyperacetylierten, pro-lipogenen Chromatinzustand zu verschieben. Dies weist auf eine potenzielle Relevanz für die Pathogenese sowie zukünftige therapeutische Strategien bei Talgdrüsenerkrankungen wie Akne vulgaris hin.

CONTENTS

LIST OF FIGURES

LIST OF TABLES

1 INTRODUCTION

1.1 Epigenetics

A fundamental challenge in biology is explaining how a multicellular organism develops a wide variety of cell types, each exhibiting unique functions, and possessing different, yet stable, profiles of gene expression even though all the cells in the organism contain essentially the same sequences of DNA [1–3]. Chromosome studies have shown that all somatic cells retained the full complement of DNA present in the fertilized egg, however, a liver cell is functionally and morphologically distinct from a neuron or a lymphocyte [2,4]. This cellular differentiation doesn't appear due to changes in the static sequence of the double helix that carries the code of life, but rather from the chemical and molecular changes affecting gene expression levels, heritable information that dictates which genes are expressed and which are silenced [1,2,5]. The study of these regulatory mechanisms is known as epigenetics, a term derived from the Greek prefix "epi-," meaning "above" or "beyond" genetics, referring to processes beyond DNA sequence changes [4,6].

The term 'epigenetics' was first used in 1942 by the British developmental biologist, embryologist, and geneticist Conrad H. Waddington [1,3,7]. Waddington originally defined epigenetics as "the branch of biology which studies the causal interactions between genes and their products, which bring the phenotype into being" [1,7]. Over the years, as research progressed and it became clear that the DNA in differentiated cells remains largely unchanged, the definition evolved to emphasize the heritability of gene expression states [1,4]. Today, a widely accepted working definition of epigenetics, described as "the study of mitotically and/or meiotically heritable changes in gene function that cannot be explained by changes in DNA sequence" [2,4–6]. Molecularly, epigenetics had been described as "the sum of the alterations to the chromatin template that collectively establish and propagate different patterns of gene expression (transcription) and silencing from the same genome" [6]. It is important to note that some definitions of epigenetics are broader and do not necessarily require heritability, such as that by the US National Institutes of Health (2009-http://nihroadmap.nih.gov/epigenomics/) stating that 'epigenetics refers to both heritable changes in gene activity and expression (in the progeny of cells or of individuals) and also stable, long-term, alterations in the transcriptional potential of a cell that are not necessarily heritable[1,2,5].

Regardless of the exact definition, the establishment and maintenance of these processes that stably alter gene expression patterns are controlled by a complex interplay of mechanisms [5,8]. These including non-coding RNAs (lncRNA, piRNA, siRNA, miRNA), structural protein templating (prions), and chromatin modifications such as DNA methylation and histone modification[1–3,9]. Together, these mechanisms organize the genome, regulate its accessibility, and provide cellular memory that can be inherited through cell division [2,5].

1.2 Chromatin structure

In eukaryotic nuclei, the genome exists as a protein-DNA complex known as chromatin [10]. This structure does not only facilitate compaction of DNA so that it fits within the nucleus, but also regulates access to genetic information, influencing essential DNA-dependent processes such as transcription, repair, replication, and recombination [10,11]. Chromatin organization is a hierarchical and dynamic process, that starts with its fundamental unit called nucleosome, progressing to higher-order compaction levels, ultimately culminating with chromosome formation, visible during cell division [10,11].

A nucleosome comprises approximately 146–147 base pairs of DNA wrapped in about 1.75 left-handed super-helical turns around a histone octamer [10,11]. This octamer consists of two copies each of the core histone proteins H2A, H2B, H3, and H4 [11]. Structurally, the octamer is organized with a central $(H3\text{-}H4)_2$ tetramer flanked by two H2A-H2B dimers [12]. Histones are small proteins that are classically less than 150 amino acids in length, and 11–15 kDa in size, containing many positively charged amino acids (such as lysine and arginine) that facilitate strong electrostatic interactions with the negatively charged phosphate backbone of DNA [12,13]. Nucleosome assembly is a multistep process initiated by the binding of the $(H3\text{-}H4)_2$ tetramer to DNA, followed by the recruitment of two H2A-H2B dimers, creating a stable nucleoprotein complex essential for chromatin organization and regulation [11].

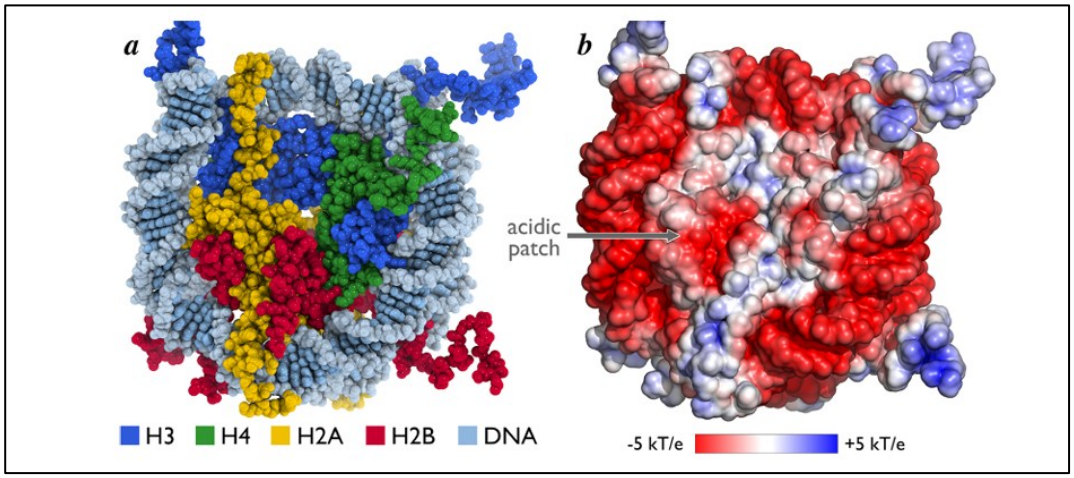

Figure 1: Surface topology and charge of the nucleosome core particle.

(a) Surface of nucleosome core particle viewed down the DNA superhelical axis in space-filling representation. (b) Surface electrostatic potential of nucleosome core particle contoured from−5 to +5 kT/e calculated with ABPS.164 Location of acidic patch is indicate (figure from [14])

Nucleosomes are connected by segments of linker DNA, forming the characteristic "beads-on-a-string" 10 nm chromatin fiber [12,15,16]. In the past, it was suggested that the 10 nm fibers are subsequently folded into a denser structure referred to as 30 nm fibers, for which several models have been proposed, such as the solenoid or zig-zag [11]. However, the existence of a stable 30 nm fiber in living cells remains a debated topic, with recent studies suggesting that chromatin fibers in vivo are more irregular and dynamic, displaying a range of diameters and forming local clusters of short nucleosome stretches or even phase-separated chromatin droplets [10,15,16]. A fifth histone (linker histone H1) binds at the entry and exit sites of DNA on the nucleosome, stabilizing higher-order chromatin architecture and contributing to further compaction [12,15]. This architectural variability enables rapid and context-dependent chromatin remodeling and contributes to diverse regulatory outcomes [11,16]. Chromatin self-associates and condenses into tertiary and quaternary structures, forming chromosomes—extremely

condensed structures that become visible during cell division, allowing precise segregation of genetic material [10].

Chromatin spatial organization and interactions include the identification of global contact similarities (compartments A/B—active/inactive) and local contact insulation (topologically-associated domains or TADs) [11].

Furthermore, nuclear rigidity is influenced by the two different states of chromatin: heterochromatin and euchromatin [11]. Heterochromatin consists of tightly packed nucleosomes that restrict access to DNA, making these regions transcriptionally inert, while euchromatin is loosely packed and therefore more accessible, being mainly associated with transcriptional activity [11,17]. In proliferating cells, the condensation level changes throughout cell cycle progression, with chromatin being loosely packed during interphase and maximally condensed during mitosis [11,12]. However, there are some chromatin regions that remain highly condensed and transcriptionally inactive throughout the entire cell cycle, called constitutive heterochromatin [11,17]. This type of chromatin functions as a silencer in pericentromeric regions and at telomeres—gene-poor areas usually made up of tandem repetitions, ensuring genomic stability [17].

Within the nucleosome structure, certain regions are functionally distinct based on the strength of their DNA-histone contacts: histone tails, DNA entry/exit region, dyad symmetry axis region, and interfaces between histone dimers [18]. Histone tails extend out from the nucleosome core and help stabilize higher-order chromatin structure [18]. DNA entry/exit region are located at the edges of the nucleosome, this region is not strongly bound to the histone surface, leading it to be the first area to detach during processes like nucleosome sliding or unwrapping [18]. The dyad symmetry axis represents the most internal segment of DNA wrap where the strongest DNA-histone interactions occur [18]. The histone-histone interfaces represent protein-protein contact points, such as those between the H3/H4 tetramer and H2A/H2B dimers, which are essential for maintaining the integrity of the octameric core [18].

The acidic patch is a specific structural feature located on the surface of the disk-like body of a nucleosome [19]. It is formed by the association of histones H2A and H2B [19]. This region serves as a critical docking site for various protein interaction modules and chromatin-modifying complexes [19]. Engaging the nucleosome via the acidic patch is a common mechanism used by many different and unrelated nucleosome-interacting factors and chromatin-modifying machines to gain access to their substrates [19].

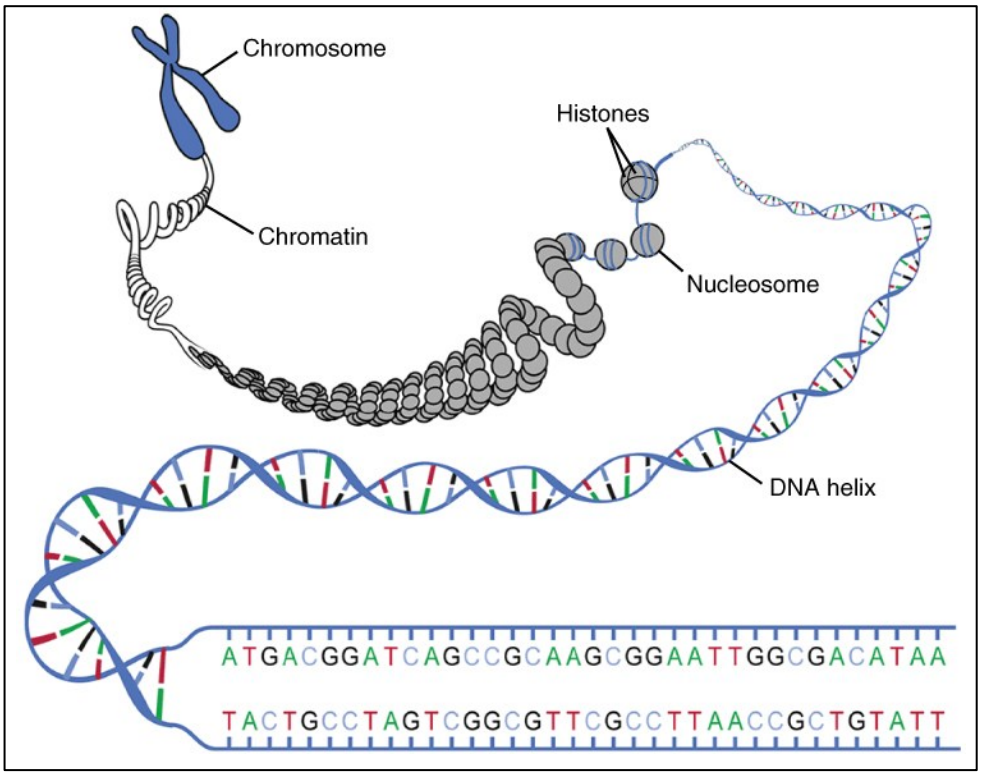

Figure 2: DNA Macrostructure

Strands of DNA are wrapped around supporting histones. These proteins are increasingly bundled and condensed into chromatin, which is packed tightly into chromosomes when the cell is ready to divide (figure from [20]).

1.3 Histones

Histones are positively charged small globular proteins that are highly conserved among all eukaryotes reflecting their fundamental role in genome organization [13,21]. There functions are very important and can be separated in 2 different types: packaging the genomic DNA and regulating gene accessibility [21]. This class of proteins contains 4 core histones: H2A, H2B, H3, and H4, and one linker histone H1 [13,22].

Core histones have around 10-15kDa in size and are classically less than 150 amino acids in length [13]. They are composed of three distinct structural elements: the basic surface, the Histone fold motif, the C- and N-terminal tails [13,23]. The overall surface of the histone protein is curved and highly positively charged (basic), because of the numerous arginine and lysine side chains [18,24]. These positively charged residues are allowing histones to neutralize the negatively charged phosphate backbone of DNA through extensive electrostatic and hydrogen-bonding interactions [13,18,24]. This enables the DNA to bend and wrap tightly around the protein core, each histone dimer coordinating three consecutive minor grooves on the inner surface of the DNA spiral, resulting in its specific bent conformation that allows the nucleosome stabilization [13,18,24].

The 'histone-fold' domain is a well conserved structural motif consisting of three α-helices that is involved in histone-histone interactions within the nucleosome core, helping to form the octameric structure around which the DNA is wrapped [13,23].

The N-terminal and C-terminal tails are unstructured, flexible, and disordered strings of amino acids that protrude from the nucleosome core, with the tail mass accounting for approximately 25% of the total histone mass [13,22,25]. Because of this, they are accessible to enzymes involved in numerous covalent PTMs [13,25]. The PTMs do not change DNA sequence but, changes the histone interaction with the DNA and serve as "docking station" for nuclear

proteins that can change expression and function levels [25,26]. These modifications include methylation, acetylation, phosphorylation, glycosylation, carbonylation, ubiquitylation, biotinylation, sumoylation, citrullination, ADP-ribosylation, N-formylation, crotonylation, propionylation, and butyrylation, as well as proline and aspartic acid isomerization.[25]
From a chemical perspective, the primary amino acids that form the functional landscape of histones (specifically serving as sites for PTM) are lysine (K), arginine (R), serine (S), threonine (T), and tyrosine (Y)[23,26,27].
Cells can replace standard "canonical" histones with histone variants (such as H2A.Z or CENP-A) that are changing multiple histone−DNA and histone−histone contacts simultaneously and are altering characteristics of single nucleosomes and chromatin fibers[18].
Additionally, histones exhibit site exposure, a dynamic behavior where the DNA spontaneously unwraps and rewraps from the protein core [18]. This "breathing" allows the cell to regulate access to the genetic code in a tunable, analog fashion rather than just being a simple binary on/off switch [18].

1.4 Epigenetic mechanisms

The epigenetic mechanisms represent a complex network of processes that influence gene expression without modifying the nucleotide sequence [4,6,12,15]. The four main epigenetic mechanisms are DNA methylation, histone modifications, chromatin remodeling complexes, and RNA-based mechanisms [2,12,16].
DNA methylation is a reversible covalent modification of the DNA and one of the best characterized epigenetic modifications [2,4,16,17]. It consists of the addition of a methyl group (-CH3) preferentially at the fifth carbon of a cytosine within CpG dinucleotides in mammals [1,15,17]. Genomic regions rich in CpG are known as CpG islands and are located near promoter regions, making them important transcriptional regulators [2,4,16]. Generally, this modification is associated with transcriptional repression (gene silencing) and is catalyzed by the enzymes called DNA methyltransferases (DNMTs), DNMT1 being essential for maintaining the methylation, and DNMT3a and DNMT3b are responsible for de novo methylation [1,4,15,17].
The histone modifications involve post-translational modifications (PTMs) of histone proteins, which include chemical alterations such as acetylation, methylation, phosphorylation, ubiquitination, and sumoylation [2,3,16,17], thereby influencing the degree of chromatin condensation and the binding of regulatory proteins [5]. These modifications predominantly occur on lysine (K) and arginine (R) residues present on the amino-terminal tails of histones, which protrude from the nucleosome core [2,4,15].
RNA-based mechanisms are based on non-coding RNAs (ncRNAs), which are transcripts that are not translated into proteins [1,2,16]. The ncRNAs have a critical role in epigenetic gene regulation, inducing gene silencing by collaborating with chromatin modifying enzymes and DNA methylation machinery [1,2,15]. In this category are included short RNAs such as microRNAs (miRNAs) and short interfering RNAs (siRNAs), as well as long non-coding RNAs (lncRNAs) like Xist RNA [1,2].
Chromatin remodeling complexes are non-covalent modifications that use the energy from ATP hydrolysis to produce dynamic changes in the chromatin structure [1–3]. Chromatin remodeling complexes are divided into four families, the SNF2H or ISWI family, the Brahma or SWI/SNF family, the IN080 family, and the chromodomain-helicase-DNA binding family [1,4,6].
The SNF2H/ISWI complexes act by mobilizing nucleosomes along the DNA [2], whereas the Brahma/SWI/SNF complexes transiently alter the structure of nucleosomes, thus exposing the DNA-histone contacts [2]. Chromatin remodelers can catalyze a wide variety of chromatin

structural changes, some promoting the replacement of conventional core histones with variant forms, thus acting as 'exchanger complexes' [1,2].
The incorporation of these non-canonical histone variants introduces a supplementary variation to the chromatin, contributing to the regulation of chromatin accessibility (H3.3 and H2A.Z), maintaining the active state of the chromatin (H3.3) [4,17], conferring resistance in the inactive regions (mH2A) [4].
These molecular mechanisms work together to introduce meaningful variation into the chromatin fiber and propagate different patterns of gene expression and silencing within the same genome [1,2,4].

1.4.1 Histone post-translational modification (PTMs)

PTMs are reversible chemical modifications that occur on histones after they have been translated into proteins [22,25].
The various PTMs are deposited mostly on lysine (K), arginine (R), threonine (T), glycine (G), and alanine (A) residues of the N-terminal and C-terminal tails, but also within the histone-fold region [13]. At the moment, at least fifteen types of PTMs have been identified at 130 different sites on core and linker histones, with some modifications being more stable like methylation, and with others that are being more dynamic like acetylation, ubiquitination, and phosphorylation [25,28].
The diversified epigenetic modification of the histone amino-terminal expands the genetic code and is it called the 'Histone Code' [28]. They are forming a set of chemical tags that are determines the transcriptional status of genomic regions by modulating chromatin structure and DNA accessibility and serve as signalling platforms for various nuclear proteins.[22,28].
The histone code is highly dynamic, allowing a rapid adaptation to environmental changes, thanks to three classes of protein modules that establish (Writers), interpret (Readers), and remove (Erasers) the chemical marks [13,25]. Writers add functional groups to histones, erasers remove them, and readers recognize PTMs serving as anchors between PTMs and associated proteins, such as transcription factors, activators, repressors, or other proteins involved in the modulation of chromatin status [13]. The changes of the histone PTMs alters their chemical properties and interactions with DNA and other histones, thereby dynamically modulating chromatin state through the coordinated action of writers, erasers, and readers [13].
Methylation of histones is relatively stable, having the half-lives ranging from several hours to days one of the stable and most studied PTMs, appearing on amino acid residues such as lysine, arginine, glutamine, aspartic acid and proline [22,25]. Unlike other modification, methylation does not change the charge of the histone, it influences chromatin folding via an electrostatic mechanism, and because of this it can be a mark for both activation and repression, depending on the site and degree [22,25]. For example, H3K4me1-2-3 is typically found at active transcription sites, whereas H3K9me2-3 and H3K27me3 are marks for constitutive heterochromatin and facultative heterochromatin, [13,22]. The attachment of methyl groups is carried out by methyltransferases and the removal by demethylase enzyme groups[13,22,25].
Phosphorylation is a highly dynamic modification that can occur mainly on serine, threonine, tyrosine residues, as well is sites such as arginine, histidine and lysine but much less studied [22,25]. Phosphate groups are added to and removed from the target histone residue by histone kinases and phosphatases respectively [25]. The phosphate group introduces a negative charge which can affect electrostatic interactions within chromatin and inducing changes in the chromatin structure [22,25]. Histone phosphorylations play important roles in chromatin-related

processes including mitosis (H3S10, S28), meiosis and the DNA damage response (H4S1, H2A.XS139), and apoptosis (H2BS10), as well as gene expression (H3S10, T11) [22,25].

1.4.1.1 Histone acetylation

Histone acetylation of lysine residue was first described by Vincent Allfrey and co-workers in 1964 [19]. The predominant acetylation sites are lysine 5 and 9 of histone H2A; lysine 5, 12, 15, and 20 of histone H2B; 9, 14, 18, and 23 of histone H3; and lysine 5, 8, 12, 16, and 20 of histone H4 [25]. Generally, histone acetylation is associated with active region because the acetyl groups (COCH3) is neutralizing the positive charge of lysine and causing the release of the histone tails from the linker DNA, leading to chromatin relaxation, and ultimately facilitating the access of transcription factors, co-factors, and RNA polymerase II-complexes to access the DNA [19,25]. This process can be influenced by other PTMs, for example, H3S10 phosphorylation can stimulate acetylation of histone H4K14 supporting transcription activity [25]. This process is regulated by two opposing classes of enzymes: Histone Acetyltransferases (HATs) and Histone Deacetylases (HDACs), which function as writers and erasers of acetyl groups on the N-terminal tails of core histones [29].

Acetyl-Coenzyme A (Acetyl-CoA) is the main acetyl donor (substrate), transferring acetyl groups to lysine residues of histone or non-histone proteins through HATs, Coenzyme A (CoA) being released as a byproduct [30]. Acetyl-CoA generated through multiple metabolic pathways, including glycolysis, fatty acid β-oxidation, and amino acid catabolism, and nuclear ATP-citrate lyase-mediated acetyl-CoA synthesis is essential for histone acetylation in pluripotent stem cells [30]. Acetyl-CoA production is tightly linked to nutrient availability, metabolic status having a major influence on chromatin acetylation: high levels of nutrient substrates such as glucose and glutamine affect acetyl-CoA synthesis, whereas AMP-activated protein kinase (AMPK) signaling regulates histone deacetylase (HDAC) activity through HDAC phosphorylation [30].

HATs, known as “writers” of acetyl marks, catalyze the transfer of acetyl groups to lysine residues on histone tails [19,31]. They are multiprotein complexes, evolutionarily conserved from yeast to human and organized into three major families based on their catalytic domains and structural characteristics: the GNAT, MYST, and p300/CBP families [30,32,33]. The GNAT (named after the founding member: Gcn5 N-acetyltransferase) family primarily targets histone substrates and includes Gcn5, PCAF, Hat1, Elp3, and Hpa2 [30,32,33]. The MYST family (named after the founding members: Morf-Ybf2-Sas2-Tip60) preferentially acetylates histone H4 and includes Esa1, MOF, Sas2, Sas3, MORF, Tip60, and Hbo1 [30,32,33]. The third family, p300/CBP, includes CREB binding protein (CBP) and p300, both of which acetylate histones H3 and H4 [30,32,33]. In addition to HATs with conserved domains, other proteins such as Taf1 and certain nuclear receptor coactivators also exhibit HAT activity [30,32,33]. HATs take advantage of their associated proteins for recruitment to specific genomic loci, ensuring precise substrate selection and contextual regulation [32]. At the molecular level, p300, coordinates transcriptional regulation through histone modification and acts as a coactivator for various signaling pathways, influencing processes like lipogenesis, gluconeogenesis, and insulin regulation [34].

Bromodomains are evolutionarily conserved structural motifs, and the only known specialized “readers” that recognize and bind to acetylated lysine marks on histone tails and transcribed proteins [30]. They are found in 46 human proteins, including even some HATs like Gcn5, PCAF, p300 and CBP [35,36]. Bromodomains are essential components of the HATs, creating a link between the recognition of the acetylation marks and the “writing” of new ones [36]. Their presence allows HAT complexes to be recruited to nucleosomes that are already acetylated, anchoring the complex to the acetylated chromatin [35–37]. This anchoring is essential for the stability of the complex at specific genomic locations, such as promoters

and enhancers, where the HAT subunit acetylates adjacent nucleosomes, converting chromatin into an open state [19,35,36].

1.5 Histone deacetylation

Histone deacetylation is a dynamic and reversible PTM that is catalyzed by HDACs, enzymes that remove acetyl groups from 1-N-acetyl lysine amino acids on histones [29,37]. The positive charge on lysine side chains is restored, returning the histone to its basal state, enhancing electrostatic interactions between histone tails and the negatively charged DNA phosphate backbone [19,29]. As a result, chromatin gets a more condensed configuration, which restricts transcriptional machinery access and leading to gene suppression in most cases [19,29]. In higher eukaryotes, most genomic regions are maintained in a hypoacetylated, inactive chromatin, transcriptionally silent ground state, while acetylation of histones across broad chromatin domains leads to activation of housekeeping and cell-type-specific genes in response to developmental and environmental signals [37].

In total, eighteen HDACs have been identified in mammals and based on developmental genetics, sequence homology to yeast deacetylases and cofactor dependence have been grouped into the following four classes: class I (HDAC1, HDAC2, HDAC3, and HDAC8); class II, which is further divided into two subclasses: IIa (HDAC4, HDAC5, HDAC7, and HDAC9) and IIb (HDAC6 and HDAC10); class III (SIRT1, SIRT2, SIRT3, SIRT4, SIRT5, SIRT6, and SIRT7); and class IV (HDAC11) [31,33,38,39]. Classes I, II, and IV are Zn^{+}-dependent protein deacetylases, whereas class III enzymes are NAD^{+}-dependent deacetylases [30,33].

Class I HDACs, homologous to yeast protein reduced potassium dependency 3 (Rpd3), are composed of an entirely conserved deacetylase domain and have minimal N- and C- terminal domains [31,40]. All of the enzymes in this class contain a highly conserved deacetylase domain and share extensive homology with each other, with 45%-94% amino acid sequence identity [40]. The enzymes are ubiquitously expressed across mammalian tissues and cell lines [29,31], are predominantly located in the nucleus and contribute to cell development and differentiation (especially in neurogenesis), and exhibit strong histone deacetylase activity [31,33].

Class II HDACs, share high homology with yeast HDAC1 deacetylase and contain conserved catalytic domains similar to those of class I human HDACs, that share 23%-81% amino acid sequence identity to each other. [29,40]. They possess *in vitro* HDAC activity, although at a much lower level compared with class I HDACs [40].The class is further divided into Class IIa, which shuttle between the nucleus and cytoplasm, and Class IIb that are mainly cytoplasmic [31–33]. The subdivided class IIa HDACs contain a unique adapter domain in the N-terminus that forms a binding site for the DNA-binding transcription factor MEF2, and subsequent 3-4 phosphorylation sites that act as regulatory signals for the association of 14-3-3 proteins, which can shuttle between the cytoplasm and nucleus in response to various regulatory signals [31]. HDAC9 has multiple alternatively spliced isoforms. One of these isoforms, an amino-terminal splice variant, is the myocyte enhancer-binding factor 2-interacting transcriptional repressor (MITR)[40]. Class IIb HDACs exhibit a characteristic long extra extension at the C-terminus, known as a tail domain, and contain each a unique second catalytic domain not found in other HDACs: HDAC6 contains two deacetylase domains, which appear to function independently of each other, and a C-terminal zinc finger ubiquitin-binding domain. HDAC10 has only one deacetylase domain and a leucine-rich repeat domain at its C-terminus[31,40].

Class III HDACs comprise the sirtuin family and are located in the nucleus (SIRT1, SIRT2, SIRT3, SIRT6, and SIRT7), cytoplasm (SIRT1 and SIRT2), or mitochondria (SIRT3, SIRT4, and SIRT5).They act primarily on non-histones proteins linking deacetylation to cellular metabolic

status, energy sensing, and stress responses [31,32]. They are homologous to the yeast silent information regulator 2 (Sir2) required for transcription silencing, sharing 22%–50% overall amino acid sequence identity with each other, and 27%–88% identity in the conserved catalytic domains, and are widely conserved proteins in many organisms from bacteria to humans [31]. A distinct characteristic of class III HDACs is the deoxyhypusine synthase-like NAD/FAD-binding domain and the display of two enzymatic activities: mono-ADP-ribosyltransferase and histone deacetylase [31,40]. SIRT1 possesses the most robust histone deacetylase activity and SIRT5 possesses additional protein lysine desuccinylase and demalonylase activity *in vitro* [40].

Class IV HDACs are homologous to yeast Hos3 and shares homologous catalytic domain with both Class I and II HDAC enzymes [31]. HDAC11 regulates the protein stability of DNA replication factor CDT1 and the expression of interleukin 10 [31,40].

A big part of the HDACs functions not as independent enzymes, but as catalytic subunits within large multiprotein corepressor complexes such as Sin3, SMRT, NuRD, N-CoR, CoREST, MiDAC and others that are mentioned in **Table 1** [31,40]. These assemblies provide scaffolding modules for chromatin targeting, substrate recognition, and integration with other epigenetic regulators. [31]

HDAC Class	Enzyme	Associated Multi-Protein Complexes	Subcellular Localization
Class I	HDAC1	Sin3 , NuRD , CoREST, MiDAC, NODE, PRC2, SHIP1, BHC, CHRASCH, ZEB1/CtBP2	Nucleus
	HDAC2	Sin3 , NuRD , CoREST, SHIP1, MiDAC, NODE, PRC2, BHC	Nucleus
	HDAC3	SMRT/N-CoR	Nucleus and Cytoplasm
	HDAC8	Functions independently	Nucleus
Class IIa	HDAC4	NCOR1/NCOR2, SMRT/N-CoR-HDAC3 complex	Nucleus and Cytoplasm
	HDAC5	SMRT/N-CoR-HDAC3 complex	Nucleus and Cytoplasm
	HDAC7	SMRT/N-CoR-HDAC3 complex	Nucleus and Cytoplasm

	HDAC9	SMRT/N-CoR-HDAC3 complex	Nucleus and Cytoplasm
Class IIb	HDAC6	Can form complexes with HDAC11	Nucleus and Cytoplasm
	HDAC10	NCOR2	Nucleus and Cytoplasm
Class III	SIRT1	eNoSC	Nucleus and Cytoplasm
	SIRT2	-	Nucleus and Cytoplasm
	SIRT3	FoxO3A	Mitochondria
	SIRT4	-	Mitochondria
	SIRT5	-	Nucleus, Cytoplasm and Mitochondria
	SIRT6	-	Nucleas and endoplasmic reticulum
	SIRT7	-	Nucleus and Cytoplasm
Class IV	HDAC11	Can form complexes with HDAC6	Nucleus

Table 1: HDAC families, the multi-subunit complexes they associate with, and their primary subcellular localizations

(information form [19,31,41–46])

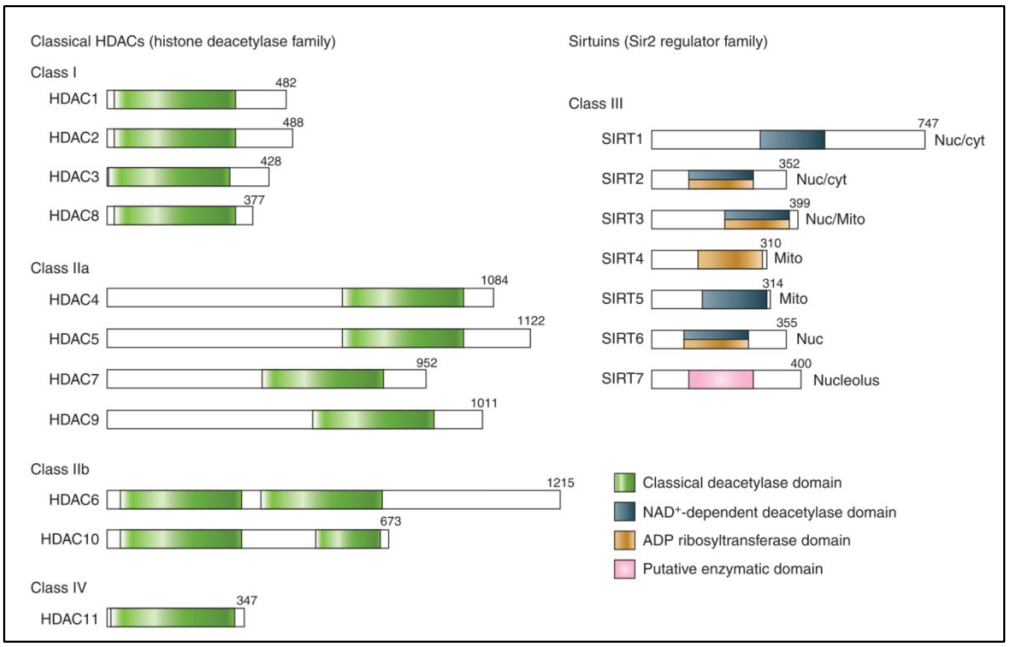

Figure 3: Domain organization of human HDACs.

The total number of amino acid residues in each HDAC is shown on the right of each protein. Many HDACs have multiple isoforms and, for simplicity, only the longest isoform is shown. Enzymatic domains (or putative enzymatic domains) are shown in colors. Sirtuin localizations: Nuc- nuclear; cyt- cytoplasmic; Mito- mitochondrial (figure from [45]).

1.5.1 Class I HDACs-with focus of HDAC1 and HDAC2

The classical HDAC families of enzymes (Class I, II, IV) all possess a highly homologues core structural domain known as the HDAC structural domain, which includes two highly conserved regions: the HDAC N-terminal and the HDAC central structural domains [40,45]. The domains contain catalytic sites that are essential for their enzymatic activity, like Zn^{2+} ions and arginine residues [40,45]. The C-terminal domain is the one that differs in length and amino acid sequences across different HDAC types [45].

HDACs 1, 2, 3, and 8 are the class I HDACs, being part from this category because of the high degree of conservation of the catalytic domains when compared to the catalytic domain found in yeast Rpd3, ranging between 40% and 70% [45]. Their catalytic domain is composed of approximately 400 amino acid residues, with the enzyme's structure being anchored by a core that includes eight parallel β-strands organized into a β-sheet, flanked by over thirteen α-helices and extended loops expanding from the C-terminus of the β-sheet, and creating an arraignment of a hydrophobic channel [44,45]. This channel represents the binding site for the substrate, with an active pocket that forms a chelate complex with the Zn^{2+} ion using highly conserved amino acid residues: His140, His141, Asp176, Asp264 in HDAC1, and His141, His142, Asp177, Asp265 in HDAC2 [44,45]. In this state the Zn^{2+} ion is also bonded to two water molecules, completing its coordination sphere [31,44,45]. When an acetylated lysine substrate inserts its side chain into the channel, its carbonyl oxygen replaces a coordinated water molecule and binds directly to the Zn^{2+} ion, which polarizes the carbonyl group for easier chemical attack [31,44,45]. Structural orientation is provided by a conserved tyrosine residue that forms hydrogen bonds with the carbonyl oxygen to fix the substrate in the correct position [31,45]. The actual deacetylation is driven by a His-Asp charge-relay system that activates the remaining water molecule into a reactive hydroxide nucleophile, which then attacks the polarized carbonyl carbon [31,44,45]. This leads to the formation of a high-energy tetrahedral intermediate stabilized by the Zn^{2+} ion, followed by the cleavage of the C-N bond and the

ultimate release of the acetate moiety and the deacetylated lysine that gets its positive charge back (**Figure 4**) [45].

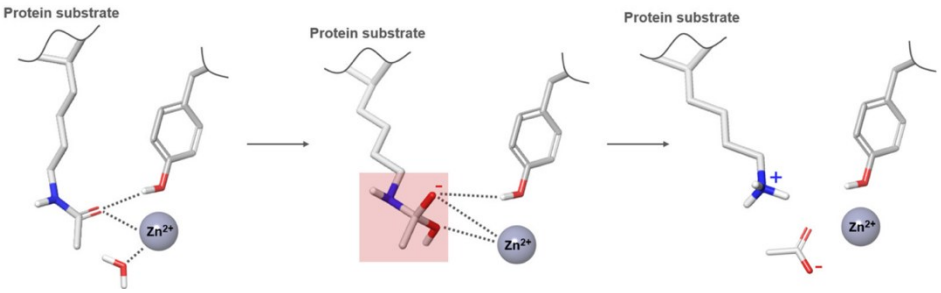

Figure 4: Dynamics and catalytic mechanisms of zinc ion-dependent HDACs during the deacylation process.

The hydrolyzing portion is highlighted in red (figure from [45]).

HDAC1 and HDAC2 are highly homologous Class I histone deacetylases, ubiquitously expressed, that are sharing approximately 82% to 86% amino acid identity and are localized to the cell nucleus, with HDAC1 having 482 aa in length and 55,103 kDa in mass, and HDAC2 having 488 aa in length and 55,364 kDa in mass [31,45,47]. Their structural organization consists of a conserved N-terminal and the central structural domains region that are conserved in all classical HDAC family as mentioned already and a more diverse and characteristic C-terminal domain [44,45]. The following domains are found in both HDAC1 and HDAC2: HDAC association domain, histone deacetylase domain and IAC(E/D)E motif [41,44]. HDAC association domain is located at the far N-terminus and is essential for the homo- and heterodimerization of the enzymes [44]. Histone deacetylase domain is composed of more than 300 amino acids, and it contains the active site where deacetylation occurs [41,44]. IAC(E/D)E motif is in the C-terminal region and is required for the interaction with "pocket proteins" like pRb, p107, and p130. While the motif is functionally the same, the specific sequence varies slightly between the two: IACEE in HDAC1 and IACDE in HDAC2 [41,44,45].

Beyond these shared features, the enzymes differ in other specialized regions: HDAC1 contains a unique nuclear localization signal (NLS) at its C-terminus and two amino-acid residues within the catalytic domain that are essential for the interaction with Chfr, an ubiquitin ligase regulating protein degradation; HDAC2 features a specific coiled-coil domain at its C-terminus as well [43–45]. The NLS is a specific sequence of amino acids that flags a protein for transport into the cell nucleus, and it is responsible for ensuring that HDAC1 is strictly confined to the nucleus [44,45]. A coiled-coil is a structural motif in which alpha-helices are twisted together, often serving as a platform for protein-protein interactions, and is believed to enable additional protein-protein associations, allowing HDAC2 to interact with a different or expanded set of partners compared to its paralog [44,45].

This region variability with the NLS and coiled-coil domains provide the structural basis for the non-redundant biological functions observed between HDAC1 and HDAC2.

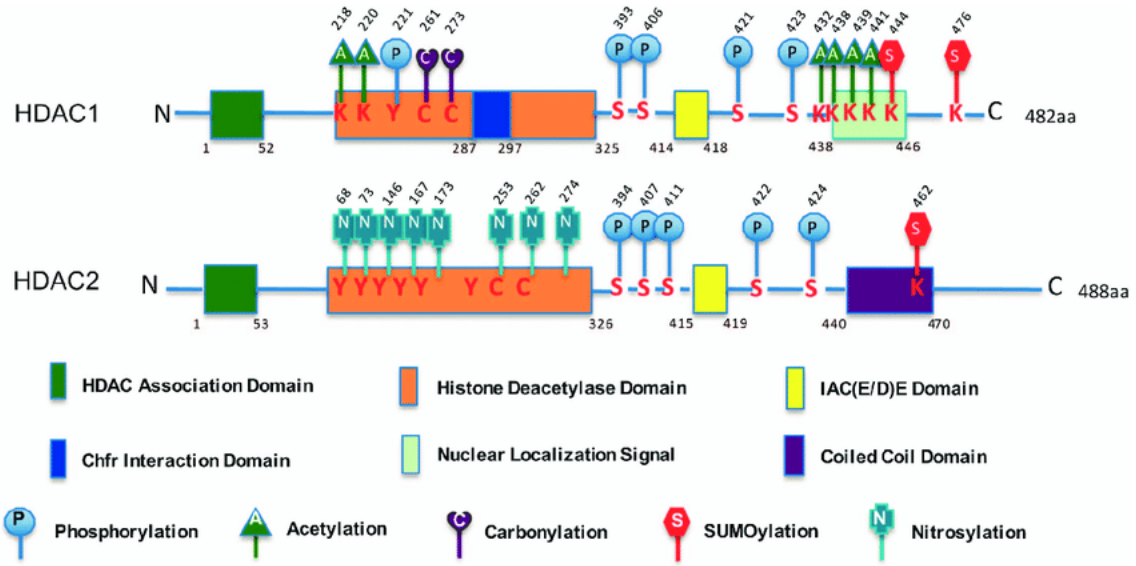

Figure 5: A schematic diagram of mammalian HDAC1 and HDAC2 structures with functional domains and post-translational modifications.

HDAC1 and HDAC2 share a highly conserved N-terminal HAD. The C-terminal part contains an IAC(E/D)E motif (IACEE in HDAC1 and IACDE in HDAC2). HDAC1 has a 2-residue Chfr interaction domain and a NLS at the C terminus. HDAC2 contains a coiled-coil domain at the C terminus. HDAC1 and HDAC2 are regulated by different post-translational modifications, such as phosphorylation, acetylation, nitrosylation, carbonylation, and sumoylation. K, lysine; C, cysteine; S, Serine; Y, tyrosine. Numbers indicate the corresponding amino-acidic (aa) position (figure from [43]).

Both enzymes are targets for various modifications that can be either chemical moieties (acetylation, phosphorylation, methylation, nitrosylation, ADP-ribosylation, glycosylation, and carbonylation) or proteins (ubiquitin, SUMO, NEDD8, FAT10, ISG15, and ATG8/ATG12), some of them being depicted in **Figure 5**, with many of the modified sites being conserved between both enzymes [43,44]. They are regulating the catalytic activity, protein stability, promote corepressor complex formation, and nuclear import of HDAC1 and HDAC2[43–45]. Phosphorylation is a well-characterized modification occurring on serine residues within the C-terminal portion of the proteins including sites on HDAC1: S393, S406, S421, and S423; and on HDAC2: S394, S407, S422, and S424 [43–45]. Phosphorylation enhances deacetylase activity, being essential for the formation of major corepressor complexes, and it also plays a role in regulating nuclear import [43–45]. Acetylation occurs on lysine residues within both the catalytic HDAC domain and the C-terminal tail on HDAC1: K218, K220, K432, K438, K439, and K441, typically resulting in reduced enzymatic activity [43–45]. Sumoylation occurs on specific lysine residues, such as K444 and K476 in HDAC1 and K462 in HDAC2, and is believed to modulate interactions with other proteins, thereby influencing which complexes the HDACs join [43–45]. Ubiquitination is noted as a modification that regulates the functions of most HDAC isoforms, primarily by influencing protein stability and targeting the enzymes for degradation [44,45]. S-Nitrosylation is specific to HDAC2, occurring at cysteine residues C262 and C274, and several tyrosine residues Y68, Y73, Y146, Y167, Y173, and Y253, acts as a regulatory switch that triggers the release of HDAC2 from chromatin, allowing for structural remodelling of the surrounding DNA [43–45].

HDAC1 and HDAC2 don't have a DNA-binding domains, that means that they cannot target specific genes on their own [41,44]. They function as the catalytic cores of several large, multi-subunit multi-protein corepressor complexes such as SIN3, NURD, and COREST that recruit them to specific genomic loci to regulate gene expression and chromatin structure [29,41,44].

The SIN3 complex typically consists of Sin3 (A or B), SDS3, the histone chaperones RbAp48 and RbAp46, and subunits like SAP18 and SAP30 [19,31,42,44]. It exists in a large form (Sin3L) that acts at promoters and a small form (Sin3S) that operates within gene bodies [19]. The structural integrity of the complex depends on the HDACs; losing HDAC1/2 results in the destabilization and degradation of the Sin3A subunit [41,48].

NuRD (Nucleosome Remodeling and Deacetylase) complex is unique for coupling deacetylation with ATP-dependent chromatin remodeling [19,44]. It contains HDAC1 and HDAC2, remodelling enzymes CHD3, CHD4, or CHD5 (Mi-2), and structural subunits MTA1/2/3, MBD2/3, p66, RbAp46, and RbAp48 [31,42,44]. The interaction between HDACs and MTA subunits is stabilized by inositol phosphates (InsP4 or InsP6), which act as "inter-molecular glue" to significantly activate the enzymes [19,45].

CoREST (corepressor for element-1-silencing transcription factor) complex is specifically targeted to neuronal genes and is comprises HDAC1/2, the scaffolding protein CoREST (RCOR1), the lysine demethylase LSD1, and MeCP2 [31,42,44]. The complex has bi-lobed or dumbbell shape that allows it to simultaneously remove acetyl groups (via HDAC) and methyl groups (via LSD1) from histone tails [19].

MiDAC (Mitotic Deacetylase) complex is essential for cell division and embryonic development. Its enzymatic activity is also potentiated by inositol phosphates [19,31].

NODE (Nanog and Oct4-associated) complex is specifically found in embryonic stem (ES) cells, this complex associates with Nanog and Oct4 to repress differentiation-related genes and maintain pluripotency [31,42,44].

SHIP1 complex is a specialized complex identified in spermatocytes that includes HDAC1, the heat shock protein HSPA2, and the testis-specific proteins SHIP1 and KCTD19 [42,44].

PRC2 (Polycomb Repressive Complex 2) is primarily a methyltransferase complex, but it recruits HDAC1/2 as well to facilitate gene silencing [43–45].

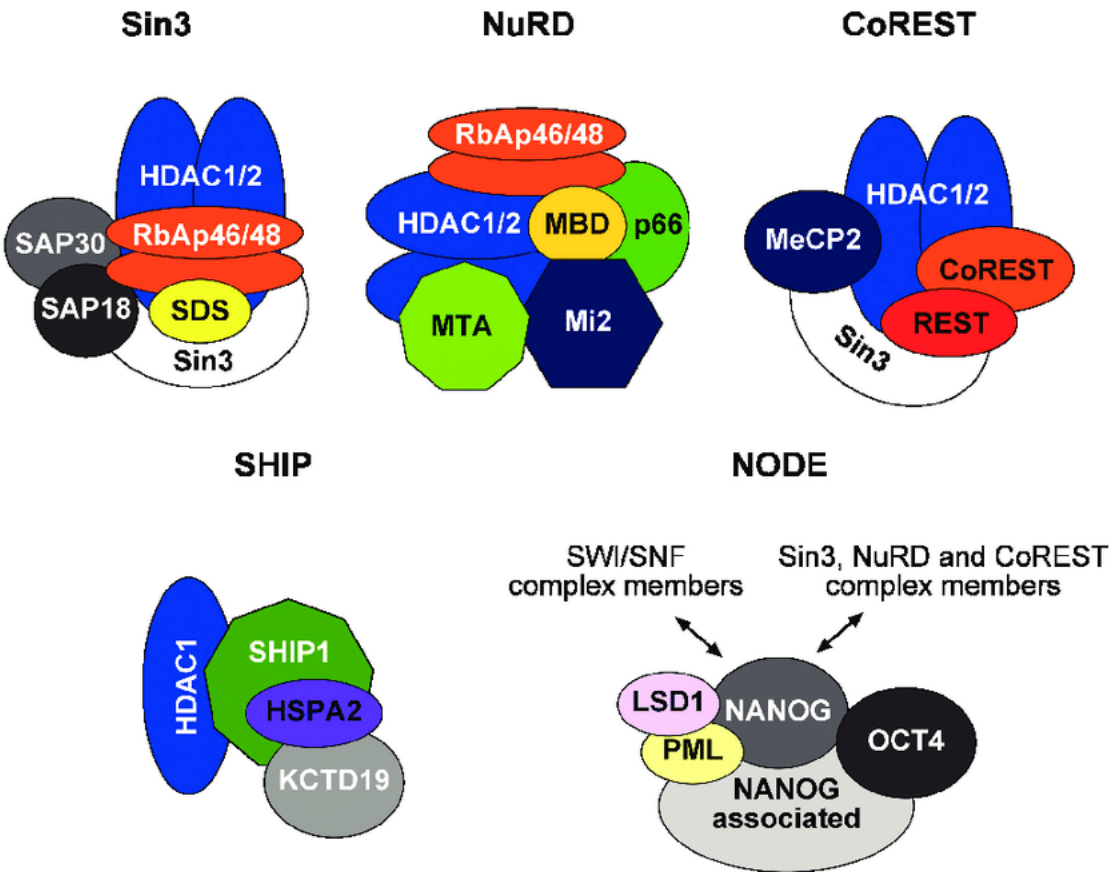

Figure 6:Composition of HDAC1/HDAC2 containing multiprotein complexes.

The SIN3 complex is comprised of HDAC1 and HDAC2 delivering enzymatic activity and the structural components SIN3, RbAp46, RbAp48, SAP18, SAP30 and SDS3. NuRD complex contains RbAp46, RbAp48, HDAC1, HDAC2, MTA, Mi-2, p66 and MBD. Both complexes are tethered to DNA via numerous transcription factors (not illustrated). The CoREST complex consists of CoREST, MeCP2, SIN3, HDAC1, HDAC2 and is targeted to DNA via the REST protein. Besides those three classical HDAC complexes, a testis specific complex has been identified, SHIP, containing SHIP1, HDAC1, HSPA2 and KCTD19. In ES cells the transcription factors Nanog and Oct4, together with associated proteins interact with HDAC1 and HDAC2 and several other members of the SIN3, NuRD, CoREST and SWI/ SNF complexes. Note that the schematic view does not mirror physical interaction of the subunits. (from [44])

1.6 The skin and its organization

The skin is the largest organ in the mammalian body covering the entire external surface and measuring up to $2m^2$, weighing about 12−15% of total adult body weight [49]. It is serving as a physical barrier and first line of defense against external environmental threats such as pathogens, ultraviolet (UV) light, chemicals, and mechanical injury, and on top, it regulates temperature, and maintain proper moisture within the body[41,49–51]. The skin consists of three principal layers: the outermost layer, the epidermis, the structure below it, the dermis and the structure below the dermis known as hypodermis or subcutaneous tissue, each having different anatomical structures and functions [49–51].

The epidermis has between 0.5−1.5mm thickness depending on the body part (0.5mm on the eyelids to 1.5mm on the palm of the hands and soles of the feet) and is avascular [49]. It is composed of several histologically distinct strata and various cell types crucial for its function [50]. Starting from the deepest to the most superficial, the five epidermal layers are: the stratum basale or stratum germinativum, stratum spinosum or prickle cell layer, stratum granulosum, stratum lucidum, and stratum corneum [49–51].

The stratum basale, also known as stratum germinativum, is the deepest layer of the epidermis consisting of a single layer of basal cells, cuboidal to columnar shaped, mitotically active stem cells that are constantly replenishing and producing new keratinocytes [49,50]. This layer also contains melanocytes which are responsible for skin colour and provide UV protection [49–51]. Another type of cell found in small numbers here are the Merkel cells that are specialized mechanoreceptor cells, found particularly in areas of high tactile sensitivity (such as fingertips) and in hair follicles [49,52].Stratum germinativum is separated from the dermis by a structure called the basement membrane (basal lamina) and attached to it by hemidesmosomes [49,50].

The stratum spinosum, also called prickle or spinous cell layer, is immediately above the basal layer, being composed of 8 to 10 cell layers that becomes thinner with age [49,50]. The cells in this layer are irregular, polyhedral-shaped keratinocytes with cytoplasmic processes, sometimes referred to as “spines”, which extend outwards and contact the neighbouring cells by desmosomes and further differentiate, making up the cells in the stratum corneum [49,50]. Langerhans dendritic cells can be found in this layer as well, acting as critical immune sentinels, recognizing, internalizing and processing antigens presented to the skin [49,50,53].

The stratum granulosum has 3 to 5 granular cell layers, either keratohyalin or lamellar granules which differentiate from the spinous layer, having flattened diamond-shaped cells and that continue to differentiate and express molecules which help them mature to epidermal cells at the stratum corneum layer. [49,50]. Keratohyalin granules contain keratin precursors that eventually aggregate, cross-link, and form bundles with the help of filaggrin [49,50,52]. The lamellar granules contain glycolipids that are secreted to the cell surfaces and act as glue to maintain cellular cohesion and create hydrophobic properties [49,50].

The stratum lucidum consists of 2−3 cell layers, only found in the thick and hairless skin of palms, soles and fingerprints [49,50,52]. Is the ‘clear’ layer of the skin, the transparent nature is due to the presence eleidin, a transformation product of keratohyalin [49,50].

The stratum corneum is the uppermost and thickest section of the epidermis consisting of 20−30 cell layers, having the most variable thickness, especially in callused skin [49,50]. The main cell type in this area is large and flat, dead, anucleate squamous keratinocytes, called corneocytes, which contain keratin and other structural proteins that are tightly crossed, forming a rigid and impermeable layer [49,50,52]. This layer is continuously renewing, and the entire layer is replaced by new keratinocytes during a period of four weeks, the turnover rate

getting reduced with age, the time taken to migrate from the basal layer to the epidermis increasing by up to 50%.
The epidermis functions as a first-line defense barrier that protects the body from the external environment with the help of its acidic pH (between 4 to 6.5) and to the antimicrobial activity through the release of anti-microbial peptides like defensins that are fighting bacteria like *S. aureus* [49,50,52].
The dermis is the middle "core" layer of the skin, the thicker structure containing vessels and nerves, nourishing, and supporting the epidermis [49]. It is divided into two distinct sub-layers that merge without a clear demarcation: the superficial papillary region and the deep reticular region [49,50]. The papillary layer is the thinner, uppermost dermal layer composed of loose connective tissue that contacts the basement membrane of the epidermis and contains blood vessels, lymphatics, epithelial cells, small muscles and neurons [49,50]. It consists of extracellular matrix and fibroblasts that are secreting the fibronectin and hyaluronic acid, two major components of the extracellular matrix which plays a role in wound healing [49,50]. The reticular layer is the deeper and much thicker layer, that is containing fibroblasts, consisting of a large network of blood vessels and collagen fibers, composing the fibro-elastic connective tissue [49,50]. The alignment of collagen and elastic fibers in the reticular dermis form the Langer lines, also known as cleavage lines, that are topological lines used to define skin tension [50]. The dermis houses many cells and cellular compartments, such as the sweat glands, sebaceous glands connected to hair follicles, muscles, sensory neurons, and blood vessels [50].
The Hypodermis, known as subcutaneous layer or fascia, is the deepest layer of the skin, consisting primarily of adipose cells but containing also sensory neurons, blood vessels, and scanty skin appendages, such as the deepest portions of hair follicles [49,50]. This layer anchors the dermis part of the skin to the underlying fascia surrounding the muscle or bone and acts as a fat storage and providing insulation and cushioning, protecting the underlying structures [49,50].
Together, the dermis and hypodermis provide the mechanical strength, nutritional support, and sensory capabilities required for the skin to function as a dynamic homeostatic organ.

1.6.1 Sebaceous glands and SZ95 cells

The sebaceous glands represent a skin appendage composed of epithelial cells (sebocytes), that originate from the same multipotent stem cell population that gives rise to the hair follicles and the epidermis. Sebaceous glands are holocrine glands that are typically located in the mid-dermis, and are usually associated with the hair follicle, forming the pilosebaceous unit. Similar than other skin-associated holocrine glands, such as Meibomian glands, they secrete an oily substance that is distributed over the hair and skin surface. This secretion provides lubrication and antimicrobial components that help to maintain the epidermal barrier. [41,54,55]. [52–54].
The distribution of sebaceous glands across the human body is very variate, from the highest density regions in seborrheic areas such as the face, scalp, chest, and upper back, with the scalp and forehead exhibit particularly high SG density, ranging from 400 to 900 glands per cm2; to areas that are completely lacking them like the palms, soles and dorsum of the feet [54–57].
Sebaceous glands are multi-acinar, multi-lobular holocrine glands giving them a "foamy" appearance under the microscope [56,57]. Each acinus secretes into a duct within its lobule, which further converges with the other lobules, forming a central duct that empties into the hair follicle, allowing secretions to reach the skin surface [55–57]. The sebaceous gland can be

divided histologically into three distinct zones: the peripheral zone, the maturation or middle zone, and the necrotic zone [55,57]. The peripheral zone is the outermost layer that consists of undifferentiated and proliferating basal cells that serve as the stem cell reservoir for the gland [55,57]. The maturation or middle zone is composed of sebocytes that are migrating inward from the peripheral zone and begin to differentiate and accumulate lipid droplets, dramatically increasing their cellular size [55,57]. The necrotic zone is the innermost zone, consisting of fully mature sebocytes that have completed their lipid synthesis and accumulation and are next disintegrating, resulting in the holocrine secretion of sebum through the ducts [55,57]. The whole process of differentiation of a human sebocyte takes about 7–14 days [55,57].

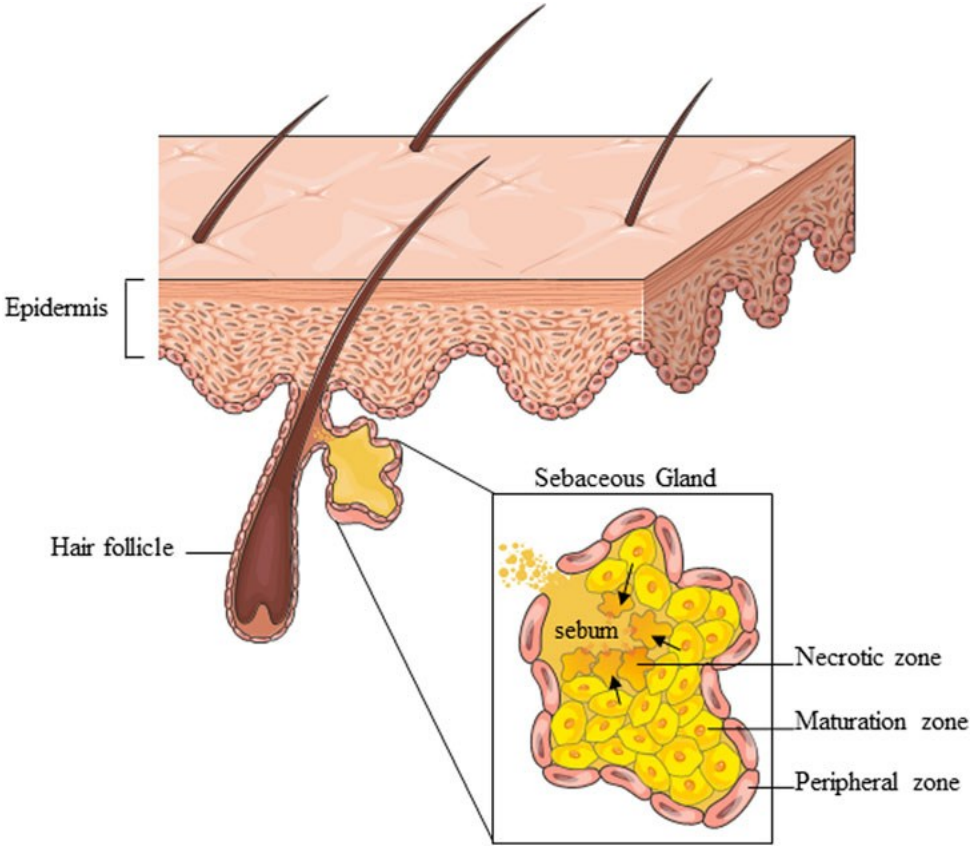

Figure 7: Schematic representation of the overall SG structure and partition into zones corresponding to various stages of sebocyte differentiation

(figure from [57])

The sebocyte secretion, sebum, is an oily, lipid-rich substance composed primarily of triglycerides and free fatty acids, that together constitute the majority of its composition (40%–60%), followed by wax esters (20%–30%), squalene (10%–20%), and cholesterol and its esters (2%–10%) [54,55,57,58]. The most characteristic products in the sebum are squalene, wax esters and sebum-specific fatty acids like branched chain fatty acids and lipids with particular pattern of unsaturation (monounsaturated sapienic acid) because they are not found in any other tissues or structures in the body [54,57,58].

Sebum is providing 90% of the skin's surface lipids, which are playing a crucial role in maintaining skin health, protection, and homeostasis [55,56]. These lipids serve multiple essential functions, including retaining moisture to prevent desiccation, lubricating the skin, providing a protective barrier, regulating pH, and acting as an antioxidant and antibacterial barrier [54–56,58].

The cellular crosstalk adjust the sebum synthesis because of the numerous regulatory receptors expressed by sebocytes that are consequently involved in the control of sebum secretion, including the corticotrophin–releasing hormone (CRH) receptor, melanocortin receptors (MC-R1–5), opiate receptors, the androgen receptor (AR), growth hormone receptor (GHR), IGF-1 receptor (IGF-1R), insulin receptor (IR), retinoid X receptor (RXR), retinoic acid receptor (RAR), peroxisome proliferator-activated receptors (PPAR), among others mentioned in **Table 2** [54,55,57]. As a result, disturbances in the hormonal, metabolic, neuroendocrine, or inflammatory signaling can translate into dysregulated sebocyte proliferation and lipid synthesis, promoting sebaceous gland dysfunction and contributing to skin disorders such as acne vulgaris, seborrhea, and seborrheic dermatitis [54,57].

Receptor Category	Specific Receptor	Primary Ligand(s)	Proliferation	Lipid Production	Native Human Sebocytes	SZ95 Immortalized Cells
Nuclear	AR	Androgens (DHT, Testosterone)	↑	↑	Expressed	Expressed
	PR	Progesterone	—	—	Expressed	Expressed
	ER-α / ER-β	Estrogens	—	↑	Expressed	Expressed
	RAR-α / RAR-γ	Tretinoin, atRA, 13-cis RA	↓	—	Expressed	Expressed
	RXR-α/β/γ	Rexinoids, Retinoids	↑	↑	Expressed	Expressed
	PPAR α	LTB4	—	↓	Expressed	Expressed
	PPAR γ	Linoleic acid, 15d-PGJ2	—	↑	Expressed	Expressed
	LXR-α / LXR-β	TO901317, 22(R)-OH-Cholesterol	↓	↑	Expressed	Expressed
	VDR	Vitamin D3	↑	↓	Expressed	Expressed
G-Protein Coupled	CRHR1/CRHR2	CRH, Urocortin	↓	↑	Expressed	Expressed
	MC1R	α-MSH	↓	—	Expressed	Expressed

Receptor (GPCR)	MC5R	α-MSH	↑	—	Expressed	Expressed
	OPR (μ-opioid receptor)	β-endorphin	↑	↑	Expressed	Expressed
	Histamine-1R	Histamine, antihistaminics	—	↓ (squalene)	Expressed	Expressed
	CBR1, CBR2	Endocannabinoids	—	—	Expressed	Expressed
	VPAC Receptors	VIP, NY, CGRP	—	—	Expressed	Expressed
Growth Factors	IGF-IR	IGF-I, Insulin	↑	↑	Expressed	Expressed
	GH-R	Growth Hormone (GH)	↑	↑	Expressed	Expressed
Ion Channels	VR (TRPV1)	Capsaicin	↓	—	Expressed	Expressed
Innate immune receptor	TLR2	LPS	—	—	Expressed	Expressed
	TLR4	LTA	—	—	Expressed	Expressed
	TLR6	Various	—	—	Expressed	Expressed
	CD14	LPS co-receptor	—	—	Expressed	Expressed
Receptor Tyrosine Kinase (RTK)	EGFR	EGF, HGF	—	—	Expressed	Expressed
	FGFR2b	FGF	—	—	Expressed	Expressed
	c-MET	HGF	—	—	Expressed	Expressed

Table 2: List of the native human sebocytes and SZ95 immortalized cells receptors and their functions *(informations from [54,59,60])*

Many studies on human sebocytes utilize SZ95 cells, an immortalized, stable, continuously renewable in vitro model of human sebaceous gland cell line derived from facial sebocytes of an 87-year-old woman transfected with the simian virus-40 large T antigen established by

Zouboulis et al. [54,61,62]. SZ95 sebocytes retain morphologic, phenotypic, and functional features of normal human sebocytes such as progressing differentiation with increasing cell volume and lipid synthesis, expression of specific protein markers of sebaceous lineage and terminal sebocyte differentiation, such as sebaceous gland antigen, keratins 7, 13, and 19, 5α-reductase type 1 enzyme and epithelial membrane antigen [54,61]. They can undergo apoptosis and also respond to hormones: 5α-dihydrotestosterone (androgen hormone) stimulate their proliferation and retinoids significantly inhibiting the proliferation [54,61]. On top, these cells synthesize sebum-specific lipids such as squalene and wax esters, as well as triglycerides and free fatty acids, even after 25±40 passages [61]. Although SZ95 cells were found to be aneuploid cells with chromosomal abnormalities like complex translocations between different chromosomes and the formation of dicentric, ring, and small marker chromosomes, the SZ95 line provides a consistent and long-term tool for studying sebaceous gland physiology and diseases [61].

1.7 Deregulations on the lipid production and lipid related genes

Sebaceous gland dysfunction can be grouped into two main outcomes: seborrhoea (quantitative sebum overproduction) and dysseborrhoea (qualitative shifts in sebum composition) [58,63]. These changes arise when disease-specific pathogenic cues reprogram lipid synthesis pathways and thereby alter expression of key metabolic genes and enzymes that control sebocyte proliferation, differentiation, and lipid output [58,63,64]. Acne is the most representative disorder of pilosebaceous deregulation, in which both sebum amount and composition are altered, characterized by comedones (blackheads/whiteheads) and inflammatory papules/pustules [63,64]. Seborrhoea and dysseborrhoea can together amplify the other acne driving processes, including colonization by Cutibacterium acnes, follicular hyperkeratinization, and local inflammation [55,64]. Sebaceous gland activity is strongly hormone-responsive: androgens (especially DHT) stimulate sebocyte proliferation and sebum production, while estrogens, glucocorticoids, growth hormone, and insulin/IGF-1 further modulate the sebaceous gland function [55,56,64]. Physiologically, sebum production is at its lowest in infancy, rises at puberty with androgens, and declines with age, and in women may increase during the luteal phase [55,56]. Acne is linked to Western high-glycemic diets because produces hyperinsulinaemia, lowering dietary glycemic load associated with improved insulin sensitivity, and reducing the levels of sapienic acid which are correlated with reduced acne severity [55,58].

In contrast to acne, other sebaceous gland-associated dermatoses display distinct phenotypic profiles [55]. Atopic dermatitis is associated with reduced gland number and volume, accompanied by depletion of triglycerides, squalene, and wax esters, contributing to barrier impairment and cutaneous dryness, with IL-4 and IL-13 altering sebocyte steroid metabolism via 3β-HSD1 and reducing total triglyceride output [55]. Seborrhoeic dermatitis involves microbial reshaping of sebum composition, in which Malassezia species preferentially metabolise saturated fatty acids through lipase activity, leaving behind irritant unsaturated fatty acids such as oleic and arachidonic acid and producing compositional shifts characterised by elevated free fatty acids and cholesterol alongside reduced triglycerides and squalene [55].

At the molecular level, sebum production is driven predominantly by de novo lipogenesis, a pathway converting glucose-derived acetyl-CoA into fatty acids [55,65,66]. The sterol regulatory element-binding protein 1 (SREBP-1) family functions as the master transcriptional regulator of this process, directly activating over thirty genes dedicated to lipid synthesis and uptake [34,65–67]. SREBP-1a and SREBP-1c are the two primary isoforms encoded by a single

gene, SREBF1, located on chromosome 17p11.2, and are generated using alternative promoters and transcription start sites that produce distinct forms of exon 1, spliced to a common set of downstream exons [65–67]. The resulting proteins are nearly identical except for their N-terminal transactivation domains [65]. SREBP-1a contains a longer acidic transactivation segment that confers greater potency as a transcriptional activator and drives a broader lipogenic and cholesterogenic program, while SREBP-1c is more restricted in its activity, preferentially inducing genes required for fatty acid and triglyceride synthesis, including FASN and ACACA, without significantly affecting cholesterol synthesis [34,65–68]. SREBP-1c is the predominant isoform in the liver and most adult tissues including sebocytes and is the primary driver of pathological lipogenesis in conditions of insulin resistance and obesity, whereas SREBP-1a predominates in cultured cell lines and selected tissues of the immune system and is essential for normal embryonic development [34,55,65,67,68].

Both isoforms are synthesized as inactive precursors anchored to the endoplasmic reticulum membrane through association with the escort protein SREBP cleavage-activating protein (SCAP) and ER retention protein called Insig [65,67]. Upon receipt of lipogenic signals, the SREBP-SCAP complex dissociates from Insig and is transported in COPII-coated vesicles to the Golgi apparatus, where sequential proteolytic cleavage by Site-1 protease and Site-2 protease releases the active N-terminal transcription factor domain [65–67]. This fragment translocates to the nucleus, where it binds sterol response elements (SREs) in the promoters of lipogenic target genes including FASN and ACACA, driving their transcription [34,65,66,68]. SREBP-1c expression and proteolytic processing are dynamically regulated by nutritional and hormonal status: insulin and LXR agonists strongly induce SREBP-1c transcription, while glucagon and polyunsaturated fatty acids suppress it, in contrast to SREBP-1a, which is constitutively expressed at low levels and is not subject to the same nutritional regulation [65,66].

The primary transducer of insulin and IGF-1 signals into the lipogenic program in sebocytes is the PI3K/Akt/mTORC1 signalling axis [55]. Binding of insulin or IGF-1 to their respective receptors recruits PI3K to the plasma membrane, where it converts phosphatidylinositol 4,5-bisphosphate (PIP2) to phosphatidylinositol 3,4,5-trisphosphate (PIP3), providing a docking platform for Akt [69,70]. Full Akt activation requires phosphorylation at two distinct sites by PDK1 and mTORC2 [69,70]. Activated Akt inhibits the TSC1/2 complex, relieving suppression of mTORC1, which subsequently drives upregulation and proteolytic processing of SREBP-1 and promotes the broader lipogenic transcriptional program [55,69,70]. A critical secondary consequence of Akt activation is the phosphorylation and nuclear export of FoxO1, a transcription factor that under basal conditions acts as a corepressor of the androgen receptor [55,69,70]. Removal of nuclear FoxO1 by Akt signalling releases this restraint on androgen receptor activity, amplifying androgen-driven sebocyte proliferation and sebum production and creating a convergent hormonal and metabolic stimulus for lipogenesis [55,70]. Androgens and insulin/IGF-1 act on partially overlapping downstream targets, androgens via mTORC2 and insulin/IGF-1 via PI3K, both ultimately converging on mTORC1-mediated SREBP-1 upregulation and inflammatory mediator production, including elevated perilipin 2 (PLIN2/ADRP), which has been linked to the coupling of seborrhoea and inflammation [55].

PPARγ, a member of the nuclear receptor superfamily, functions as the master regulator of sebocyte maturation and acts as a physiological counter-regulator of the insulin/IGF-1-driven lipogenic axis [55,71,72]. In the sebaceous gland, PPARγ expression correlates directly with differentiation status: mature, lipid-laden sebocytes in the central necrotic zone exhibit high PPARγ levels, whereas poorly differentiated proliferative cells at the gland periphery express low levels [55]. By promoting cellular maturation, PPARγ reduces sebocyte sensitivity to hormonal lipogenic stimuli, and selective PPARγ modulation has been shown experimentally

to normalise the insulin/IGF-1 response and counteract acne-like lipid dysregulation [55]. Under pathological conditions, however, hyperactivation of the PI3K/Akt/mTORC1 axis is accompanied by concomitant suppression of both PPARγ and nuclear FoxO1, producing a low-differentiation, high-metabolic state that display key features of the acne-like sebocyte phenotype [55]. Poorly differentiated SZ95 sebocytes express elevated levels of insulin and IGF-1 receptors relative to mature cells, making them hypersensitive to hormonal and dietary lipogenic stimuli, and reproduce acne-like lipid composition and inflammatory mediator profiles upon insulin stimulation in vitro [55].

Beyond transcriptional and signaling regulation, sebaceous lipogenesis is subject to epigenetic control through modulation of histone acetylation at lipogenic gene promoters [34,68]. The histone acetyltransferase p300 functions as a central coactivator of the SREBP-1 lipogenic program, with its activity and expression elevated in response to both insulin and LXR agonist stimulation, leading to enhanced histone H3 and H4 acetylation and transcriptional activation at lipogenic gene loci including SREBF1 and FASN [34,68]. In the acne-like state, p300 is upregulated and contributes to sustained transcriptional permissiveness at these loci, while class I HDACs, particularly HDAC1, which normally provide opposing deacetylase activity to restrain the lipogenic program, are functionally compromised [34,68]. Consistent with a causal role for p300 in acne-like lipid deregulation, minocycline has been reported to attenuate excessive lipid accumulation in sebocytes through inhibition of p300 HAT activity, resulting in reduced expression of SREBP-1, FASN, and ACCA34. These observations establish the balance between p300-mediated histone acetylation and HDAC1-mediated deacetylation as a critical epigenetic regulatory axis governing sebaceous lipid secretion, and position both enzymes as candidate targets for therapeutic intervention in conditions characterised by sebaceous gland hyperactivity [34,68].

1.8 Aim of the project

Our laboratory is interested in elucidating the role of HDAC1 and its catalytic activity in the epigenetic regulation of gene expression, with the long-term goal of improving knowledge about isoform-specific HDAC functions that may ultimately contribute to the development of more targeted therapeutic strategies. In this context, models of catalytic inactivation are of particular interest, as they allow the enzymatic function of an HDAC to be selectively disrupted while preserving its structural and scaffolding roles within co-repressor complexes, thereby mimicking the effect of isoform-specific HDAC inhibition more closely than complete protein deletion.

Previous work in our laboratory demonstrated that treatment of SZ95 sebocytes with class I HDAC inhibitors such as MS-275, induces lipid droplet formation and upregulates lipid-associated transcription factors and lipogenic enzymes at both the transcriptional and protein level. Complementary evidence was obtained from a mouse model in which the catalytically inactive HDAC1 H141A variant was introduced specifically in keratinocytes and sebocytes, revealing a skin phenotype characterized by enhanced sebaceous gland size, local inflammation, and dysregulation of lipid-associated genes. These observations collectively suggested that HDAC1 catalytic activity plays a direct role in controlling sebaceous lipogenesis through chromatin-based mechanisms and raised the question of whether this regulation operates through changes in histone acetylation at the promoters of lipogenic target genes.

The central hypothesis of this project was therefore that HDAC1 regulates the expression of critical lipid-associated transcription factors and lipogenic enzymes in human SZ95 sebocytes

via its catalytic deacetylase activity. To address this hypothesis, three specific aims were pursued.

The first aim was to further characterize the process of lipid generation in response to altered histone acetylation states in SZ95 sebocytes. Chemical perturbation was produced using class I HDAC inhibitors to induce lipid accumulation, and the p300 HAT inhibitor A-485 to determine the contribution of p300-dependent histone acetylation to the lipogenic phenotype, thereby determining the functional balance between acetylation and deacetylation at lipogenic gene loci.

The second aim was to establish more isoform-specific approaches to dissect the contribution of individual class I HDACs to sebaceous lipogenesis. Since chemical HDAC inhibitors target multiple isoforms simultaneously and may exert off-target effects, siRNA-mediated knockdown of HDAC1, HDAC2, and HDAC3 was established and validated in SZ95 sebocytes. In parallel, a genetic system was developed to inactivate HDAC1 specifically by generating transgenic SZ95 cell lines expressing the catalytically inactive HDAC1 H141A variant via CRISPR/Cas9-mediated knock-in. This approach was designed to separate the enzymatic function of HDAC1 from its structural role within co-repressor complexes, avoiding the confounding compensatory upregulation of HDAC2 that is associated with knockdown-based strategies, and thereby enabling a more precise determination of HDAC1 catalytic function in the regulation of lipid metabolism.

The third aim was to investigate chromatin-level changes accompanying lipid-associated gene activation in SZ95 sebocytes. CUT&RUN chromatin profiling using an antibody against H3K4me3, a histone mark associated with transcriptionally active promoters, was performed in sebocytes under lipogenic stimulation. This aimed to determine whether the pharmacological perturbation employed in this study produce detectable and locus-specific changes in promoter-associated chromatin states at key lipogenic gene loci, providing a mechanistic link catalytic activity of class I HDACs, histone acetylation dynamics, and transcriptional regulation of the sebaceous lipogenic program.

2 MATERIALS AND METHODS

2.1 Human sebocytes SZ95 cell culture

The immortalized human SZ95 sebaceous gland cell line was cultured in DMEM/F-12 medium or Sebomed basal medium supplemented with 1mM CaCl2, 10% FBS, 1% penicillin-streptomycin, 2,5mM Ala-Gln (200mM solution) and 5 ng/mL human epidermal growth factor. All reagents were sterile filtered by us or by the manufacturer and were preheated to 37°C before use. The sebocytes were incubated in an incubator at 37°C with 5% CO_2. The medium was replaced every 2 days. All working steps with cells were conducted under sterile conditions in a Laminar Flow Hood, with 70% ethanol used for disinfection of surfaces and materials.

Reagents used	Quantity	Source	Product number
Sebomed basal medium	500 ml	MERCK	F8205
DMEM/F-12 medium	500ml	MERCK	D6434
1M CaCl2	500µl	MERCK	C5670
Ala-Gln	6,25ml	MERCK	G8541
Penicillin – Streptomycin	5ml	MERCK	P4333
FBS	50ml	MERCK	F7524
hEGF	2,5 µl	MERCK	E9644

Table 3: Reagents used for the medium preparation

Cell line	Flag % positive	Notes	Source
SZ95 Sebocytes	-	-	Gruber Lab
SZ95 Sebocytes (early passage)	-	-	Toroscik Lab
HDAC1 H141A Clone 1G3G9	Flag-negative	Subclones	Fischer Lab Izabela Pasca
HDAC1 H141A Clone 2E3C4	Flag-negative	Subclones	Fischer Lab Izabela Pasca
HDAC1 H141A Clone 1G3C8	Flag-negative	Subclones	Fischer Lab Izabela Pasca
HDAC1 H141A Clone 2E3B4	Flag-negative	Subclones	Fischer Lab Izabela Pasca
HDAC1 H141A Clone 1G3E11	100 % Flag-positive	Subclones	Fischer Lab Izabela Pasca
HDAC1 H141A Clone 1G3C5	100 % Flag-positive	Subclones	Fischer Lab Izabela Pasca
HDAC1 H141A Clone 1G3C6	75% Flag-positive	Subclones	Fischer Lab Izabela Pasca

HDAC1 H141A Clone 2E3A6	75% Flag-positive	Subclones	Fischer Lab Izabela Pasca
HDAC1 H141A Clone 2E3B9	75% Flag-positive	Subclones	Fischer Lab Izabela Pasca
HDAC1 H141A Clone C3	100 % Flag-positive	Clones	Fischer Lab Lukas Baumgartner
HDAC1 H141A Clone C7	Flag-negative	Clones	Fischer Lab Lukas Baumgartner
HDAC1 H141A Clone C5	Flag-negative	Clones	Fischer Lab Lukas Baumgartner
HDAC1 WT Clone 5H5	Flag-negative	Subclones	Fischer Lab Lukas Baumgartner
HDAC1 WT Clone 3D9-1	Flag-positive	Subclones	Fischer Lab Lukas Baumgartner
HDAC1 WT Clone 3D9-2	Flag-positive	Subclones	Fischer Lab Lukas Baumgartner
HDAC1 WT Clone 3F8	97% Flag-positive	Subclones	Fischer Lab Izabela Pasca
HDAC1 WT Clone 4G7	99% Flag-positive	Subclones	Fischer Lab Izabela Pasca
HDAC1 WT Clone 3D7	25% Flag-positive	Subclones	Fischer Lab Izabela Pasca
HDAC1 WT Clone 4G6	Flag-negative	Subclones	Fischer Lab Izabela Pasca
HDAC1 WT Clone 5H6	Flag-negative	Subclones	Fischer Lab Izabela Pasca

Table 4: Cell lines used in this project

2.1.1 Cultivation and propagation of SZ95 sebocytes

2.1.1.1 Thawing cells

Vials (containing 10^6 cells each) were quickly thawed by hand and added to a 15ml falcon containing 8 ml of SZ95 medium. Afterwards, the suspension was centrifuged for 3 minutes at 1500 rpm (300 rcf), and the supernatant (SN) was discarded. The pellet was resuspended in 8 ml of fresh SZ95 medium and seeded into 6 or 10cm plates. The next day, the medium was renewed.

2.1.1.2 Splitting cells

Cells were split at 60-80% confluency. Medium and Trypsin-EDTA (Thermo Fisher #25200056) were warmed up at 37°C in a water bath before usage. The medium was removed from the dish, and the cells were washed once with 1x PBS (Phosphate Buffered Saline). After removing the 1xPBS, Trypsin-EDTA was added to the dish to detach the cells (e.g. 3ml for 10cm dish), and incubated between 3 and 8 minutes (depending on the cell line) at 37°C. Afterwards, the cells were removed mechanically by hitting the plate against the table and checking at the

microscope to see if the majority of cells had detached. Then, the triple amount of medium as the amount of trypsin was added to the dish to inactivate the Trypsin-EDTA and the cells were transferred into a 15ml falcon tube. Next, the suspension was centrifuged for 3 minutes at 1500 rpm (300 rcf), and the SN was discarded. The cells were resuspended in 2 ml medium by pipetting up and down at least 15 times, and they were counted using the Countness 2 Cell counter (Thermo Fisher Scientific) and diluted in the desired concentrations (or just splitted in 1:3 to 1:5 ratio).

10x PBS	8% sodium chloride
	0.2% potassium chloride
	0.2% monopotassium phosphate
	1.11% disodium hydrogen phosphate
	Diluted in dH2O and pH adjusted to 7.4 with NaOH

Table 5: 10xPBS

2.1.1.3 Seeding cells

The needed number of cells (e.g. $0{,}2x10^6$ cells into 6 cm plate) was resuspended in the total medium (e.g. 5ml for 6cm plate). This solution was then pipetted up and down at least 10 times, and the medium containing the cells was added to the well plates as required.

2.1.1.4 Freezing cells

Cells were detached from the culture plate using Trypsin-EDTA as described in **2.1.1.2**. After the centrifugation, the pellet was resuspended in 1 ml of medium, then the cells were counted and diluted to $2x10^6$ cell/ml. Next, 0.5 ml of cells were added to 0.5 ml of 2x Freezing medium (**Table 6**) per vial to achieve a final concentration of $1*10^6$ cell/ml, then the vial was placed on ice until the remaining vials were prepared. Then, vials were transferred at -80°C using Mr. Frosty freezing container (Nalgene, Sigma Aldrich) and after 24 hours moved into the -150°C liquid nitrogen tank for long term storage.

Freezing medium	80% DMEM medium
	20% DMSO

Table 6: Freezing medium

2.1.1.5 Harvesting cells for protein analysis

The cells were washed once with 1x PBS, and then 4 ml of 1x PBS was added to scrape them off the plates using a cell scraper. The suspension was transferred into a 15 ml Falcon tube and centrifuged for 5 minutes at 560 rcf. The supernatant was discarded and the pellet was resuspended in 1 ml 1x PBS. The suspension was transferred into 1.5 ml microcentrifuge tubes, spin again for 5 minutes at 560 rcf, and the supernatant was removed. Samples were flash frozen in liquid nitrogen and stored at -80°C or immediately used for further experiments.

2.2 Generation of transgenic human sebocyte cell lines expressing wildtype HDAC1 and catalytic inactive HDAC1 (HDAC1 H141A) using CRISPR/Cas9 technology

2.2.1 Cell transfection overview and reagents

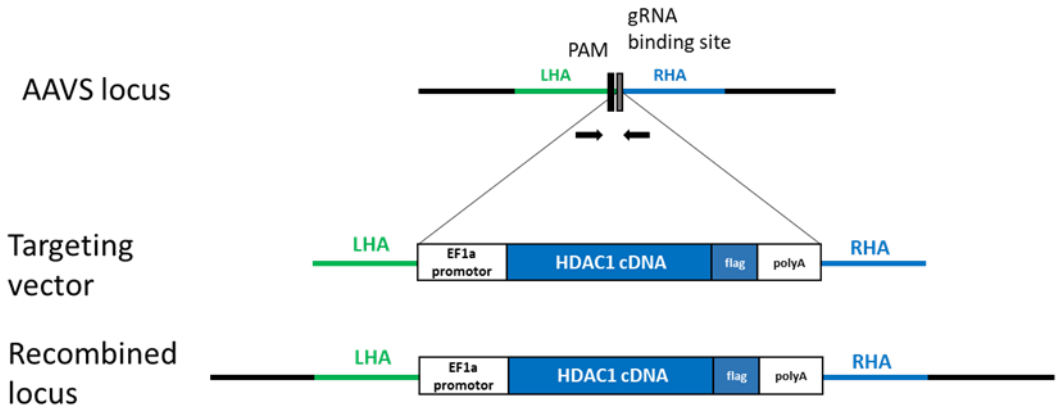

Figure 8: *Schematic overview of CRISPR-Cas9 mediated knock-in of HDAC1 constructs into the AAVS safe harbor locus. Homology arms (LHA, RHA) guide targeted integration of the donor vector. The two constructs HDAC1 WT and H141A, were designed with a EF1α promoter, a FLAG-tag and polyA signal, enabling stable expression of WT or H141A HDAC1 in SZ95 cells. Adapted from Master thesis Eva Zorec, 2018*

The pCAS9 plasmid was created using ZymoPURE™ II Plasmid Maxiprep Kit and encodes the Cas9 endonuclease, which introduces site-specific double-strand breaks at the AAVS1 safe harbor locus. The pGuide RNA plasmid provides the guide RNA that directs Cas9 to the target site. pVJV_HDAC1_wt and pVJV_HDAC1_H141A plasmids carry wild-type (WT) or H141A (catalytically inactive) HDAC1 genes for integration into the AAVS1 locus via homology repair. pcDNAc Blasto GFP includes a blasticidin resistance gene for selection and a GFP reporter for efficiency tracking of transfection. FuGENE reagent was used to form DNA-cell membrane complexes, facilitating efficient plasmid uptake with minimal toxicity.

Reagents used	Source
Opti-MEM™	Thermo Fisher Scientific (#31985062)
pCAS9 (#771)	Hess et al, 2022
pGuide RNA (#596)	Hess et al, 2022
pVJV_HDAC1_WT (1:2)	Hess et al, 2022
pVJV_HDAC1_H141A (1:2)	Hess et al, 2022

pcDNAc Blasto GFP (1:5)	Hess et al, 2022
FuGENE HD transfection reagent	Promega (#E2311)

Table 7: Reagents used for the transfection

2.2.2 Transfection protocol

On day 1, SZ95 cells were seeded a density of 0.08 × 10^6 cells in a six-well plate. On day 2, the medium was replaced, and all the reagents for the transfection mix were put together in an Eppendorf tube for each well as indicated in **Table 8** and were incubated 15 min at room temperature (RT). After that the 100µl were added dropwise to the cells according to the specific well. On day 3, the medium was replaced again, and blasticidin (5µg/ml final concentration) was applied to the designated wells as indicated in the **Table 8**, to eliminate the non-transfected cells because the successfully transfected cells have the blasticidin resistance gene. On day 4, the medium was exchanged once more. On day 5, transfected cells were identified under a fluorescent microscope, as successful transfection resulted in fluorescence expression.

	Well 1	**Well 2**	**Well 3**	**Well 4**	**Well 5**	**Well 6**
Reagents and vectors	**Volumes in µl**	**Volumes in µl**	**Volumes in µl**	**Volumes in µl**	**Volumes in µl**	**Volumes in µl**
Opti-MEM	87,21	86,93	92,55	94,00	94,00	-
pCAS9	2,54	2,54	-	-	-	-
pGuide RNA	1,5	1,5	-	-	-	-
pVJV_HDAC1_WT (1:2)	1,3	-	-	-	-	-
pVJV_HDAC1_H141A (1:2)	-	1,5	-	-	-	-
pcDNAc Blasto GFP (1:5)	1,45	1,45	1,45	-	-	-
FuGENE reagent	6.00	6,00	6,00	6,00	6,00	-
Total	100.0	100.0	100.0	100.0	100.0	-
Blasticidine 24h later	+	+	+	+	-	-

Table 8: The transfection mixes reagents and how they are distributed

2.2.3 Clonal Dilution and Culture

Clonal dilution was performed by plating approximately 5 cells per well into five 96-well plates for the WT and H141A positive transfected wells. Cells were maintained in a specialized growth medium described in **Table 9**. Cells were cultured in 96-well plates for approximately 2–3 weeks. Following this period, each plate was split into two new 96-well plates: one plate designated for immunofluorescent staining, to identify the positive clones, and the other plate designated for further propagation.

Specialized growth medium	20% fetal bovine serum (FBS)
	40% standard culture medium
	40% enriched medium (medium derived from growing SZ95 cells, filtered prior to use)

Table 9: Specialized growth medium

2.3 Treatments applied to the SZ95 cells

All treatments were designed to target HDAC activity, one way or another, helping to evaluate their impact on lipid metabolism. To assess lipid formation under varying conditions, treatments were applied either individually or in combination. All procedures were conducted under a sterile laminar flow hood, with 70% ethanol used for disinfection of surfaces and materials.

2.3.1 Treatment with siRNA

The siRNA treatment is used for the knock down (KD) of HDAC1, HDAC2 andHDAC3, as a control we used Silence Select Negative Control siRNA. First, the siRNA tube was quickly spined to ensure that the dried siRNA is at the bottom of the tube, and resuspended it in nuclease-free water provided for a final working concentration of 20 µM.

On day 1, SZ95 sebocytes were seeded at a density of 0.2 × 10^6 cells per 6 cm plate or 0,03 × 10^6 cells per well in a 12-well plate. On Day 2, at approximately 40% confluency, the medium was replaced from each plate and the cells were transfected with siRNA. Two 1.5 ml Eppendorf tubes (A and B) were used, tube A contained Opti-MEM™ (half of the amount mention in **Table 10**) and Lipofectamine™ 2000, while tube B contained Opti-MEM™ (the other half of the amount mention in **Table 10**) and the respective siRNA. Tubes A and B were incubated separately for 15 minutes at RT, then combined and incubated for another 20 minutes, in the end the A+B mix was added dropwise to the cell plates. On day 3, the medium was refreshed to remove residual transfection reagents and depending on how long the treatment needs to stay (48 or 72 hours) cells were used for further experiments on day 4 or day 5.

Reagents used	Volume for a 6cm plate (µl)	Volume for a 1 well of a 12-well plate (µl)	Final concentration	Source	Product number
siRNA HDAC1 s73	17,5	3,5	0.07 µM	Thermo Fisher Scientific	4390824
siRNA HDAC2 s6493	17,5	3,5	0.07 µM	Thermo Fisher Scientific	4390824

siRNA HDAC3 s16878	17,5	3,5	0.07 µM	Thermo Fisher Scientific	4390824
Silencer™ Select Negative Control siRNA	17,5	3,5	0.07 µM	Thermo Fisher Scientific	4390843
Opti-MEM™	500+500	100+100	10%+10%	Thermo Fisher Scientific	31985062
Lipofectamine™ 2000	10	2	0.2%	Thermo Fisher Scientific	11668027

Table 10: reagents used for the siRNA KD and their final concentration that were applied on the cells

2.3.2 Treatment with insulin and LXR agonist

SZ95 cells produce lipids in response to Insulin and stimulation of Liver X receptor (LXR), so insulin and LXR agonist (TO901317) treatments were used as a positive control. Insulin powder was solubilized in 0.01 M HCL to get a working concentration of 10 mg/mL, and TO901317 was dissolved in DMSO to a working concentration of 1mM. To avoid freeze-thaw cycles, after solubilization, both substances were divided into aliquots and stored at -20°C for long term storage.

On day 1, SZ95 sebocytes were seeded at a density of 0.2 × 10^6 cells per 6 cm plate or 0,03 × 10^6 cells per well in a 12-well plate. On day 2, at approximately 40% confluency cells were treated with insulin and TO901317 at the concentration specified in **Table 11**, and DMSO was used as a control (1:1000). On day 3, cells were observed and notes were taken, if something was found to be unusual. On day 4 (48h), insulin and TO901317 treatment was repeated. On day 5, after 72h treatment, cells were used for further experiments.

Reagents used	Final concentration	Source	Product number
Insulin	10µg/ml	Merck	I2643
TO901317 (LXR-Agonist)	1µM TO901317	Merck	T2320
Dimethyl sulfoxide (DMSO)	1:1000	Merck	D2650

Table 11: reagents used for insulin+TO901317 treatment and their final concentration that were applied on the cells

2.3.3 Treatment with MS-275

Cell lines were treated with the class I HDAC inhibitor MS-275, having high affinity for HDAC1. This compound was diluted to a working concentration of 1mM taken in DMSO, and to avoid freeze-thaw cycles, after solubilization, the substance was divided in aliquots and stored at -20°C for long term storage.
On Day 1, SZ95 sebocytes were seeded at a density of 0.2 × 10^6 cells per 6 cm plate or 0,03 × 10^6 cells per well in a 12-well plate. On Day 2, the medium was aspirated from each well and replaced with fresh medium containing the final concentration of 0.5µM MS-275, and as a control use DMSO diluted 1:1000. On Day 3 (24h with the treatment) the cells were observed and notes were taken. On Day 4 (48h) cells were treated the same as on Day 2. On Day 5 (72 h), cells were used for further experiments.

Reagents used	Final concentration	Source	Product number
MS-275	0.5µM	Selleck Chemicals	S1053
Dimethyl sulfoxide (DMSO)	1:1000	Merck	D2650

Table 12: reagents used for MS-275 treatment and their final concentration that were applied on the cells

2.3.4 Treatment with A-485

Cell lines were treated with the p300 acetyltransferase inhibitor A-485. This compound was diluted to a working concentration of 1 mM in DMSO. To avoid freeze-thaw cycles, after solubilization, the substance was divided into aliquots and stored at -20°C for long-term storage.
On Day 1, SZ95 sebocytes were seeded at a density of 0.2 × 10^6 cells per 6 cm plate or 0.03 × 10^6 cells per well in a 12-well plate. On Day 2, the medium was aspirated from each well and replaced with fresh medium containing a final concentration of 1 µM A-485, and as a control, DMSO was diluted 1:1000. On Day 3 (24h with the treatment), the cells were observed, and notes were taken. On Day 4 (48h), cells were treated similarly to Day 2. On Day 5 (72h), cells were used for further experiments.

Reagents used	Final concentration	Source	Product number
A-485	1µM	MedChemExpress	HY-107455
Dimethyl sulfoxide (DMSO)	1:1000	Merck	D2650

Table 13: reagents used on the A-485 treatment and their final concentration that were applied on the cells

2.3.5 Treatment with PPARγ inhibitor

Cell lines were treated with the PPARγ inhibitor T0070907, targeting the key regulator of sebocyte lipogenesis. This compound was diluted to a working concentration of 1 mM in DMSO, and to avoid freeze-thaw cycles, after solubilization, the substance was divided into aliquots and stored at -20°C for long-term storage. On Day 1, SZ95 sebocytes were seeded at a density of 0.2 × 10^6 cells per 6 cm plate or 0.03 × 10^6 cells per well in a 12-well plate. On Day 2, the medium was aspirated from each well and replaced with fresh medium containing a final concentration of 2 µM T0070907, and as a control, DMSO was diluted 1:1000. On Day

3 (24h with the treatment), the cells were observed and notes were taken. On Day 4 (48h), cells were treated similarly to Day 2. On Day 5 (72h), cells were used for further experiments.

Reagents used	Final concentration	Source	Product number
T0070907 (PPARγ - inhibitor)	2µM	Merck	T8703
Dimethyl sulfoxide (DMSO)	1:1000	Merck	D2650

Table 14: reagents used on the T0070907 treatment and their final concentration that were applied on the cells

2.4 Staining for neutral lipids using Oil red O solution (ORO)

The cells were cultivated in 12 well plates for 3 to 4 days depending on the treatment. After the specific treatment time the cells were first fixed. The procedure began by removing the medium from each well and rinsing the cells with 1xPBS. Under the chemical hood, 500 µL of 10% formalin to each well was added and incubated at 4 °C for 10 minutes to fix the cells. After fixation, formalin was carefully removed and disposed in designated chemical waste container. The wells were then rinsed three times with 1xPBS for 30 seconds each, thereby discarding the first PBS wash in special waste container as well. Following this step, the procedure was then continued at the bench. Next, the ORO working solution was filtered, and applied to the cells that were incubated at room temperature for 26 minutes. After removing the ORO solution, wash the wells three times with distilled water to remove any residual stain. Hematoxylin was added and incubated for 6 minutes to counterstain the nuclei. Then everything was rinsed with tap water one last time and after ensuring complete removal of residual liquid. Finally, one drop of mounting medium (Histoline, PMT030) was added per well, the coverslips was placed carefully to avoid air bubbles, and the plates were allowed to dry overnight before imaging on the following days.

Reagents used	Indications
ORO stock solution	500mg ORO+ 60ml Triethyl Phosphate+40ml ddH2O
ORO working solution (made just prior to use)	10ml stock solution+8ml ddH2O (filtrate it)
10% Formalin	dilute 16% Formalin with 1xPBS
Hematoxylin	(filtrate it)

Table 15: Reagents used for the ORO staining procedure

2.5 Immunofluorescent staining

The cells were cultivated on sterile coverslips in 12 well plates depending on the treatment time. Immunofluorescent staining protocol is performed over two days. After the specific treatment time the cells were fixed on the first day of the protocol. First, the cells were washed with 1×PBS, followed by incubation in 50 µL/well of 4% FA at 4°C for 20 minutes. After, the FA was carefully removed and disposed of it in designated chemical waste. The wells were rinsed two times with 1xPBS, discarding the first PBS wash in special waste as well. Next, cells were permeabilized by incubating them with 0.1% Triton-X in PBS for 20 minutes at room temperature. To prevent unspecific binding of antibodies, cells were blocked with 10% goat

serum (GS) and 0.1% Triton-X in PBS for 30 minutes at room temperature. Then, cells were incubated overnight at 4°C with the primary antibody (**Table 16**) diluted in blocking solution. On the second day, cells were washed three times for 10 minutes each in 1× PBS + 0.1% Tween-20 (1xPBST). This was followed by incubating the cells with the secondary fluorophore-labelled antibody (1:500) and DAPI (1:2000) in 1× PBST + 10% GS for no more than 1 hour at RT, protected from light with aluminum foil. Cells were then washed three more times in 1× PBST, followed by a final 10-minute wash in 1× PBS. Finally, the coverslips were mounted on microscopy slides using Prolong Gold Antifade reagent (Thermo Fisher Scientific P36930) and allowed the slides to dry overnight before imaging on the following days.

Epitope	Source	Product number	Animal of Origin	Dilution
H2BK5ac	Abcam	AB40886	Rabbit	1:1000
H3K27ac	Abcam	AB4729	Rabbit	1:1000
PEPCK (F-3)	Santa Cruz	sc-271029	Mouse	1:500
SCD (CD.E10)	Santa Cruz	sc-58420	Mouse	1:250
SCD (E8)	Santa Cruz	SC-515844	Mouse	1:250
SREBP1 (2A4)	Santa Cruz	SC-13551	Mouse	1:250
SREBP1	Novus Biologicals	NB100-2215	Rabbit	1:250
FASN	Santa Cruz	sc-55580	Mouse	1:500

Table 16:Primary antibodies used for immunofluorescent staining

Epitope	Source	Product Number	Animal of Origin	Dilution
Alexa Flour 546 mouse	Invitrogen	A-11003	Goat	1:500
Alexa Flour 546 Rabbit	Invitrogen	A-11010	Goat	1:500

Table 17: Secondary antibodies used for immunofluorescent staining

2.6 Microscopy

Images of the plates and slides stained with ORO or immunofluorescent dyes were acquired with an *inverted microscope and with the* slide scanner. For the plates, 4 to 8 pictures were acquired with the 10x objective of each well, for a broader coverage of the sample, at the inverted microscope. For the slides, the whole slide was pre-scanned with the 4x objective for sample detection. After, only selected areas were scanned in detail using 20x. The images were selected and analyzed with Fiji (ImageJ) and *Olympus OlyVIA* software. Further evaluation and figures were prepared in Microsoft Excel and *Power Point.*

2.7 Protein work

2.7.1 Total protein extraction from the SZ95 cells

The harvested cell pellets (find the procedure at **2.1.1.5**) were resuspended in the appropriate amount of desired Hunt Buffer (**Table 18**) with added protease inhibitors (**Table 19**). Next, the tubes with the cell suspension undergo three cycles of snap-frozen in liquid nitrogen and then thawed at room temperature. The third thawing step was performed during centrifugation for

30 minutes at 14000rpm and 4°C, and the SN was transfer into a new 1.5 ml Eppendorf tube. The concentration of the samples was measured using the **Bradford Protein Assay**. The lysates were either directly used or snap frozen and stored at -80°C.

Hunt Buffer	20 mM Tris/HCl pH 8.0
	100 mM Sodium chloride
	1 mM EDTA
	0.5% NP-40

Table 18: Hunt Buffer

Protease inhibitors	1x Complete Protease Inhibitor Cocktail (Roche)
	10mM Sodium fluoride (1M stock)
	100µM Orthovanadate (activated 5min at 95°C; 100mM stock)
	100µM Phenylmethyl sulfonyl fluoride (PMSF; 100mM stock)
	10µM Sodium molybdate (10mM stock)

Table 19: Protease Inhibitors

2.7.2 Bradford Protein Assay

The Bradford protein dye reagent concentrate (Bio-Rad, #5000006) was diluted 1:5 in dH2O. 1ml of the diluted Bradford solution was mixed with 1µl of sample, and all the samples were always measured in duplicates. The absorbance was measured at 595 nm using polystyrene cuvettes with the NanoDrop UV-vis spectrophotometer using 1ml diluted Bradford solution mixed with 1µl of respective sample buffer as blank. If outside 0.1-0.5 range, samples were dilute and remeasured. The protein concentration was calculated as follows:

$$\text{Protein concentration} = \left(\frac{\frac{\text{measurement 1} + \text{measurement 2}}{2}}{2} * dilution\ factor \right) * 10.$$

2.7.3 FLAG immunoprecipitation

For FLAG immunoprecipitation, the cell lysates obtained in **2.7.1** were used immediately.
At the beginning the desire amount of M2 Flag beads (Sigma Aldrich M8823-5ML) was prepared, 40 µl + 10% -> 44 µl of beads/sample. The beads were washed with 500µl 1xTBS (Tris-Buffered Saline) (**Table 20**)+Inhibitors (**Table 19**) and the tubes were inverted several times. Next, the tubes were placed on a magnetic rack, and the SN was carefully removed (taking new tip between each sample). The tubes were removed from the magnetic rack, new 500ul of 1xTBS+Inhinitors were added and the washing steps was repeated two more times. After the final washing step, the beads were placed onto the magnetic rack, and all the SN was removed. The beads were covered with blocking solution (1xTBS+Inh. +10% BSA (10mg/ml)) and incubated on the rotor for 30min at 4°C with 20rpm.
The desired cell lysates were prepared, using 300-500µg of protein per sample and filling each sample to a total volume of 300 µl with 1x Hunt buffer without sodium butyrate+inhibitors. After the 30 minutes, the beads were blocked and ready to use. The tubes were placed with the beads on the magnetic rack and the SN was aspirated. The beads were resuspended in the original volume, and 40ul of the beads/sample was aliquoted into designated tubes. The new aliquoted tubes were placed with the beads on the magnetic rack and the liquid was removed. After, the tubes with the beads were removed from the rack and protein extract (300µl) was added and put to incubate overnight at 4°C with 20rpm.

The following day the immunoprecipitated samples were spun down shortly, and if needed, transferred the SN to fresh Eppendorf tubes and stored at -80°C until further analysis. Next, the samples were washed tree times in 500 µl of 1x 500µl Hunt buffer without sodium butyrate +Inhibitors, twice for 5 minutes at 4°C at 20rpm and once for 15 minutes at 4°C at 20 rpm. The tubes were placed on the magnetic rack, and the SN was aspirated fully. 300ul of 1xHunt Buffer without sodium butyrate +Inhibitors was added, to carefully resuspend the beads and take 2x 50µl for **Activity** .
The beads were removed from the rest of the sample (~200µl) to use them for **Western Blotting (Wet-tank Transfer)**. The tubes were placed on the magnetic rack, and the SN was aspirated fully. The tubes were removed from the magnetic rack, spined shortly so that no beads are sticking to the wall of the tube and covered with 30ul of SDS loading dye without DTT (**Table 21**) to elute. Next, incubate for 5min at 60°C, and place the tubes again on a magnetic rack. 30µl of the eluate was transferred into a new tube. Now, 10µl of SDS loading dye with DTT (**Table 22**) was added into 30µl eluate and incubated at 95°C for 5min and loaded 15-20 µl on the gel and freeze the rest or store at -20°C until use.

10xTBS buffer	24.2% Tris Base
	80% NaCl
	diluted in dH2O
	Bring the pH to 7.6 with HCl,

Table 20: 10xTBS

SDS loading dye without DTT	100 mM Tris/HCl pH 6.8
	20% Glycerol
	0.01% Bromophenol blue
	5% SDS
	diluted in dH2O

Table 21:SDS loading dye without DTT

SDS loading dye with DTT	100 mM Tris/HCl pH 6.8
	20% Glycerol
	0.01% Bromophenol blue
	10% β - Mercaptoethanol
	5% SDS
	diluted in dH2O

Table 22: SDS loading dye with DTT

2.7.4 Activity Assay

Activity assays were performed in combination with **FLAG immunoprecipitation** experiments. After the 300µl of 1xHunt buffer without sodium butyrate+inhibitors was added, and the samples with beads were carefully resuspended, take 2x 50ul for the activity assay. Next, the SN is discarded, and the samples with beads were resuspended in 20µl of 1xHunt buffer without sodium butyrate +Inhibitors, and for the blank 20µl 1xHunt buffer without sodium butyrate+inhibitors was used in duplicates as well. 4µl of 3H acetate-labelled chicken erythrocyte histones (provided by Gerald Brosch, University of Innsbruck) were added to each sample and the blank, incubate the tubes at 30°C for 3 hours at 300 rpm. After the 3 hours of incubation 35µl of histone stop solution (**Table 23**) and 800µl of ethyl acetate were added to

each sample, followed by 15 seconds of vertexing and a centrifugation at 10000 rpm for 4 minutes in a swing centrifuge. 600µl of the upper organic phase from each sample were added to previously prepared 3ml of scintillation solution (**Table 24**). The samples were inverted several times and then measure the counts per minute on the Scintillation Counter at the following conditions:

- **Count Conditions:**

- Nuclide: 3H
- Quench Indicator: SIS
- External Std Terminator (sec): n/a
- Pre-Count Delay (min): 0.00
- Quench Set: n/a
- Count Time (min): 2.50
- Count Mode: Normal
- Assay Count Cycles: 1
- Repeat Sample Count: 1
- #Vials/Sample: 1
- Calculate % Reference: Off

- **Background Subtract:**

- Background Subtract: Off
- Low CPM Threshold: Off
- 2 Sigma % Terminator: Off

Regions	LL	UL
A	0.0	18.6
B	2.0	18.6
C	0.0	0.0

- **Count Corrections:**

- Static Controller: On
- Colored Samples: n/a
- Coincidence Time (nsec): 18
- Luminescence Correction: n/a
- Heterogeneity Monitor: n/a
- Delay Before Burst (nsec): 75

Histone stop solution	1M HCl
	0.4M Sodium acetate

Table 23: Histone stop solution

Scintillation Solution	5 g/l 2,5-Diphenyloxazole (PPO)
	0.5g/l 1,4-bis(5-phenyloxazol-2-yl) benzene) (POPO)
	Filled up with toluene

Table 24: Scintillation Solution

2.7.5 SDS-PAGE

Sodium Dodecyl Sulfate Polyacrylamide Gel Electrophoresis (SDS-PAGE) was used to separate proteins according to their molecular weight. We used the 10% precast polyacrylamide gel (Bio-Rad #4561033EDU) for use with Mini-PROTEAN Tetra Vertical Electrophoresis Cell (Bio-Rad).

First 20µg of protein extract were taken, filled with Hunt Buffer+Inhibitors up to 15µl, 5µl SDS with DTT were added, and everything was incubated at 95°C for 5min, then shortly spun down. Next, the samples were loaded on the stacking gel with a protein marker (Precision Plus Protein Dual Color Standards, #1610394, Bio-Rad). After electrophoresis in 1x running buffer (**Table 25**) at 15mA. When the samples reached the separation gel the current was increased to up to 20mA, separating the samples to the desired point. When two SDS pages were performed simultaneously the current was started at 30 mA and turned up to 40 mA once the samples have left the stacking gel.

10x Running Buffer (pH 8.3)	14.4% Glycine
	3% Tris base
	1% SDS
	diluted in dH2O

Table 25: 10x Running Buffer

2.7.6 Western Blotting (Wet-tank Transfer)

After SDS-PAGE the separated proteins samples were transferred from the gel onto a nitrocellulose membrane by wet-tank transfer. First, the stacking gel was removed, and assembled a “transfer sandwich” in the following order, from cathode (-) to anode (+), in a transfer cassette: sponge, Whatman filter paper, separation gel, nitrocellulose membrane, Whatman filter paper, sponge, like in **Figure 9**. Residual air between the membrane and the gel was removed by gently moving a roller over the assembly. Before assembling, all components were soaked in 1x transfer buffer (**Table 26**). The negatively charged proteins in the gel are pulled in an electric current toward the positively charged anode and into the membrane. Since the gel and membrane are sandwiched tightly during the procedure, the proteins maintain the separation they achieved during the SDS-PAGE electrophoresis.

After placing the cassette into a blotting tank (BioRad), it was filled with cold 1x transfer buffer. The proteins were blotted at 4°C for 2 hours with a constant current flow of 250mA.

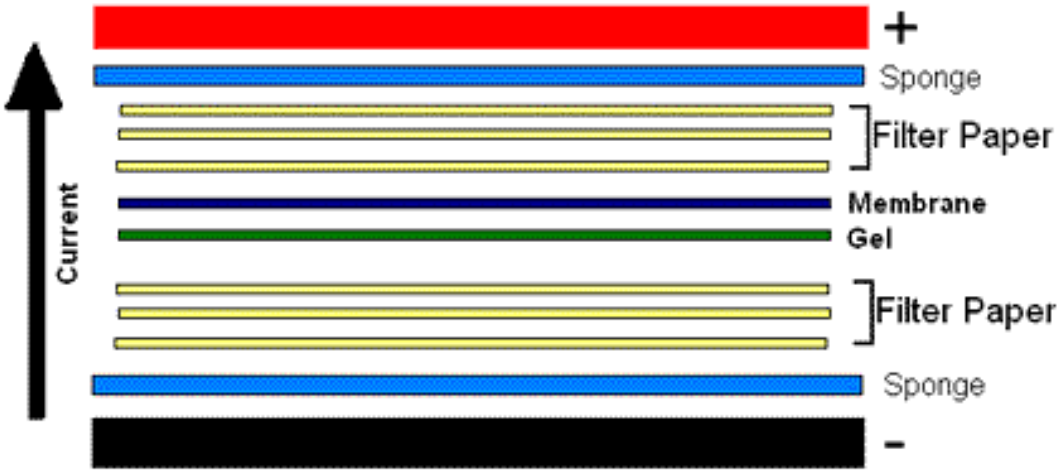

Figure 9: The components and structure of the "transfer sandwich"
https://www.antibodiesinc.com/pages/intro-to-western-blotting

Transfer buffer	3.024 g/L Tris/HCl, pH 8.0
	14.42 g/L Glycine
	20% Methanol (optional)
	diluted in dH2O

Table 26: Transfer buffer

2.7.7 Ponceau staining

To verify successful protein transfer, the nitrocellulose membrane was removed from the transfer cassette and incubated for 5 minutes with 1x Ponceau staining solution (**Table 27**). Following incubation, the Ponceau staining solution was retained for reuse, and the membrane was washed in dH_2O until red protein bands were visible against a white background. The membrane was then labelled and photographed.

10x Ponceau stain solution	2% Ponceau S
	30% Trichloroacetic acid
	30% Sulfosalicylic acid
	diluted in dH2O

Table 27: 10x Ponceau staining solution

2.7.8 Antibody incubation and immunodetection

Following Ponceau staining, each membrane was incubated for 30 minutes at room temperature in blocking solution (**Table 28**) with shaking, to prevent non-specific antibody binding. The desired primary antibody was diluted appropriately in 5ml of blocking solution in a falcon tube according to **Table 29**, and membranes were incubated overnight at 4°C on a rotor with the primary antibody solution.
The following day, membranes were washed three times in 1x PBST for 5 minutes each. Depending on the species of origin of the primary antibody, membranes were subsequently incubated with the appropriate secondary antibody, either goat IgG anti-rabbit or goat IgG anti-mouse (**Table 30**), diluted in 5% milk in 1x PBS, for 1 hour at room temperature while shaking.

Membranes were then washed again three times in 1x PBST for 5 minutes each. Chemiluminescent detection was performed using either ECL or super ECL solution as a substrate, selected based on the primary antibody used. Detection reagents 1 and 2 were mixed at a 1:1 ratio and pipetted directly onto the membrane or diluted 1:3 with dH_2O prior to application in the case of the super ECL solution. Antibody-antigen signals were visualised using the Fusion FX detection system.

Blocking Solution	5% Milk powder
	0.01% Sodium azide
	diluted in 1xPBST

Table 28: Blocking solution

Epitope	Source	Product number	Animal of origin	Molecular weight
HDAC1 Sat 208	Seiser lab	-	Rabbit	~55kDa
HDAC1 10E2	Seiser lab	-	Mouse	~55kDa
HDAC2 3F3	Seiser lab	-	Mouse	56kDa
FLAG M2	Sigma Aldrich	F 1804	Mouse	17kDa
ß-actin	Abcam	ab8227	Mouse	40kDa
Vinculin	Cell signalling	13901	Rabbit	100kDa
GAPDH	Cell signalling	5174S	Rabbit	37kDa
CoREST	Millipore	07-455	Rabbit	66kDa
SAP30	Abcam	ab231804	Rabbit	30kDa
Sin3A	Santa Cruz	sc-5299	Mouse	160kDa
PEPCK (F-3)	Santa Cruz	sc-271029	Mouse	70kDa
SCD (CD.E10)	Santa Cruz	sc-58420	Mouse	40kDa
SCD(E8)	Santa Cruz	SC-515844	Mouse	40kDa
SREBP (2A4)	Santa Cruz	SC-13551	Mouse	125/68kDa
SREBP1	Novus Biologicals	NB100-2215	Rabbit	122/65kDa
FASN	Santa Cruz	sc-55580	Mouse	250-272kDa
MTA2	Sigma Aldrich	M7569	Mouse	75kDa

Table 29: Primary antibodies for protein detection

Antibody	Source	Product number	Animal	Dilution
Anti-mouse-HRP	Jackson ImmunoReseach	115-035-174	Goat	1:10000
Anti-rabbit-HRP	Jackson ImmunoReseach	111-035-003	Goat	1:3000

Table 30: secondary antibodies for protein detection

2.8 Cleavage Under Targets & Release Using Nuclease (CUT&RUN)

2.8.1 Buffer preparation and ConA Beads activation

For every CUT&RUN experiment all buffers were prepared fresh on Day 1. First the protease inhibitor tablet was dissolved in molecular biology-grade water to a working concentration of 25X stock. After buffer preparation, the remaining 25X stock can be stored for 12 weeks at -20˚C. Next, the Wash Buffer was prepared by mixing the reagents mentioned in **Table 31**, in the specific concentrations, and store it at the RT for use on Day 1. The Cell Permeabilization Buffer was prepared second, with reagents and concentrations described **Table 32**, stored at 4°C for use on Day 2. The third buffer is Antibody Buffer was prepared according to **Table 33**, store on ice for use on Day 1.

Wash Buffer	1x protease inhibitor
	0.5mM Spermidine
	Dissolve in Pre-Wash Buffer

Table 31: Wash Buffer-reagents final concentration

Cell Permeabilization Buffer	0.01% Digitonin
	Dissolve in Wash Buffer

Table 32:Cell Permeabilization Buffer-reagents final concentration

Antibody Buffer	2mM EDTA
	Dissolve in Cell Permeabilization Buffer

Table 33: Antibody Buffer-reagents final concentration

For the activation of the Concanavalin A (ConA) beads, the bead slurry was gently resuspended, and 11 µl/sample was transferred to a 1.5 ml Eppendorf tube. The tube was placed on a magnetic rack until the slurry cleared and the supernatant was removed. Cold Bead Activation Buffer (provided in the kit) was added at 100 µl per sample and mixed by pipetting. The tube was returned to the magnetic rack until the slurry cleared and the supernatant was removed. This washing step was repeated two more times. Following the final wash, the beads were resuspended in 11 µl/sample of cold Bead Activation Buffer, and 10 µl per sample of the activated bead slurry was aliquoted into 8-strip tubes. Beads were kept on ice and used within four hours of activation.

2.8.2 EpiCypher CUTANA CUT&RUN Protocol

Cell plates prepared under the treatment conditions described in the **2.3** section were harvested following the same protocol as described in **2.1.1.2**. Following the cell count, $0.5x10^6$ cells per sample were transferred to a 1.5 ml Eppendorf tube, pelleted by centrifugation for 3 minutes at 600x g at room temperature, and the supernatant was discarded. Cells were resuspended in 100µl Wash Buffer, centrifuged again for 3 minutes at 600x g at room temperature, and the supernatant was discarded. This washing step was repeated two more times. Following the final wash, cells were resuspended in 100µl Wash Buffer and 100µl of the washed cell suspension was aliquoted into each 8-strip tube containing 10µl of activated bead slurry. Samples were gently vortexed and incubated for 10 minutes at room temperature to allow cells to adsorb onto the activated ConA beads.

For antibody binding, the 8-strip tubes were placed on a magnetic rack until the slurry cleared and the supernatant was removed. Cold Antibody Buffer (50µl) was added to each sample and samples were gently vortexed. Primary antibody was added to each reaction at the desired concentration. For control reactions, 1µl of the respective H3K4me3 and IgG control antibody was added. Samples were gently vortexed and incubated overnight at 4˚C on a nutator with tube caps elevated to allow gentle rocking.
On Day 2, following the overnight incubation, the tubes were placed on a magnetic rack until the slurry cleared and the supernatant was removed. While the beads were retained on the magnet, 250µl of cold Digitonin Buffer, prepared the day prior, was added directly to the beads of each sample and the supernatant was removed. This washing step was repeated two more times. Following the final wash, 50µl of cold Digitonin Buffer was added to each 8-strip tube and samples were gently vortexed. For pAG-MNase binding, 2.5µl of pAG-MNase was added to each sample and samples were gently vortexed. Samples were incubated for 10 minutes at room temperature, after which the 8-strip tubes were returned to the magnetic rack, 250µl of cold Digitonin Buffer was added directly to each sample, and the supernatant was removed. This washing step was repeated two more times. Finally, 50µl of cold Digitonin Buffer was added to each sample and samples were gently vortexed.
For targeted chromatin digestion and release, the 8-strip tubes were placed on ice and 1 µl of 100mM $CaCl_2$ was added to each sample to activate the MNase tethered to chromatin, followed by gentle vortexing. Samples were incubated on a nutator for 2 hours at 4˚C. Following incubation, 33µl of Stop Buffer, provided in the kit to terminate MNase activity by chelating Ca^{2+} ions, was added to each sample and samples were gently vortexed. The 8-strip tubes were incubated for 10 minutes at 37˚C in a thermocycler to release chromatin into the supernatant and degrade RNA. Tubes were placed on a magnetic rack until the slurry cleared and the supernatant was transferred to new 1.5ml Eppendorf tubes. DNA was subsequently purified using the NEB Monarch® DNA Cleanup Kit.

2.8.3 DNA purification

Fresh 85% ethanol (EtOH) was prepared at 500 µl per reaction using 100% EtOH and molecular biology-grade water. The SPRIselect reagent was vortexed to fully resuspend, and 118µl was slowly added to each tube, for size selection, to avoid adaptor dimers. Samples were mixed thoroughly by pipetting and vortexing to achieve an even resuspension, quickly spined, and incubated for 5 minutes at room temperature. Tubes were then placed on a magnetic rack for 2–5 minutes at room temperature until the solution cleared, and the supernatant was removed without disturbing the beads. While the tubes remained on the magnetic rack, 180µl of 85% EtOH was added directly onto the SPRIselect reagent and beads, and the supernatant was removed. This washing step was repeated one more time, after which the tubes were removed from the magnetic rack, quickly spined with caps facing inward to avoid dislodging the beads, returned to the magnetic rack, and residual EtOH was removed.
Tubes were removed from the magnetic rack, and beads were air-dried with caps open for 2-3 minutes at room temperature. Beads that appeared damp and matte brown were considered adequately dried; beads that appeared crackly or light brown were considered over-dried. To elute the DNA, 17µl of 0.1x TE Buffer was added to each reaction, beads were fully resuspended by pipetting and vortexing, tubes were quickly spined, and samples were incubated for 2 minutes at room temperature. Tubes were placed on a magnetic rack for 2 minutes at room temperature, and 15µl of CUT&RUN-enriched DNA was transferred to new 8-strip tubes. DNA concentration was quantified using 1µl of eluate with the Qubit fluorometer and the 1x dsDNA HS Assay Kit. DNA was stored at −20˚C until library preparation.

2.8.4 Library prep

Illumina sequencing libraries were prepared using the NEBNext Ultra™ II Library Prep Kit for Illumina. For the end repair step, 5–10ng of purified CUT&RUN-enriched DNA was transferred to a new 8-strip tube and the final volume was adjusted to 25µl with 0.1x TE Buffer. An End Repair Master Mix was prepared for the required number of reactions by combining the reagents listed in **Table 35**, gently vortexed, quickly spined, and kept on ice. Five microliters of End Repair Master Mix were added to 25µl of CUT&RUN DNA in each 8-strip tube, pipetted up and down five times to clear the tips, gently vortexed, and quickly spined. The 8-strip tubes were placed in a thermocycler and the end repair program described in **Table 34** was run with the heated lid set to ≥75˚C. Following the program, tubes were quickly spined to collect liquid at the bottom and placed immediately on ice.

Step	Temperature	Time	Cycles	Notes
1	20˚C	20 min	1	Reaction temperature
2	65 ˚C	30 min	1	Enzyme inactivation
3	4-12 ˚C	∞	1	Hold temperature

Table 34: thermocycler running program

End Repair Master Mix	4.2µl End Prep Buffer
	1.8µl End Prep Enzyme

Table 35: End Repair Master Mix-reagents amount/reaction

For adapter ligation and U-excision, a Ligation Master Mix was prepared according to the reagents and volumes listed in **Table 36**, gently vortexed, quickly spined, and kept on ice. To each 8-strip tube, 1.25µl of 1.5µM Adapter for Illumina and 15.5µl of Ligation Master Mix were added while tubes were kept on ice. Samples were incubated in a thermocycler without a heated lid for 15 minutes at 20˚C. Tubes were removed from the thermocycler to a room temperature rack and 1µl of U-Excision Enzyme was added to each tube. Samples were gently vortexed and quickly spined. Tubes were placed in a thermocycler with a heated lid set to ≥47˚C, with the block temperature set to 37˚C, and incubated for 15 minutes. Tubes were then removed from the thermocycler and quickly spined.

Ligation Master Mix	16.5µl Ligation Mix
	0.55µl Ligation Enhancer

Table 36: Ligation Master Mix-reagents amount/reaction

For DNA cleanup, the DNA Purification Beads were vortexed thoroughly to resuspend, and 47.75µl was slowly added to each tube in the 8-strip format and mixed thoroughly. Samples were quickly spined and incubated for 5 minutes at room temperature. Tubes were placed on a magnetic rack for 2-5 minutes at room temperature until the solution cleared, and the supernatant was removed without disturbing the beads. While tubes remained on the magnetic rack, 180µl of 85% EtOH was added directly onto the beads, and the supernatant was carefully removed. This washing step was repeated one more time. Tubes were removed from the magnetic rack, quickly spined with caps facing inward to avoid dislodging the beads, returned to the magnetic rack, and residual EtOH was removed. Tubes were removed from the magnetic rack, caps were left open, and beads were air-dried for 2-3 minutes until they

appeared damp and matte brown. To elute the target DNA, 12µl of 0.1x TE Buffer was added to each reaction, beads were fully resuspended by pipetting and vortexing, tubes were quickly spined, and samples were incubated for 2 minutes at room temperature. Tubes were placed on the magnetic rack for 2 minutes at room temperature and 10.5µl of eluted DNA was transferred to new 8-strip tubes.
For PCR indexing, a unique pair of i5 and i7 index primers was assigned to each reaction. To each 10.5µl CUT&RUN DNA sample, 1µl of the assigned i7 primer, 1µl of the assigned i5 primer, and 12.5µl of Hot Start 2x PCR Master Mix were added individually and in order. Reactions were mixed by vortexing and quickly spined to collect liquid. Tubes were placed in a thermocycler with a heated lid set to 105˚C and PCR amplification was performed using the parameters described in **Table 37**.

Step	Temperature	Time	Cycles	Notes
1	98˚C	45 sec	1	Hot start activation of DNA Polymerase
2	98˚C	15 sec	14	DNA melting
3	60˚C	10 sec		Hybrid annealing/extension
4	72˚C	60 sec	1	Final extension
5	4-12˚C	∞	1	Hold temperature

Table 37: Thermocycler running program

For the final PCR cleanup, the DNA Purification Beads were vortexed to resuspend and 25µl was slowly added to each PCR tube in the 8-strip format. Samples were mixed thoroughly by vortexing and pipetting, quickly spined, and incubated for 5 minutes at room temperature. Tubes were placed on a magnetic rack for 2-5 minutes at room temperature until the solution cleared, and the supernatant was removed without disturbing the beads. While tubes remained on the magnetic rack, 180µl of 85% EtOH was added directly onto the beads and the supernatant was removed. This washing step was repeated one more time. Tubes were removed from the magnetic rack, quickly spined with caps facing inward to avoid dislodging the beads, returned to the magnetic rack, and residual EtOH was removed. Tubes were removed from the magnetic rack, caps were left open, and beads were air-dried for 2-3 minutes until they appeared damp and matte brown. To elute the sequencing libraries, 12µl of 0.1x TE Buffer was added to each reaction, beads were fully resuspended by pipetting and vortexing, tubes were quickly spined, and samples were incubated for 2 minutes at room temperature. Tubes were placed on the magnetic rack for 2 minutes at room temperature and 10.5µl of eluted CUT&RUN sequencing libraries was transferred to new 8-strip tubes. Libraries were stored at −20˚C until fragment analysis and sequencing, both of which were performed at the Vienna Biocenter Next Generation Sequencing Facility. And before sending out for sequencing, libraries were measured via Qubit for DNA concentration.

2.9 Work with DNA

2.9.1 Wizard Genomic DNA Purification Kit

Genomic DNA was isolated from H141A SZ95 sebocytes using the Wizard® Genomic DNA Purification Kit (Promega, #A1120) according to the manufacturer's instructions for tissue culture cells. The harvested cell pellets (find the procedure at **2.1.1.5**) were resuspended in 600 µl of Nuclei Lysis Solution by pipetting and incubated at 65°C for 15 minutes to achieve complete cell lysis. RNA was subsequently removed by addition of 3 µl RNase A Solution, followed by gentle mixing and incubation at 37°C for 15 minutes. After cooling to room temperature, proteins were precipitated by the addition of 200 µl of Protein Precipitation Solution and vigorous vortexing. The protein precipitate was removed by centrifugation, and the DNA-containing supernatant was transferred to a fresh tube containing room-temperature isopropanol and mixed by inversion until a visible DNA mass formed. The DNA pellet was collected by centrifugation, washed with 70% ethanol, air-dried, and rehydrated in DNA Rehydration Solution overnight at room temperature.

2.9.2 Measuring DNA concentration

DNA concentrations were determined spectrophotometrically using the NanoDrop UV-vis spectrophotometer. DNA Rehydration Solution (Promega, #A7963) was used as blank, and 1 µl of each sample was measured individually. Absorbance at 260 nm was recorded to calculate DNA concentration in ng/µl, and absorbance ratios at 260/280 nm and 260/230 nm were assessed to evaluate sample purity.

2.9.3 Nested PCR

Nested PCR was performed using two sets of primers (**Table 38**) and two sequential amplification reactions to increase PCR specificity for later sequencing of the amplified catalytic center. Prior to PCR, genomic DNA concentrations were measured, and samples of higher concentration were diluted with dH2O to a uniform concentration of 100 ng/µl.

For the first PCR reaction, the forward primer annealed upstream of the HDAC1 catalytic center, and the reverse primer annealed downstream of the FLAG tag within the SZ95 genomic DNA, yielding an amplicon of 2900 bp. The reverse primer was designed to be complementary to a genomic region outside the vector construct to ensure specificity. Reactions were prepared in 0.2 ml tubes containing 23 µl of Master mix (**Table 39**) and 2 µl of isolated gDNA, with dH2O substituted for the DNA template in the negative control. Amplification was carried out in a Bio-Rad T100 Thermal Cycler according to the conditions listed in **Table 40**.

For the second PCR reaction, the forward primer annealed upstream of position 141 of the HDAC1 catalytic center and the reverse primer annealed closely downstream of it, yielding a smaller amplicon of 314 bp. Reactions were prepared in 0.2 ml tubes containing 23 µl of Master mix (**Table 41**) and 2 µl of first-round PCR product diluted 1:1000 in dH2O, with dH2O substituted for the DNA template in the negative control. Amplification was performed in a Bio-Rad T100 Thermal Cycler according to the conditions listed in **Table 42**.

Nested PCR	Primers	Sequence	Company	Product size
1st PCR reaction	mHD1-F1 (forward)	5'CAATGCTGAGGAGATGACCA	Sigma Aldrich	2900 bp
	3'end_AAVS1_R2 (reverse)	5'AGAAGGATGCAGGACGAGAA		
2nd PCR reaction	mHD1-F (forward)	5'GCGTTCTATTCGCCCAGATA	Sigma Aldrich	314 bp
	mHD1-R (reverse)	5'CGCCATGGTGAATATCAATG		

Table 38: Primer specificities and expected amplicon sizes for nested PCR reactions

1x Master mix for the first nested PCR reaction	14,75µl dH2O
	5µl 5x Q5 Reaction Buffer(#B9027S)
	0,5 µl dNTPs Mix (10mM) (#U151B)
	1,25µl mHD1-F1 (10µM)
	1,25µl 3'end_AAVS1_R2 (10µM)
	0,25µl Q5 High-Fidelity DNA Polymerase (#M0491S)

Table 39: Master Mix-reagents amount/reaction for the first nested PCR reaction

PCR conditions		
Temperature	**Time**	**Cycles**
98°C	30 s	1
98°C	10 s	35
57°C	30 s	35
72°C	90 s	35
72°C	2 min	1
10°C	∞	

Table 40: Thermocycler running program for the first reaction of the nested PCR

1x Master mix for the second nested PCR reaction	14,75 µl dH2O
	5 µl 5x Q5 Reaction Buffer(#B9027S)
	0,5 µl dNTPs Mix (10mM) (#U151B)
	1,25 µl mHD1-F (10µM)
	1,25 µl mHD1-R (10µM)
	0,25 µl Q5 High-Fidelity DNA Polymerase (#M0491S)

Table 41:Master Mix-reagents amount/reaction for the second nested PCR reaction

PCR conditions		
Temperature	**Time**	**Cycles**
98°C	30 s	1
98°C	10 s	35
60°C	30 s	35
72°C	20 s	35
72°C	2 min	1
20°C	∞	

Table 42: Thermocycler running program for the second reaction of the nested PCR

2.9.4 Gel electrophoresis

To confirm successful amplification of the target sequence, PCR products from both the first and second reactions were analyzed by gel electrophoresis. A 1.5% agarose gel was prepared by dissolving 1.5 g of agarose (#LQ-163044-0500) in 100 ml of 1x TAE buffer by boiling, cooling to 60°C, and supplementing with 2 µl of peqGREEN DNA/RNA dye (#37-5010) prior to casting in a gel tray fitted with a well comb. The gel was allowed to solidify for 20–30 minutes at room temperature, after which the tray was transferred to a gel box filled with 1x TAE buffer. Prior to loading, 10 µl of each PCR sample was mixed with 2 µl of 6x DNA Loading Dye (#R0611). A 1 kb Plus DNA Ladder (#N3200S) was included as a molecular weight marker. Electrophoresis was performed at 90 V for 45 minutes.

10xTAE buffer	400mM Tris-Acetate
	20mM EDTA
	diluted in dH2O, adjusted pH to 8.5

Table 43: 10xTAE buffer

2.9.5 Sanger sequencing

Following confirmation of successful nested PCR amplification of the 314 bp target sequence of the HDAC1 catalytic center, second-round PCR products were submitted for Sanger sequencing. Samples were sent diluted in ddH2O together with the forward primer mHD1-F (10 µM), which was used for forward sequencing.
Sequencing results were analyzed and aligned against the *Mus musculus Hdac1* mRNA reference sequence (NCBI Reference Sequence: NM_008228.3) using Nucleotide BLAST. Chromatogram data were additionally inspected using SnapGene Viewer software.

2.10 AI usage statement

Artificial intelligence (AI) tools were employed at various stages of the writing process in this thesis. Specifically, AI was used to support the rephrasing and restructuring of text passages, the correction of grammatical errors, and the overall stylistic refinement of academic language. Additionally, DeepL was used to translate the abstract into German.
All AI-generated suggestions were critically reviewed, evaluated, and adapted by the author. The intellectual content, scientific reasoning, experimental design, data interpretation, and conclusions presented in this thesis remain exclusively the work of the author and the supervisor.
The following AI tools were used: Perplexity, Claude (Anthropic), ChatGPT (OpenAI), and DeepL.

3 RESULTS

3.1 Regulation of lipid synthesis in the human sebocyte cell line SZ95

3.1.1 Effects of Insulin, TO901317 and MS-275 on expression of lipid-associated proteins

Previous experiments in our lab have shown that in SZ95 sebocytes lipid droplet formation can be induced by treatment with insulin and the LXR agonist TO901317, as well as by inhibition of class I HDACs using Entinostat (MS-275). The combination of all three treatments results in the highest lipid accumulation. Furthermore, the combined treatment of SZ 95 cells resulted in upregulation of lipid-associated genes on the transcriptional level. To test, whether stimulation of cells also results in upregulation of enzymes and factors on the protein level, SZ 95 cells were stimulated with insulin+TO901317 and insulin+TO901317+MS-275 for 72h. Protein lysates were harvested and subjected to Western Blotting using antibodies specific for SREBP1, SCD, and PPARγ (**Figure 10**). Equal protein loading was confirmed by Ponceau staining.

An increase in SREBP1 and SCD protein levels was observed following insulin+TO901317 treatment, with a further increase upon addition of MS-275. In contrast, PPARγ protein levels decreased with insulin+TO901317+MS-275 treatment and showed an even greater reduction with insulin+TO901317 alone.

In addition, the efficiency of PPARγ and SREBP siRNA in mediating knockdown was tested showing a partial KD, indicating their potential suitability for future experiments (**Figure 10**, right lanes).

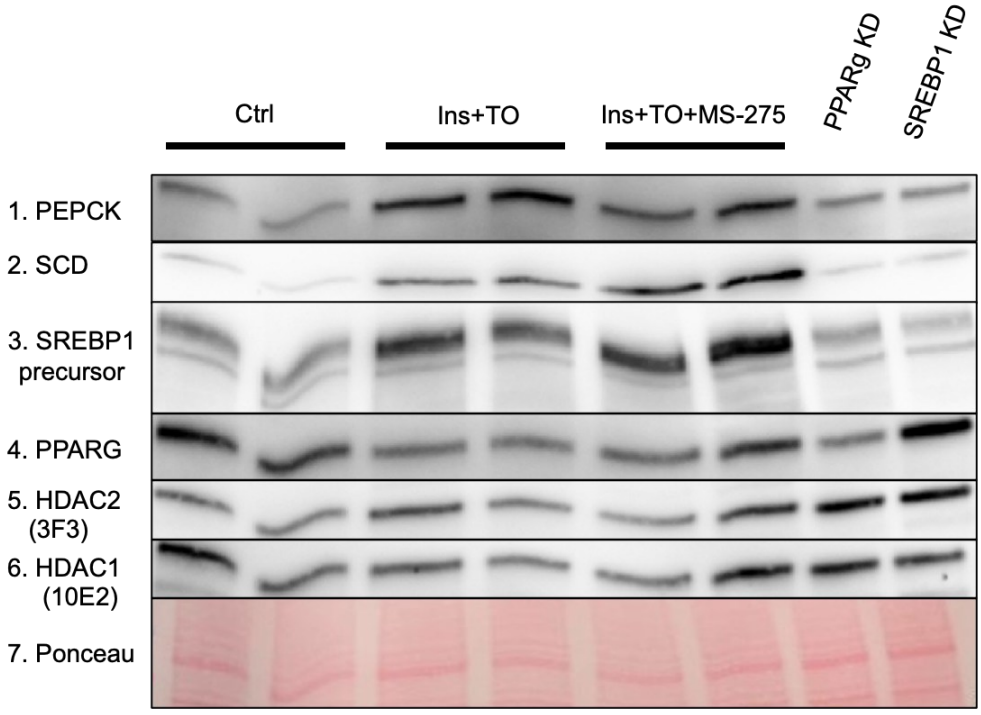

Figure 10: Regulation of lipid associated genes after stimulation of SZ95 cells

Western blot analysis lysates from SZ95 cells treated with DMSO (Control), Insulin+TO(TO901317), and Insulin+TO(TO901317) +MS-275. Additionally, lysates from siRNA-mediated knockdown of PPARγ and SREBP1 were tested. Ponceau staining was used as loading control.

3.1.2 Formation of lipid droplets depends on p300 activity

Previous work with SZ95 sebocytes showed that lipid droplet formation is strongly enhanced by combined insulin+TO901317 stimulation and with MS-275. To assess whether p300 activity contributes to the lipid-accumulating effect observed under MS-275 treatment, ORO staining was used to quantify lipid droplet formation after chemical inhibition of p300.

SZ95 cells were seeded in 12-well plates and treated for the indicated period under four conditions: DMSO 1:1000 (control), insulin+TO901317, insulin+TO901317+MS-275, and insulin+TO901317+MS-275+A-485 (p300 inhibitor). Each condition was performed with three biological replicates. Cells were stained with ORO to visualize neutral lipids and counterstained with hematoxylin to label nuclei.

Representative images (**Figure 11**) showed the lipid droplets as red dots, with nuclei appearing bluish due to hematoxylin staining. The insulin+TO901317+MS-275 condition displayed the strongest lipid droplet accumulation compared to the other treatment groups. Quantification of the mean ORO-stained area per nucleus (**Figure 12**) confirmed that insulin+TO901317+MS-275 significantly increased lipid accumulation relative to both DMSO and insulin+TO901317 alone. Addition of A-485 significantly reduced lipid droplet formation compared to insulin+TO901317+MS-275 ($p < 0.01$, one-way ANOVA).

Together, these results indicated that p300 activity is at least partially required for lipid droplet accumulation in SZ95 cells under the present conditions.

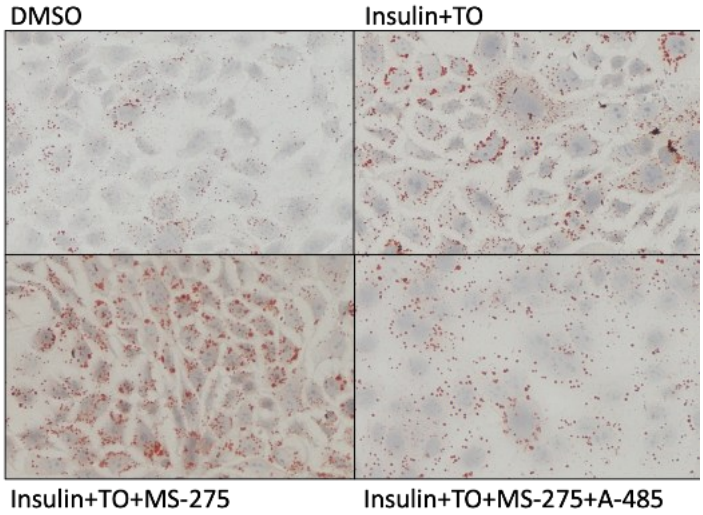

Figure 11: ORO-stained SZ95 cells under multiple treatment conditions

Representative microscope images of ORO-stained SZ95 cells under the following conditions: DMSO (control), insulin+TO (TO901317), insulin+TO+MS-275, and insulin+TO+MS-275+A-485. Images show lipid droplets (red) in the cytoplasm and cell nuclei counterstained with hematoxylin (blueish).

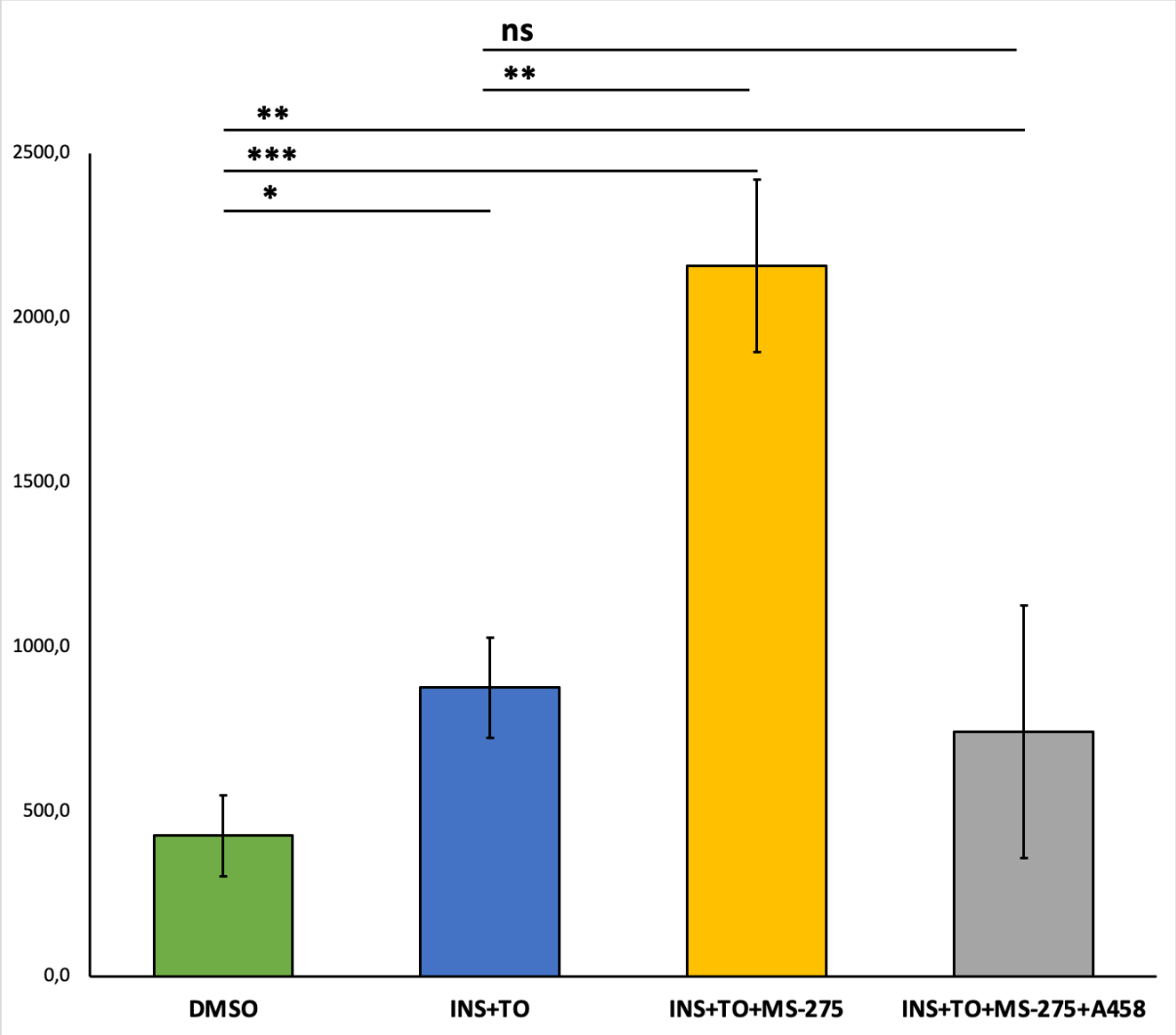

Figure 12: Quantification of the ORO staining in SZ95 cells under the four treatment conditions

*Mean ORO-stained area per nucleus is shown for cells treated with DMSO (control), insulin+TO (TO901317), insulin+TO+MS-275, and insulin+TO+MS-275+A-485. Data represent means ± SD from three independent replicates. Statistical significance: *p < 0.05; **p < 0.01; **p < 0.01 vs. DMSO and vs. insulin+TO (one-way ANOVA).*

3.1.3 SiRNA-mediated knockdown of HDAC1, HDAC2 and HDAC3 in SZ95 cells

3.1.3.1 Validation of knockdown efficiency

Previous experiments showed that chemical inhibition of class I HDACs with the class I–selective inhibitor MS-275 induced strong lipid droplet formation in SZ95 sebocytes. To identify which individual class I HDAC isoform may be critical for this phenotype, siRNA-mediated knockdown of HDAC1, HDAC2, and HDAC3 was established and optimized.
Two siRNA transfection protocols differing in the lipofectamine-to-siRNA ratio were compared. SZ95 cells were seeded in 6 cm plates with biological duplicates for all conditions. Western blot analysis confirmed successful knockdown of HDAC1, HDAC2, and HDAC3 under both protocols after 48h (**Figure 13, Figure 15, Figure 17**). Protein loading was consistent across all samples, as demonstrated by stable GAPDH expression (housekeeping control) and uniform Ponceau S staining.

In addition to the primary knockdown effects, a compensatory upregulation of class I HDACs was observed: HDAC1 knockdown resulted in compensatory upregulation of HDAC2 expression in the first blot (**Figure 13, Figure 14**), while HDAC2 knockdown led to enhanced HDAC1 expression in the second blot (**Figure 15, Figure 16**). Based on the robust and reproducible knockdown efficiency and the lower amount of siRNA used, future experiments were conducted using the "L" protocol, as described in the "**Materials and Methods" section**.
Quantification was performed by comparing intensities of specific bands to the loading control (GAPDH) to correct for differences in protein loading across samples. Subsequently, all values were normalized relative to the DMSO 1:1000 control group to express data as fold changes compared to the untreated control.

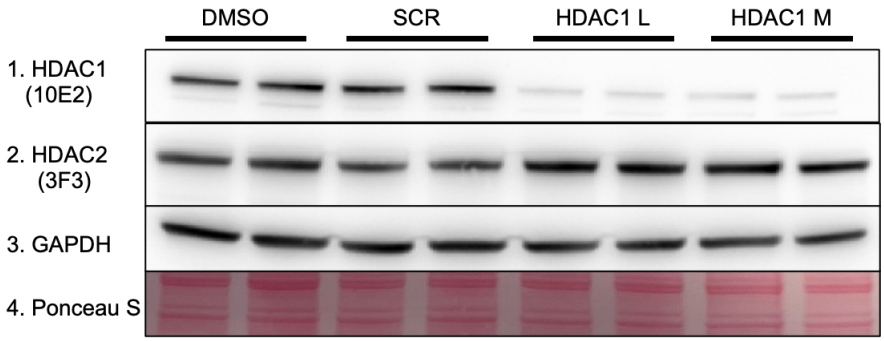

Figure 13: Evaluation of HDAC1 siRNA-mediated knockdown

Western blot analysis lysates from SZ95 cells treated with DMSO 1:1000, SCR and HDAC1 KD. GAPDH and Ponceau S was used as loading controls.

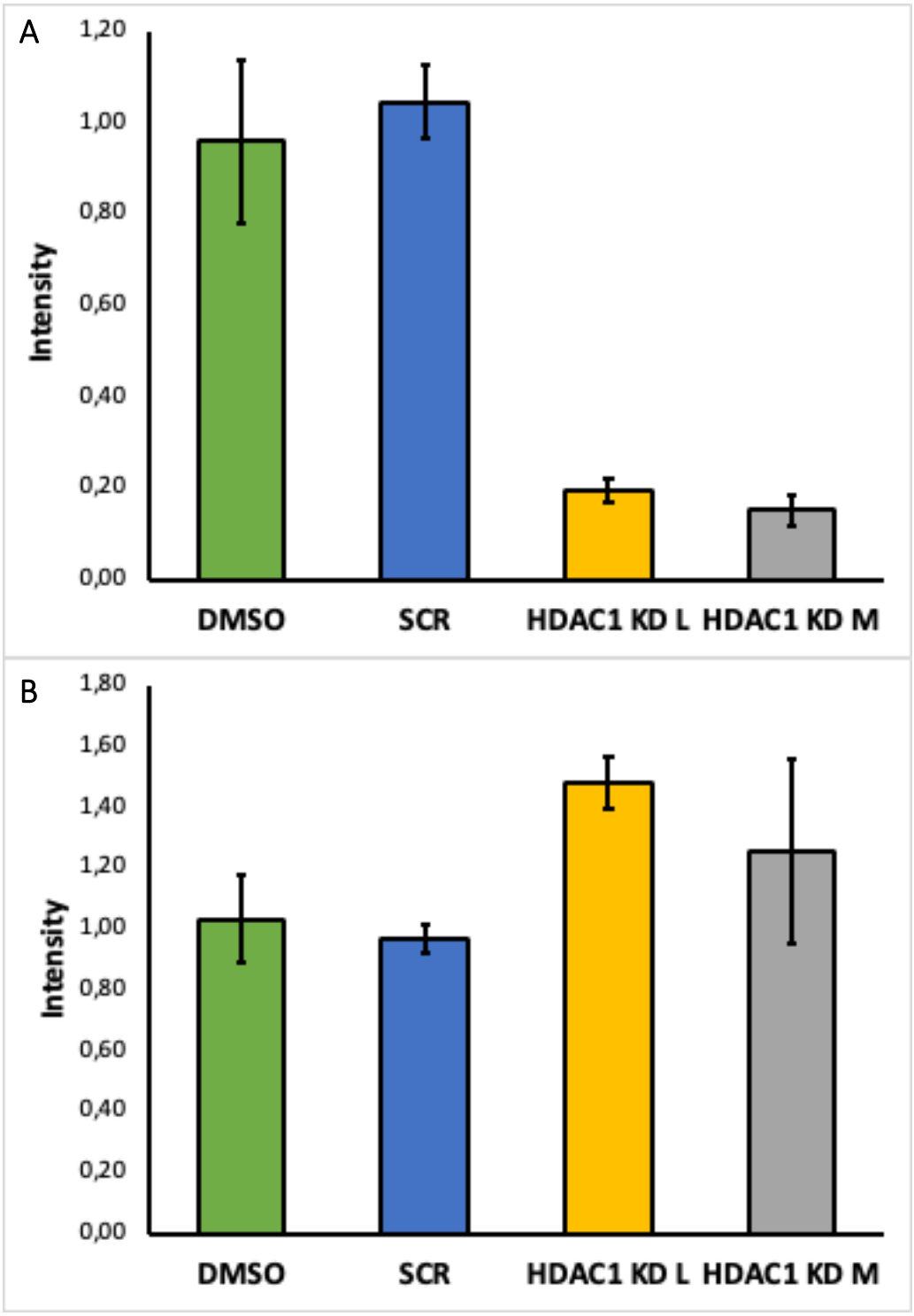

Figure 14:Quantification of HDAC protein levels by Western blot analysis following HDAC1 knockdown

(A) HDAC1 protein levels were strongly reduced in both HDAC1 KD L and HDAC1 KD M conditions compared to the CTRL and SCR samples. (B) HDAC2 protein levels were elevated in both HDAC1 KD L and HDAC1 KD M conditions relative to CTRL and SCR, suggesting a compensatory upregulation of HDAC2 upon HDAC1 knockdown. Data are represented as mean intensity values ± standard deviation for each experimental group.

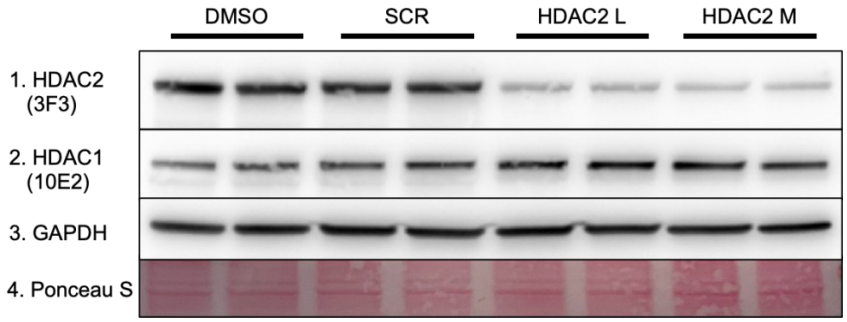

Figure 15: Evaluation of HDAC2 siRNA-mediated knockdown

Western blot analysis lysates from SZ95 cells treated with DMSO 1:1000, SCR and HDAC2 KD. GAPDH and Ponceau S was used as loading controls.

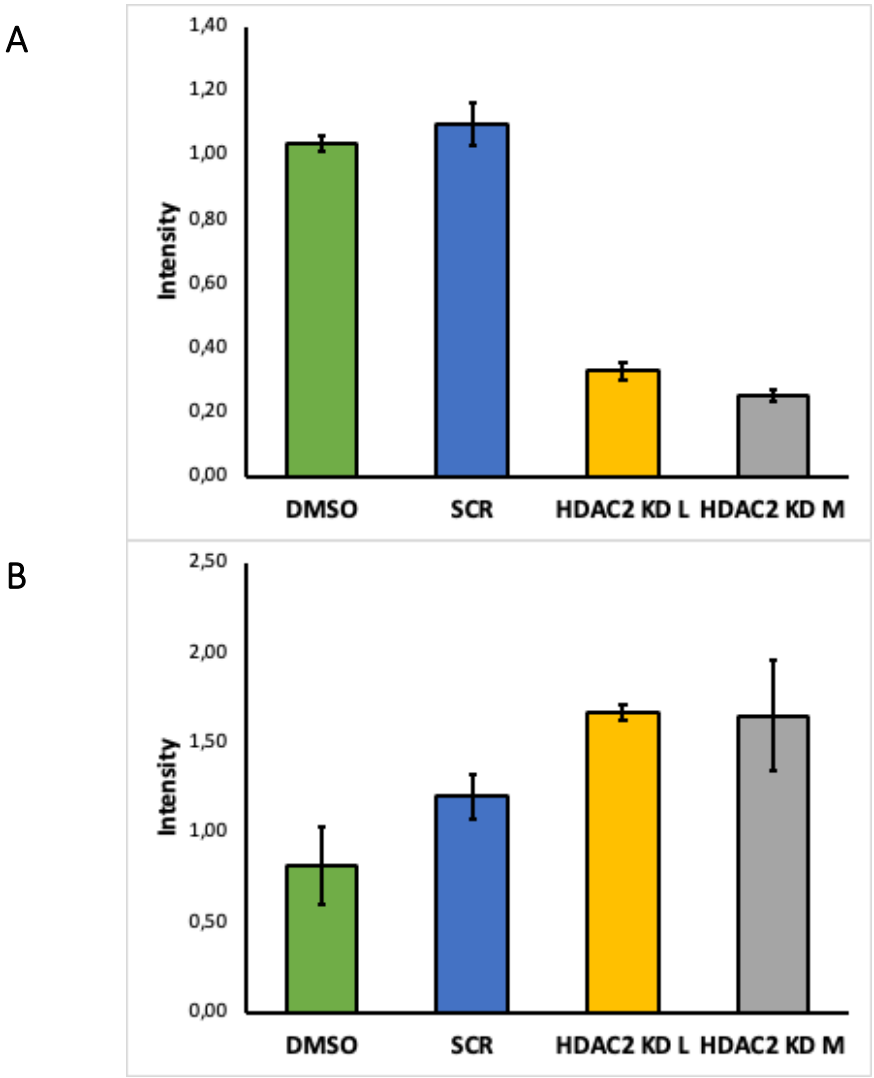

Figure 16:Quantification of HDAC protein levels by Western blot analysis following HDAC2 knockdown

(A)HDAC2 protein levels were strongly reduced in both HDAC2 KD L and HDAC2 KD M conditions compared to the CTRL and SCR samples. (B) HDAC1 protein levels were elevated in both HDAC2 KD L and HDAC2 KD M conditions relative to CTRL and SCR, suggesting a compensatory upregulation of HDAC1 upon HDAC2 knockdown. Data are represented as mean intensity values ± standard deviation for each experimental group.

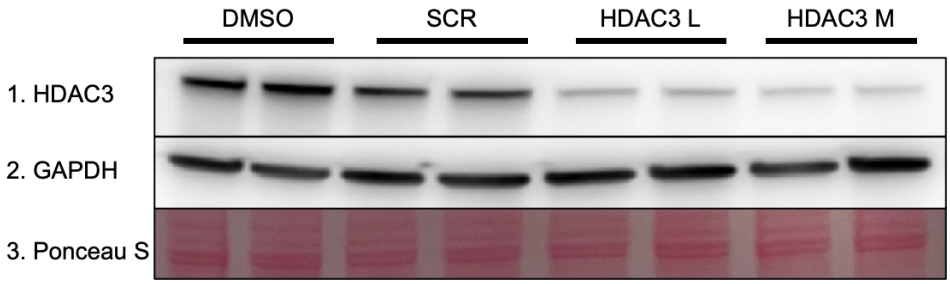

Figure 17: Evaluation of HDAC3 siRNA-mediated knockdown

Western blot analysis lysates from SZ95 cells treated with DMSO 1:1000, SCR and HDAC3 KD. GAPDH and Ponceau S was used as loading controls

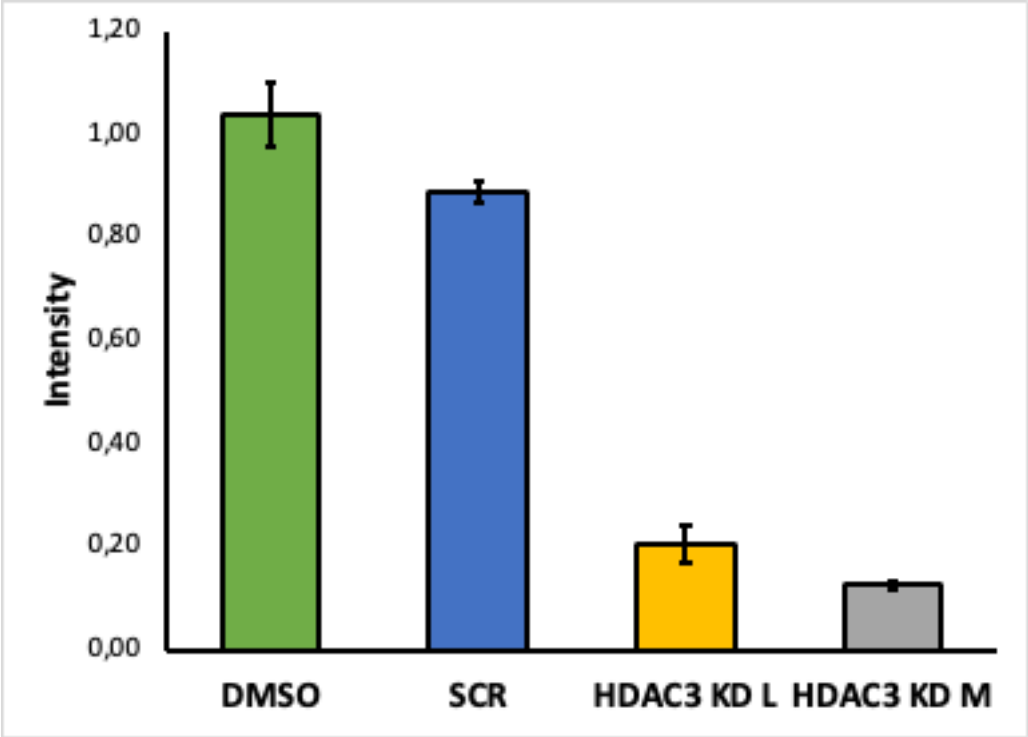

Figure 18: Quantification of HDAC protein levels by Western blot analysis following HDAC3 knockdown

HDAC3 protein levels were strongly reduced in both HDAC3 KD L and HDAC3 KD M conditions compared to the CTRL and SCR samples. Data are represented as mean intensity values ± standard deviation for each experimental group.

3.1.3.2 Impact of siRNA-mediated knockdown on formation of lipids

Following optimization and validation of siRNA-mediated knockdown of HDAC1, HDAC2, and HDAC3 by Western blotting, ORO staining was performed as an additional assay to verify whether the knock-down of individual class I HDAC isoforms was sufficient to increase lipid accumulation.

ORO staining was carried out on two 12-well plates for 48h, with four wells assigned to each condition.

Treatment-dependent variation in lipid accumulation faintly observed across conditions (**Figure 19**), with the lipid droplets appearing as red dots (ORO staining), and nuclei being stained blueish (Hematoxylin). Quantitative image analysis (**Figure 20**) showed that mean lipid droplet area per nucleus was only a minor increased in all HDAC KD conditions compared to the untreated control (DMSO).

A scrambled siRNA control was included as an additional negative control and did not show a significant change relative to untreated cells.
Knockdown of HDAC2 and combined knockdown of HDAC1 and HDAC2 resulted in statistically significant increases in lipid content compared to the scrambled control but they are very small, as quantified by ORO staining. Knockdown of HDAC1 alone or HDAC3 alone did not produce significant changes in lipid accumulation relative to the scrambled control.

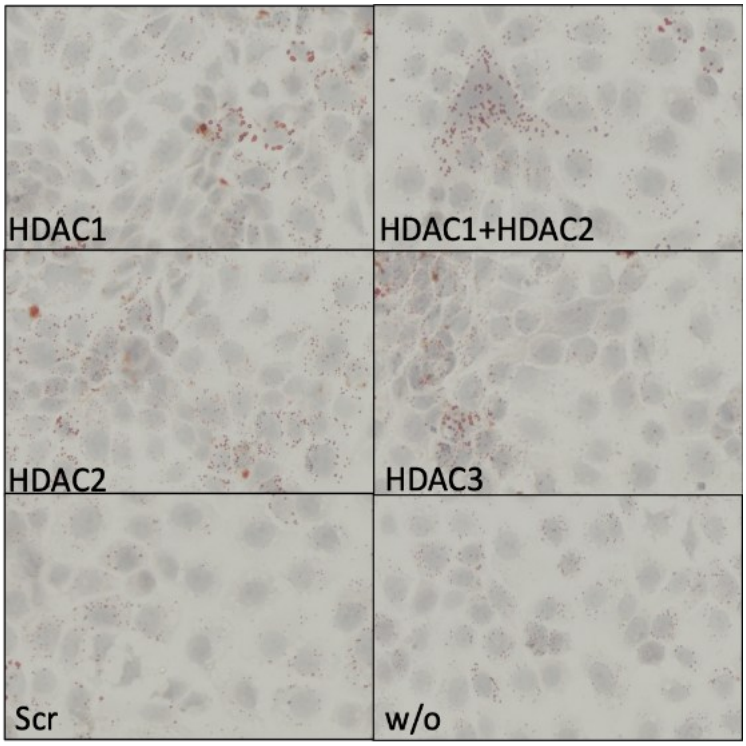

Figure 19: ORO-stained SZ95 cells under multiple class I HDAC KD treatment conditions:
Representative microscope images of ORO-stained SZ95 cells under the following conditions: w/o (DMSO-negative control), scr, HDAC1 KD, HDAC2 KD, HDAC1+HDAC2 KD, and HDAC3 KD. Images show lipid droplets (red) in the cytoplasm and cell nuclei counterstained with hematoxylin (blueish).

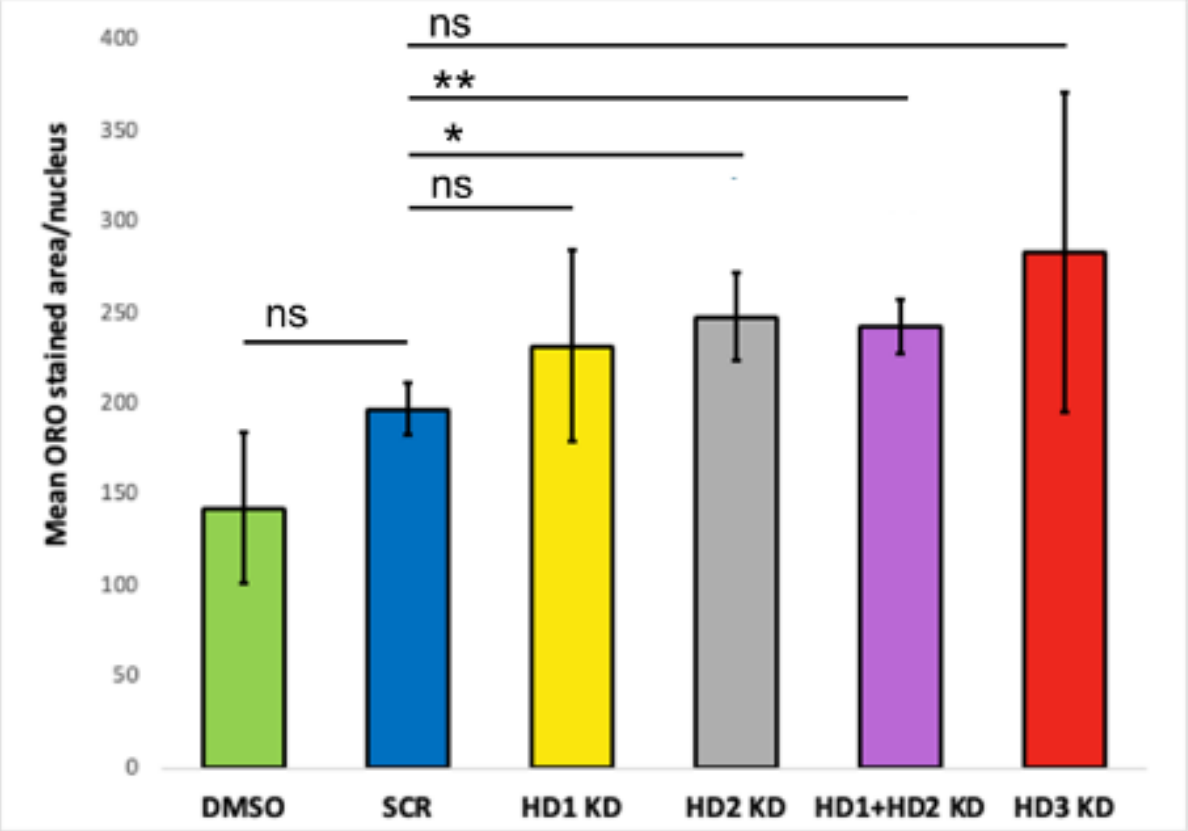

Figure 20: Quantification of the ORO staining in SZ95 cells under multiple class I HDAC KD treatment conditions

*Mean ORO-stained area per nucleus is shown for cells treated with DMSO, Scr, HDAC1 KD, HDAC2 KD, HDAC1+HDAC2 KD, and HDAC3 KD. Data represent means ± SD from three independent replicates. Statistical significance: ns≥0.05; *p < 0.05; **p < 0.01 (one-way ANOVA).*

3.1.4 Effect of PPARγ inhibition on sebocyte lipid accumulation- pilot experiment

Previous experiments demonstrated that lipogenic stimulation with insulin and the LXR-agonist TO901317, combined with class I HDAC inhibition by MS-275, promoted robust lipid accumulation in SZ95 sebocytes. To assess whether the master transcription factor involved in lipid metabolism PPARγ modulates this lipogenic response, cells were treated with increasing concentrations of the PPARγ inhibitor T0070907 (0, 1, and 2 µM) under defined treatment conditions and analyzed by ORO staining and quantitative image analysis. Treatment with 10 µM T0070907 was initially included but was excluded from further analysis due to significant cell death observed from Day 3 of treatment onwards, preventing reliable quantification under this condition.

SZ95 cells were cultured under DMSO control, MS-275, or combined insulin+TO901317+MS-275 conditions in the presence of 0, 1, or 2 µM T0070907 for 72 hours, followed by ORO staining to visualize neutral lipid accumulation and hematoxylin counterstaining to label nuclei. Lipid accumulation was quantified as mean ORO-positive area per nucleus.

Representative images (**Figure 21**) and quantification (**Figure 22**) revealed treatment-dependent variation in lipid droplet formation across all conditions. Consistent with prior

experiments, MS-275 treatment increased lipid accumulation relative to DMSO, and this effect was further enhanced by combined insulin+TO901317 stimulation.
Within the MS-275 and MS-275+insulin+TO901317 conditions, PPARγ inhibition at 1 µM T0070907 produced a statistically significant further increase in lipid accumulation relative to the uninhibited condition, with the highest mean ORO-stained area per nucleus observed in the insulin+TO901317+MS-275+1 µM T0070907 group. At 2 µM T0070907, this effect was no longer statistically significant compared to the 0 µM condition within the same treatment group, suggesting an attenuation at higher inhibitor concentrations. In the DMSO-only context, the pattern was inverted: only 2 µM T0070907 reached significance, likely reflecting a distinct baseline sensitivity rather than a consistent dose-response

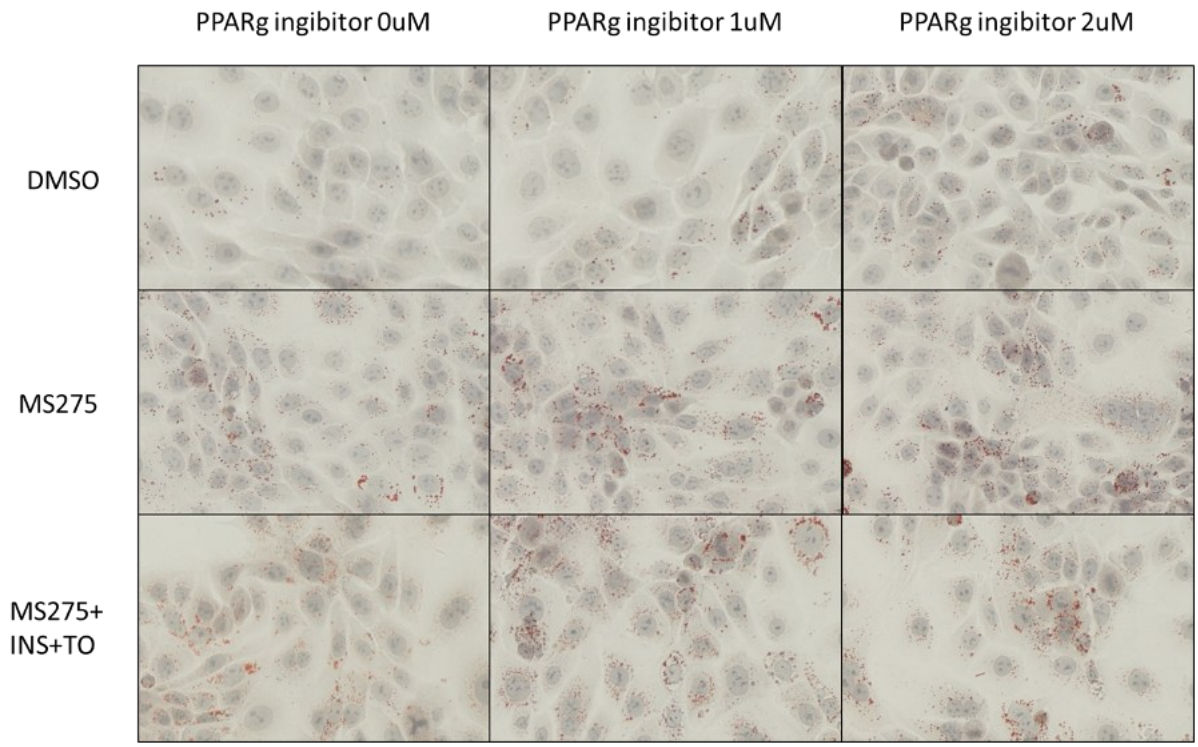

Figure 21: ORO-stained SZ95 cells under multiple treatment conditions:

Representative microscope images of ORO-stained SZ95 cells under the following conditions: DMSO 1:1000 (negative control), DMSO 1:1000+1 µM PPARγ inhibitor, DMSO 1:1000+2 µM PPARγ inhibitor, MS-275, MS-275+1 µM PPARγ inhibitor, MS-275+2 µM PPARγ inhibitor, MS-275+insulin+TO901317, MS-275+insulin+TO901317+1 µM PPARγ inhibitor, MS-275+insulin+TO901317+2 µM PPARγ inhibitor. Images show lipid droplets (red) in the cytoplasm and cell nuclei counterstained with hematoxylin (blueish).

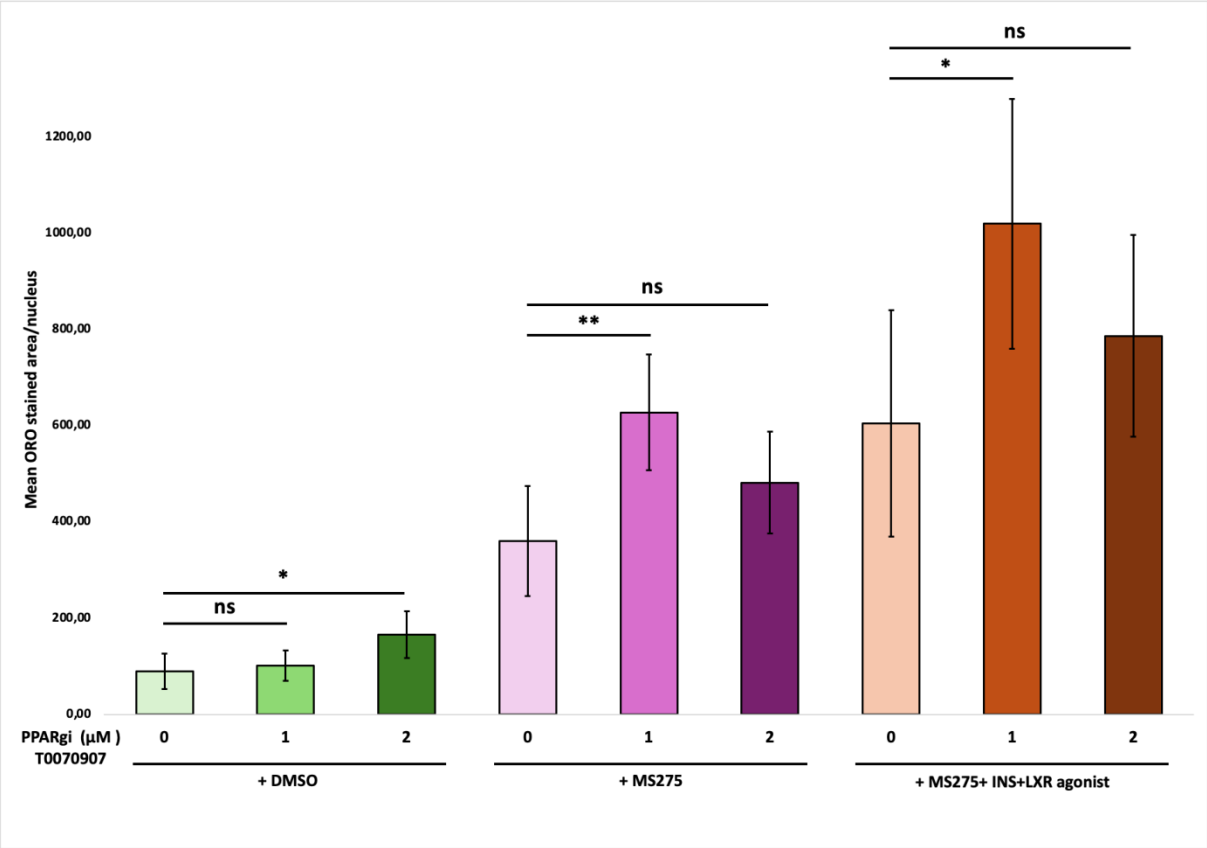

Figure 22: Quantification of the ORO staining in SZ95 cells under multiple treatment

*Mean ORO-stained area per nucleus is shown for cells treated with DMSO 1:1000 (negative control), DMSO 1:1000+1 µM PPARγ inhibitor, DMSO 1:1000+2 µM PPARγ inhibitor, MS-275, MS-275+1 µM PPARγ inhibitor, MS-275+2 µM PPARγ inhibitor, MS-275+insulin+TO901317, MS-275+insulin+TO901317+1 µM PPARγ inhibitor, MS-275+insulin+TO901317+2 µM PPARγ inhibitor. Data represent means ± SD from one well. Statistical significance: ns≥0.05; *p < 0.05; **p < 0.01 (one-way ANOVA).*

3.1.5 Validation of antibodies

Previous experiments in SZ95 sebocytes showed that lipid accumulation can be stimulated by insulin+TO901317 treatment and further enhanced by MS-275 or by siRNA-mediated knockdown of HDAC1 and HDAC. To enable reliable analysis of lipid metabolism pathways at the protein level in these experimental settings, the suitability of commercially available antibodies against lipid-associated enzymes and regulators was evaluated in SZ95 cells.

Western blotting was performed using SZ95 lysates from cells treated with insulin, TO901317, MS-275, and siRNA-mediated knockdown of HDAC1 and HDAC2. In total, nine antibodies targeting lipid metabolism related proteins were tested. Antibody performance was assessed based on the presence of specific bands at the expected molecular weight and the extent of nonspecific background.

Several antibodies produced clear, specific bands at the expected sizes, including PEPCK/PCK1/PCK2 (~70 kDa; sc-271029), SCD (~40 kDa; sc-515844), ADRP/Perilipin-2 (~48 kDa; 15294-1-AP), FADS3 (~51 kDa; 15205-1-AP), and ELOVL6 (~31 kDa; 21160-1-AP). In contrast, antibodies against SREBP-1 (~68 kDa, ~120 kDa; sc-13551), monoglyceride lipase (~33 kDa; sc-398942), UGT8 (~61 kDa; 17982-1-AP), and FA2H (~43 kDa; 15452-1-AP) did not yield specific bands and/or showed predominantly nonspecific background signal (**Figure 23**, **Figure 24**).

Although five antibodies were technically suitable based on band specificity, only SCD showed a detectable treatment-dependent regulation under the conditions tested, getting up-regulated as a result of insulin+TO901317 treatment. Overall, this antibody validation established a set of reliable tools for Western blot analysis of lipid metabolism in SZ95 sebocytes and identified antibodies that were not suitable in this system, providing a practical basis for future mechanistic experiments.

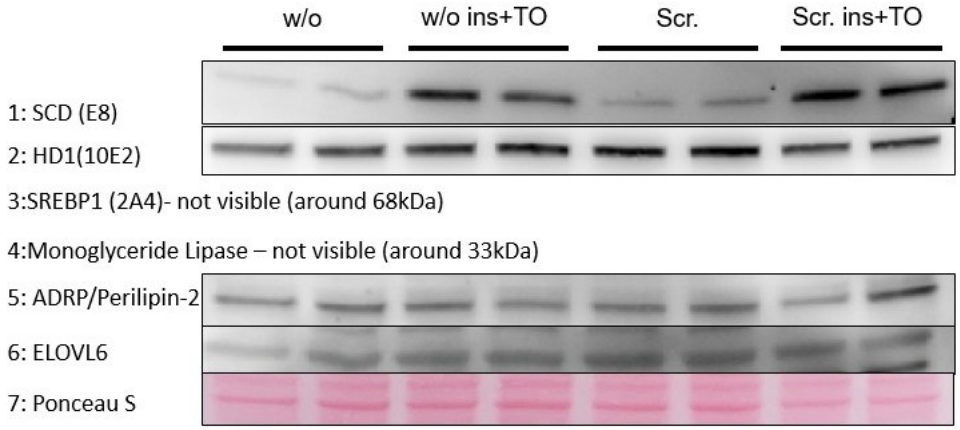

Figure 23: Testing of the new antibodies in SZ95 cell lysates:
Western blot analysis lysates from SZ95 cells treated with w/o (control), insulin+TO(TO901317), scr and scr+insulin+TO. Ponceau S was used as loading control.

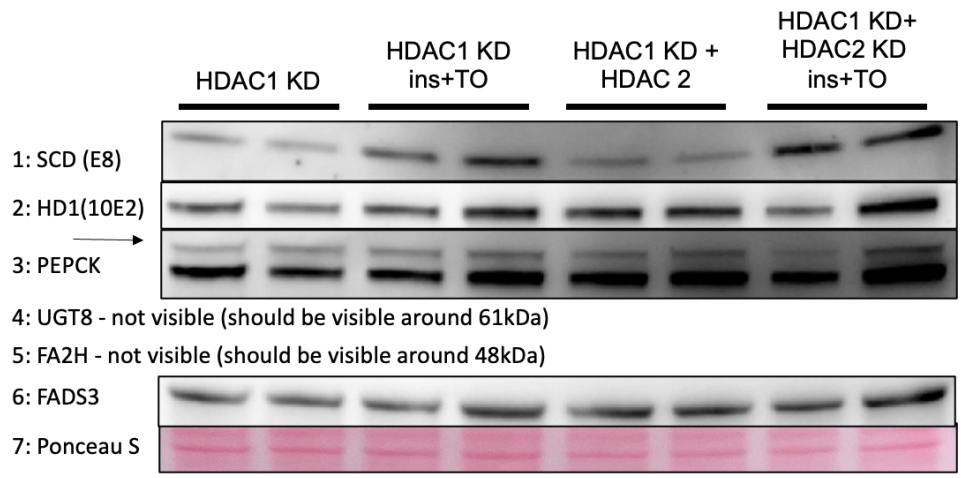

Figure 24: Testing of the new antibodies in SZ95 cell lysates:
Western blot analysis lysates from SZ95 cells treated with siRNAs against HDAC1 (HD1KD), HD1KD+insulin+TO(TO901317), HD1&HD2KD and HD1&HDKD2+insulin+TO. Ponceau S was used as loading control.

3.1.6 Analysis of chromatin wide changes of histone modifications using CUT&RUN (Cleavage Under Targets & Release Using Nuclease)

Previous experiments indicated that class I HDAC inhibition promotes a lipogenic phenotype in SZ95 sebocytes and suggested that chromatin-based mechanisms may contribute to transcriptional activation of target genes. To determine whether these treatments alter promoter-associated chromatin states, CUT&RUN method was established in the lab using the SZ95 sebocytes cell line.

Cells were analyzed under DMSO control condition and after conditions that trigger formation of intracellular lipid droplets (insulin+TO901317+MS-275), using two biological replicates. CUT&RUN profiling was performed using an antibody against histone H3K4me3, a marker of active promoters, alongside IgG controls to assess background signal. However, one of the two DMSO-treated samples did not pass the quality control after NGS and therefore was excluded from further analysis.

At the *SREBF1* locus, CUT&RUN profiling revealed distinct and reproducible changes in H3K4me3 occupancy upon combination treatment. A promoter-proximal peak was present under both DMSO and treated conditions present but enhanced by conditions favoring lipid droplet formation in the right part of the track, consistent with a constitutively active promoter for *SREBP-1a*. In addition, a second downstream of the first promoter peak was specifically induced upon treatment conditions and was not detectable under control conditions. This treatment-specific peak is consistent with activation of the alternative *SREBP-1c* promoter, which is known to be regulated by LXR signaling. This indicates that, when lipid droplet formation in SZ95 cells is induced by insulin, LXR-Agonist and MS-275 specifically the *SREBF1c* promotor specifically gains active histone marks.

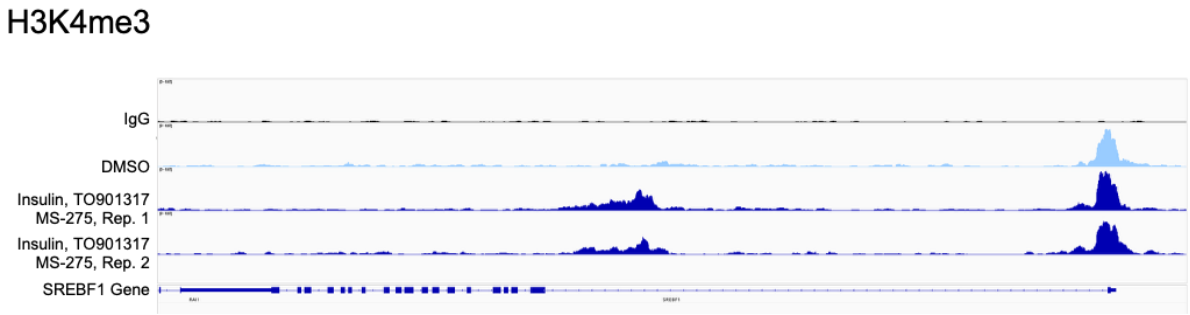

Figure 25: CUT&RUN analysis of H3K4me3 at the SREBF1 promoter in HDAC1 H141A clones under insulin, TO901317, and MS-275 treatment:

IGV (Integrative Genomics Viewer) screenshot showing a visual representation of CUT&RUN profiling of H3K4me3 at the SREBF1 locus in heterozygous HDAC1 H141A knock-in SZ95 sebocytes treated with DMSO (light blue) or a combination of insulin, TO901317, and MS-275 (dark blue, two biological replicates). IgG served as a negative control (black). Two spatially distinct H3K4me3-enriched regions are visible: a sharp peak at the canonical SREBF1 promoter (right), present under both conditions but enhanced by combo treatment, and a broader peak at a second upstream regulatory region (center), detected exclusively under the treatment condition and consistent with the known LXR-responsive SREBP-1c alternative promoter. Both treated replicates show concordant signal, indicating reproducibility. IgG signal remains flat across the locus, confirming specificity of enrichment.

At the genomic locus of fatty acid synthase (*FASN)*, a prominent H3K4me3 peak cluster was detected at the promoter/TSS region under both DMSO and combination treatment conditions, indicating that the FASN promoter is basally active. Upon insulin+TO901317+MS-275 treatment, H3K4me3 signal intensity was increased compared to DMSO, with a broader and higher peak profile. This enhancement was reproducible across both replicates. IgG

controls showed minimal signal, confirming assay specificity. The basal H3K4me3 signal in DMSO indicates a constitutively active promoter that is further enhanced by the combination treatment, consistent with convergent transcriptional activation of *FASN* through LXR and SREBP-1 dependent pathways.

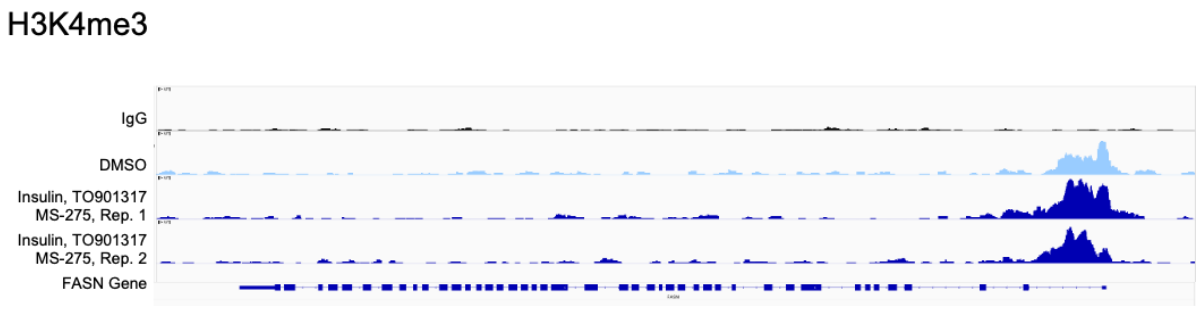

Figure 26: CUT&RUN analysis of H3K4me3 at the FASN promoter in HDAC1 H141A clones under insulin, TO901317, and MS-275 treatment:

IGV (Integrative Genomics Viewer) screenshot showing a visual representation of CUT&RUN profiling of H3K4me3 at the FASN locus in heterozygous HDAC1 H141A knock-in SZ95 sebocytes treated with DMSO (light blue) or a combination of insulin, TO901317, and MS-275 (dark blue, two biological replicates). IgG served as a negative control (black). A broad, multi-summit H3K4me3 peak is detected at the FASN promoter region under both conditions, with increased signal under the treatment condition. Both treated replicates show concordant signal, indicating reproducibility. IgG signal remains flat, confirming specificity.

At the locus of the gene for stearoyl-CoA desaturase (*SCD*), a prominent H3K4me3 peak was detected at the 5' promoter/TSS region under both DMSO and combination treatment conditions, while the gene body remained largely devoid of signal. The DMSO condition already exhibited a strong H3K4me3 signal, indicating that the SCD promoter is highly active under basal conditions in the transfected SZ95 sebocytes. Upon combination treatment, H3K4me3 signal intensity was further increased. A slight extension of signal into the proximal gene body was observed, likely reflecting high transcriptional activity rather than a distinct regulatory feature. Replicates showed concordant patterns, and IgG controls exhibited minimal signal, confirming assay specificity.

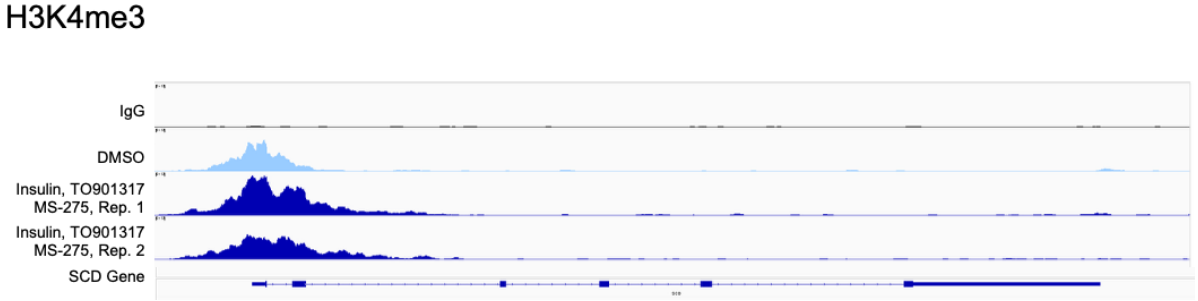

Figure 27: CUT&RUN analysis of H3K4me3 at the SCD promoter in HDAC1 H141A clones under insulin, TO901317, and MS-275 treatment:

IGV (Integrative Genomics Viewer) screenshot showing a visual representation of CUT&RUN profiling of H3K4me3 at the SCD locus in heterozygous HDAC1 H141A knock-in SZ95 sebocytes treated with DMSO (light blue) or a combination of insulin, TO901317, and MS-275 (dark blue, two biological replicates). IgG served as a negative control (black). A broad, multi-summit H3K4me3 peak is detected at the SCD promoter under both conditions, with the DMSO condition showing notably high basal enrichment consistent with constitutively active transcription in sebocytes. Both treated replicates show concordant signal, indicating reproducibility. IgG signal remains flat, confirming enrichment specificity.

Under DMSO conditions, H3K4me3 signal at the ATP-binding cassette subfamily D member 1 (*ABCA1)* locus was almost absent, indicating minimal basal promoter activity. In contrast, combination treatment induced a sharp, localized H3K4me3 peak at the promoter region, which was reproducible across both replicates. The peak displayed a narrow, well-defined morphology consistent with canonical promoter-associated H3K4me3 enrichment. IgG controls remained flat, confirming signal specificity. This pattern indicated a transition from an more inactive to a more active chromatin state at the *ABCA1* promoter upon combination treatment, representing de novo promoter activation rather than enhancement of an already active locus. Mechanistically, this is consistent with *ABCA1* being a direct target of LXR signaling, where TO901317-mediated activation of LXR drives transcriptional induction. Concurrent HDAC inhibition likely facilitates chromatin accessibility, supporting efficient promoter activation.

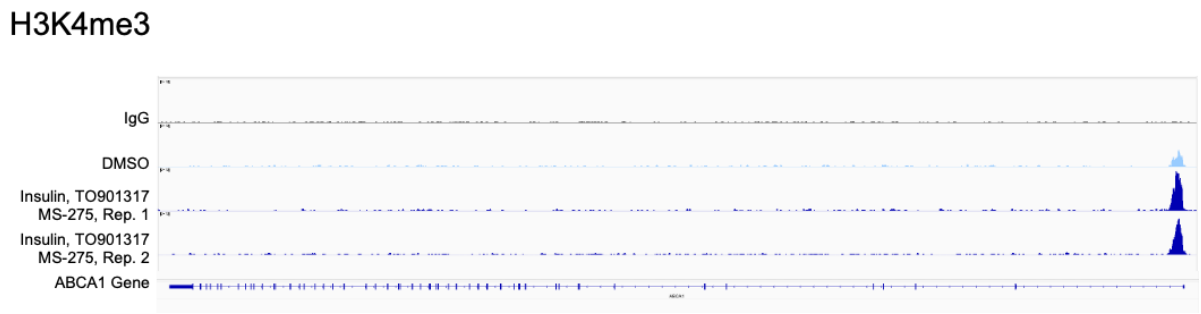

Figure 28: CUT&RUN analysis of H3K4me3 at the ABCA1 promoter in HDAC1 H141A clones under insulin, TO901317, and MS-275 treatment:

IGV (Integrative Genomics Viewer) screenshot showing a visual representation of CUT&RUN profiling of H3K4me3 at the ABCA1 locus in heterozygous HDAC1 H141A knock-in SZ95 sebocytes treated with DMSO (light blue) or a combination of insulin, TO901317, and MS-275 (dark blue, two biological replicates). IgG served as a negative control (black). H3K4me3 signal is near-absent across the ABCA1 locus under DMSO conditions, while combo treatment induces a sharp, reproducible peak at the ABCA1 promoter region. Both treated replicates show concordant signal, indicating reproducibility. IgG signal remains flat throughout, confirming enrichment specificity.

To confirm that the observed increases in H3K4me3 occupancy at lipogenic gene promoters reflected locus-specific transcriptional activation rather than a global chromatin effect of the treatment used to induce lipid droplet formation, three additional loci were examined: *ZNF713*, *DLX2*, and *EOLA2*. These genes showed reduced of H3K4me3 enrichment relative to DMSO, indicating that the treatment-induced changes in H3K4me3 changes are gene-specific and not due to non-specific chromatin remodeling.

H3K4me3 signal at the *DLX2* locus displays a broad basal signal under DMSO that is not enhanced by combo treatment, serving as a locus-specific control demonstrating that H3K4me3 increases at lipogenic gene promoters reflect targeted transcriptional regulation rather than non-specific.

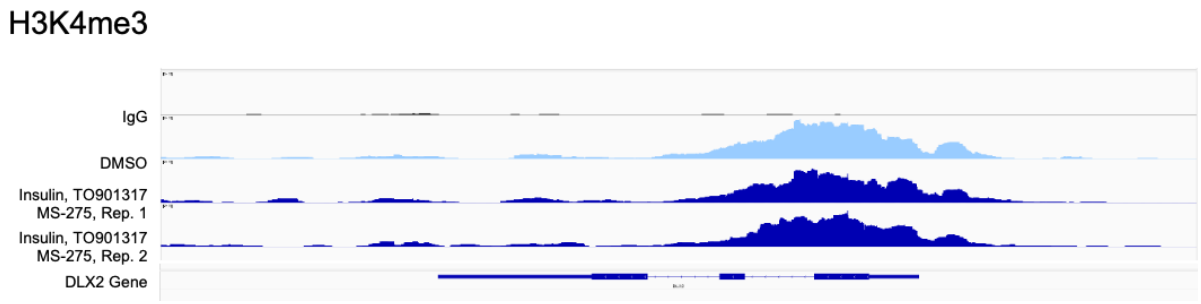

Figure 29: CUT&RUN analysis of H3K4me3 at the DLX2 promoter in HDAC1 H141A clones under combination treatment:

IGV (Integrative Genomics Viewer) screenshot showing a visual representation of CUT&RUN profiling of H3K4me3 at the DLX2 locus in heterozygous HDAC1 H141A knock-in SZ95 sebocytes treated with DMSO (light blue) or a combination of insulin, TO901317, and MS-275 (dark blue, two biological replicates). IgG served as a negative control (black). DLX2 displays a broad basal H3K4me3 signal under DMSO that is not enhanced by combo treatment. Both treated replicates show concordant signal, indicating reproducibility. IgG signal remains flat, confirming enrichment specificity

EOLA2 displays reduced H3K4me3 occupancy under treatment conditions relative to DMSO, serving as a locus-specific control to confirm the specificity of treatment driven H3K4me3 enrichment at lipogenic target gene promoters.

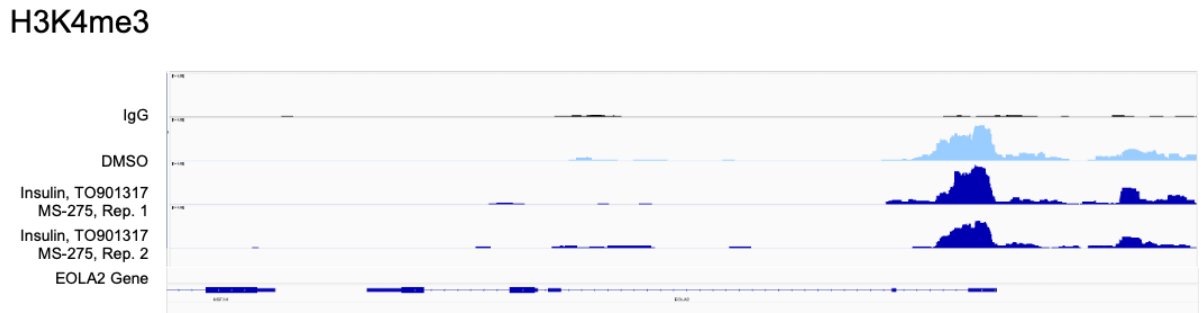

Figure 30: CUT&RUN analysis of H3K4me3 at the EOLA2 promoter in HDAC1 H141A clones under combination treatment:

IGV (Integrative Genomics Viewer) screenshot showing a visual representation of CUT&RUN profiling of H3K4me3 at the EOLA2 locus in heterozygous HDAC1 H141A knock-in SZ95 sebocytes treated with DMSO (light blue) or a combination of insulin, TO901317, and MS-275 (dark blue, two biological replicates). IgG served as a negative control (black). The neighboring gene HSFX4 is also present within this genomic window. EOLA2 displays reduced or comparable H3K4me3 occupancy under combo relative to DMSO. Both treated replicates show concordant signal, indicating reproducibility. IgG signal remains flat, confirming enrichment specificity.

H3K4me3 occupancy at the *ZNF713* locus was reduced under combo treatment compared to DMSO, indicating that the observed increases at lipogenic gene promoters were not attributable to a global, treatment-induced chromatin remodeling effect.

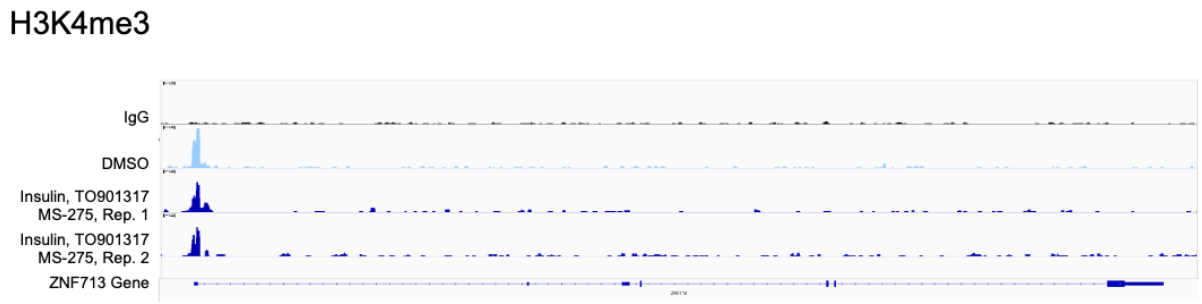

Figure 31: CUT&RUN analysis of H3K4me3 at the ZNF713 promoter in HDAC1 H141A clones under combination treatment:

IGV (Integrative Genomics Viewer) screenshot showing a visual representation of CUT&RUN profiling of H3K4me3 at the ZNF713 locus in heterozygous HDAC1 H141A knock-in SZ95 sebocytes treated with DMSO (light blue) or a combination of insulin, TO901317, and MS-275 (dark blue, two biological replicates). IgG served as a negative control (black). ZNF713 displays reduced H3K4me3 occupancy under combo treatment relative to DMSO. Both treated replicates show concordant signal, indicating reproducibility. IgG signal remains flat, confirming enrichment specificity.

3.2 Generation of CRISPR/Cas-mediated transgenic SZ95 cell lines expressing catalytic inactive HDAC1 (HDAC1 H141A) and wildtype HDAC1

3.2.1 Generation and validation of cell lines

Previous experiments indicated that class I HDAC inhibition and isoform-specific knockdown affected lipid accumulation in SZ95 sebocytes but also revealed mutual regulation between HDAC1 and HDAC2 (Figure 13, 15). To determine whether the enhanced lipogenesis depends on HDAC1 catalytic activity, rather than loss of HDAC1 protein, stable SZ95 cell lines were generated expressing either FLAG-tagged wild-type HDAC1 (HDAC1 WT) or a catalytically inactive H141A variant. This approach aimed to separate enzymatic activity from the structural and scaffolding functions without removing the protein entirely, because the catalytically inactive HDAC1 KI clones are reducing confounding effects from HDAC2 compensation and preserving HDAC1's scaffolding role, preventing co-repressor complex destabilization, that can occur upon knockdown.

Cell lines were generated by integration of HDAC1 WT and HDAC1 H141A constructs carrying a C-terminal FLAG tag into the AAVS1 safe-harbor locus of SZ95 cells to achieve long-term expression (Figure 8). Two experimental groups were produced: a FLAG-tagged wild-type allele (HDAC1 WT) and a FLAG-tagged catalytically inactive (HDAC1 H141A). The WT allele served as an essential control because it represents a functional HDAC1 protein expressed from the same construct backbone and at comparable levels, providing a more appropriate reference than un-transfected cells when evaluating effects attributable specifically to loss of catalytic activity.

After expansion, clones were screened for transgene expression by immunostaining with the M2-FLAG antibody to ensure that the detected signal originated specifically from FLAG-tagged HDAC1-expressing cells (**Figure 32**). Based on FLAG immunoreactivity, both FLAG-positive clones (expressing the transgene) and FLAG-negative clones (non-expressing) were selected as internal controls within each construct background (HDAC1 WT and HDAC1 H141A). This strategy enabled clear distinction between tagged and untagged populations and established relatable reference points for downstream analyses. In total, 20 individual clones and subclones were obtained and are summarized in **Table 4**.

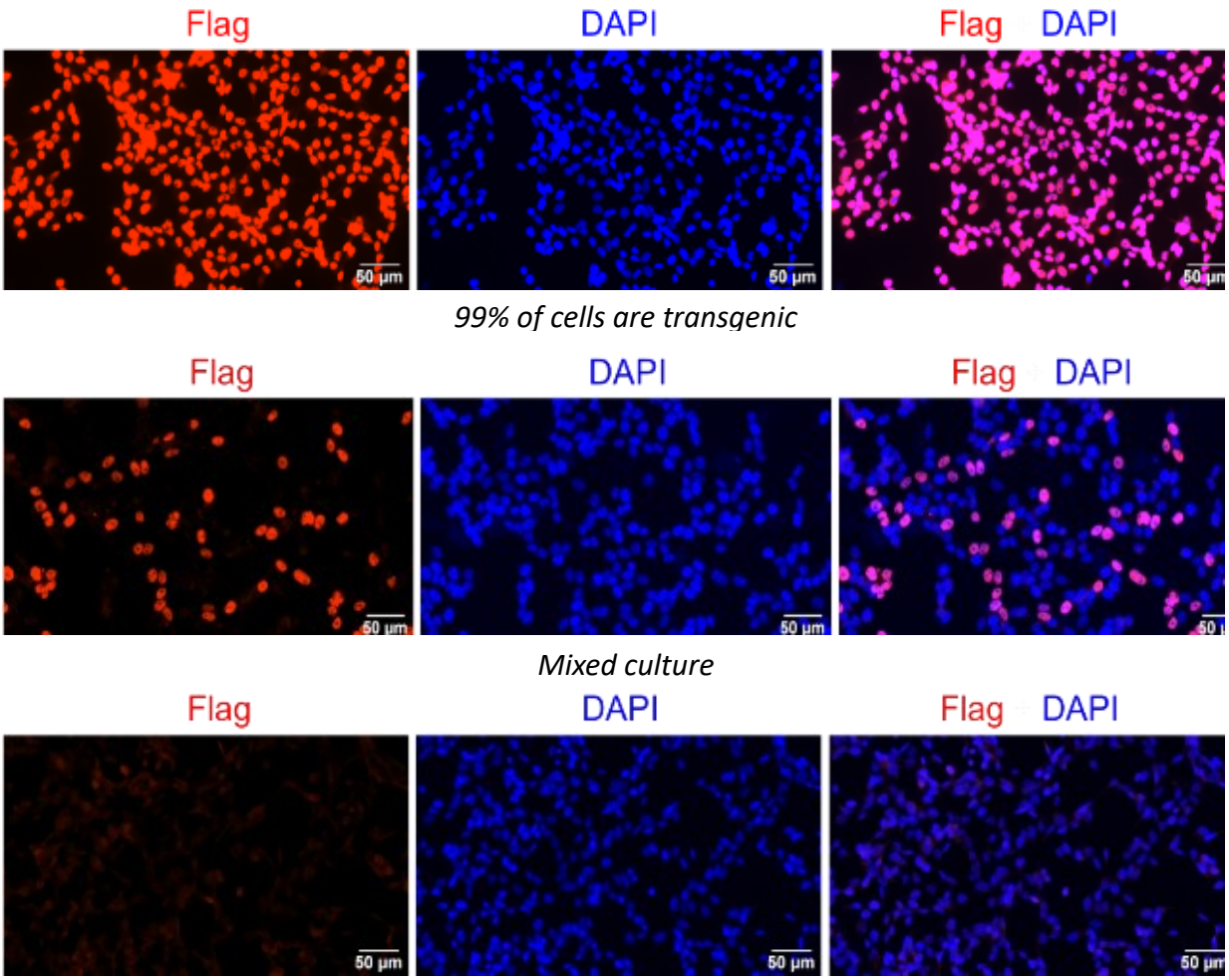

Figure 32: The positive and negative FLAG stains of the SZ95 clones:
Representative immunofluorescence images of SZ95 clones stained for FLAG to distinguish tagged from untagged cell populations. FLAG signal is shown in red, nuclei are counterstained with DAPI (blue), and merged images (FLAG + DAPI) are shown on the right. FLAG-positive clones display strong nuclear-associated FLAG signal in most cells, whereas the negative population shows no FLAG fluorescence, and the mixed culture display nuclear-associated FLAG signal in just some cells. Scale bar: 50 µm

3.2.2 Evaluation of SZ95 clones by Western blotting

Stable SZ95 clones expressing FLAG-tagged HDAC1 WT or the catalytically inactive HDAC1 H141A variant were generated to separate HDAC1 enzymatic activity from its structural functions and to assess potential compensatory responses that can disrupt the knockdown-based approaches. To verify transgene expression and to compare protein levels across clones, Western blotting was performed on selected FLAG-positive and FLAG-negative clones (**Figure 33**, **Figure 35**).

In the HDAC1 Western blot, an endogenous HDAC1 band was detected in all samples, including negative controls. In clones carrying the HDAC1 WT or H141A KI alleles, an additional HDAC1 band migrated at a slightly higher apparent molecular weight, consistent with the presence of the FLAG tag. This was corroborated by the M2-FLAG blot, which specifically detected the tagged KI proteins. The WT clones showed stronger expression of the KI-derived HDAC1 protein compared to the HDAC1 H141A clones, in line with the expected expression pattern.

HDAC2 protein levels were similar across HDAC1 WT and HDAC1 H141A clones, consistent with the interpretation that endogenous regulatory mechanisms may buffer loss of HDAC1 catalytic function, potentially contributing to compensation in the mutant background. Protein loading was assessed using GAPDH as a housekeeping control and Ponceau S staining, supporting comparability of the analyzed lysates.

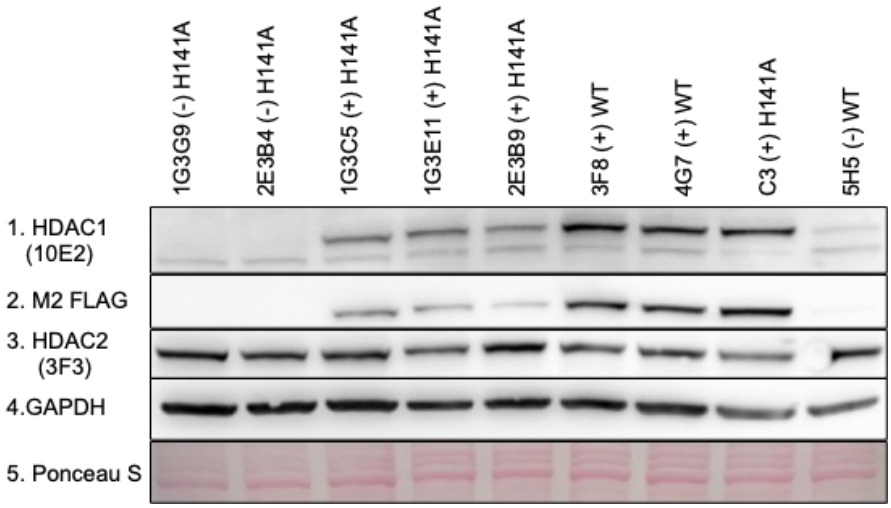

Figure 33: Evaluation of SZ95 clones and subclones by Western blotting

Cell lysates from FLAG-positive and FLAG-negative populations expressing HDAC1 wild type (WT) or the catalytically inactive HDAC1 H141A mutant (MUT) were analyzed. GAPDH and Ponceau S staining was used as loading controls.

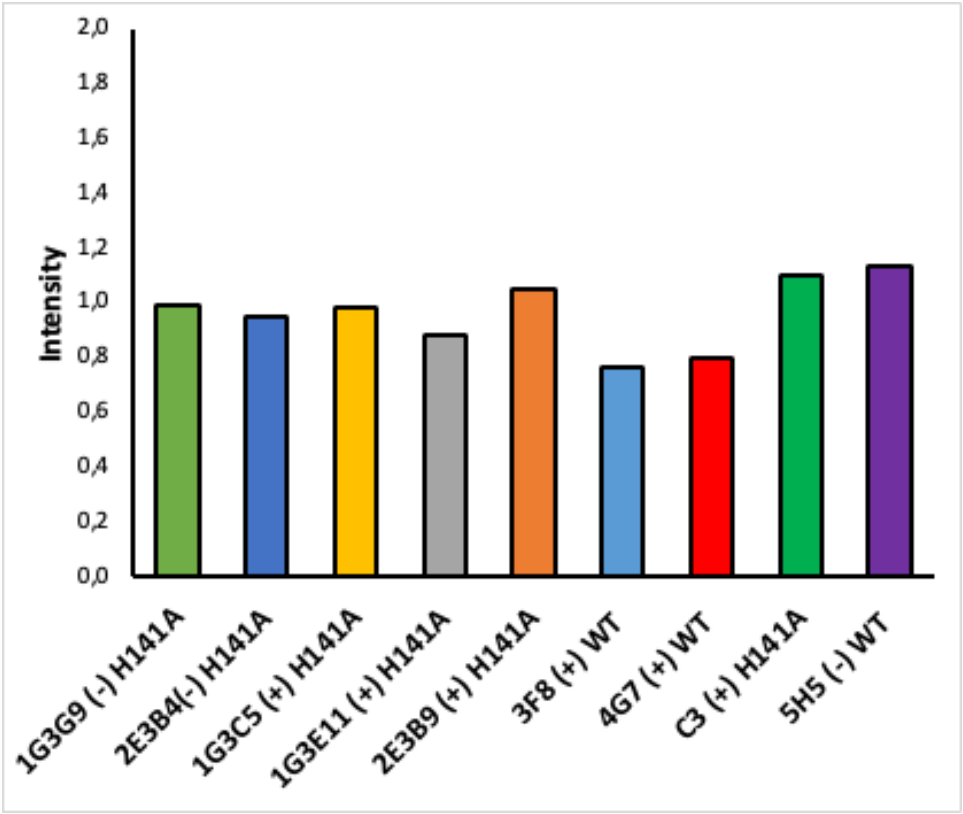

Figure 34: Quantification of HDAC2 protein levels by Western blot analysis on the generated clones

HDAC2 protein levels are similar among all the clones negative (-) or positive (+) onec. Data are represented as the intensity values for each clone.

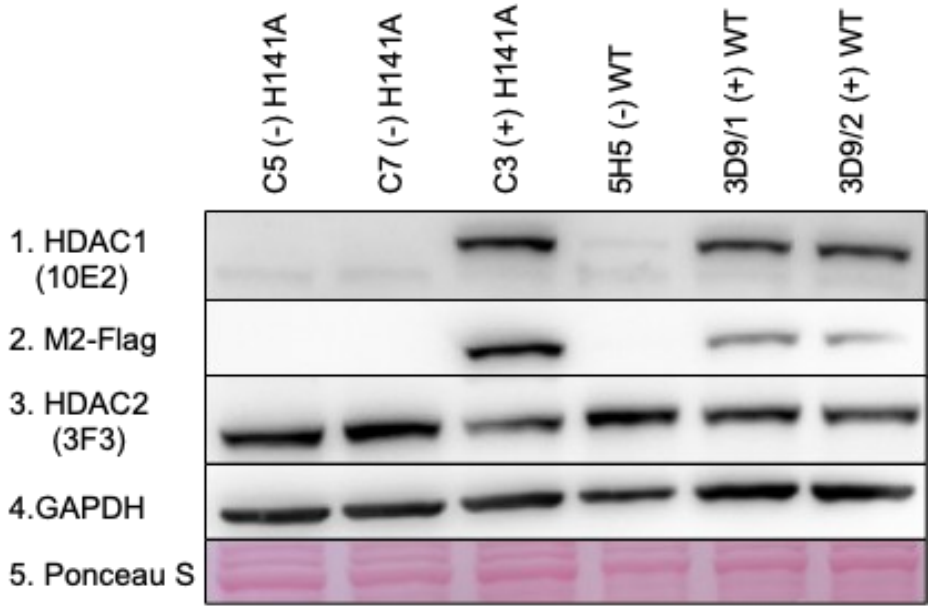

Figure 35: Evaluation of SZ95 clones and subclones by Western blotting:

Cell lysates from FLAG-positive and FLAG-negative populations expressing HDAC1 wild type (WT) or the catalytically inactive HDAC1 H141A mutant (MUT) were analyzed. GAPDH and Ponceau S staining was used as loading controls.

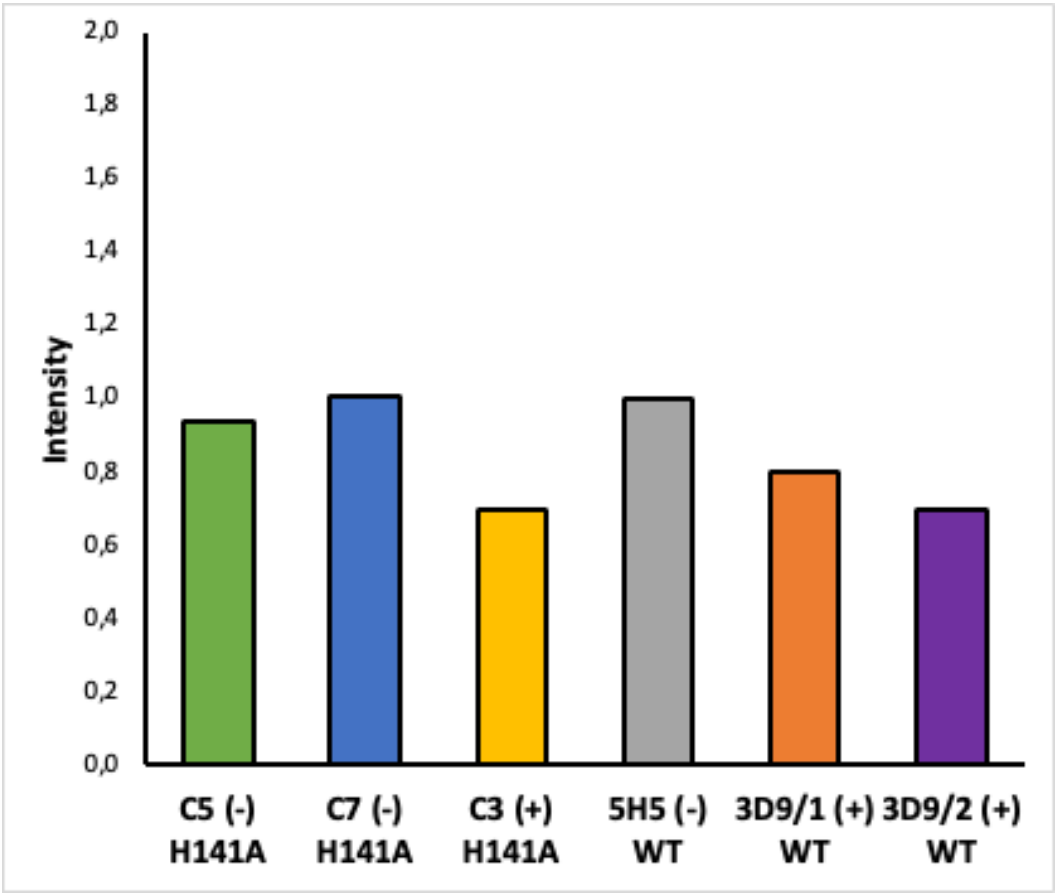

Figure 36: Quantification of HDAC2 protein levels by Western blot analysis on the generated clones

HDAC2 protein levels are similar among all the clones negative (-) or positive (+) onec. Data are represented as the intensity values for each clone.

3.2.3 Assessment of the activity and co-repressor complex formation of HDAC1 variants

To determine whether the generated HDAC1 knock-in clones differed in HDAC1 catalytic activity as intended, a deacetylase activity assay was performed together with lab rotation student Mia Vican. This experiment was conducted to functionally validate that FLAG-tagged HDAC1 WT clones retained enzymatic activity, whereas FLAG-tagged HDAC1 H141A clones lacked catalytic activity despite expressing the protein. This validation step was essential because these transgenic lines were generated to investigate the HDAC1 catalytic function, excluding the structural and scaffolding functions and reducing confounding effects seen in knockdown settings (compensation by HDAC2 and potential destabilization of co-repressor complexes).

Deacetylase activity was measured in (**Figure 37**) whole-cell lysates ("input") and (**Figure 38**) FLAG immunoprecipitation ("IP") obtained by FLAG pull-down. Activity was quantified by measuring the release of acetate from radioactive ^{3}H-acetylated histones over a 3h reaction period. Readouts were reported as counts per minute (cpm) and normalized to a blank sample containing only assay buffer (Hunt buffer) to control for background signal.

Input measurements (**Figure 37**) showed comparable activity across samples. This was expected because whole-cell lysates reflect the combined catalytic activity of all endogenous HDACs present in the cells rather than specifically the FLAG-tagged HDAC1 variant. Importantly, the similar input activities indicated that comparable amounts of starting material were used across conditions, supporting that differences observed in the IP fraction were not driven by unequal protein input.

In the FLAG-IP measurements (**Figure 38**), negative control samples showed only low activity (background), consistent with the absence of FLAG-tagged HDAC1. FLAG-IP samples from HDAC1 WT clones displayed the highest activity, as expected for catalytically active, wild type, HDAC1 and serving as positive controls. In contrast, FLAG-IP samples from HDAC1 H141A clones exhibited reduced activity, consistent with successful introduction of a catalytically inactive HDAC1 allele. Overall, the assay confirmed that the knock-in strategy produced clones with the expected separation of HDAC1 catalytic activity between HDAC1 WT and HDAC1 H141A mutant variants, enabling downstream experiments to attribute phenotypes specifically to loss of HDAC1 enzymatic activity rather than loss of HDAC1 protein or co-repressor complex integrity.

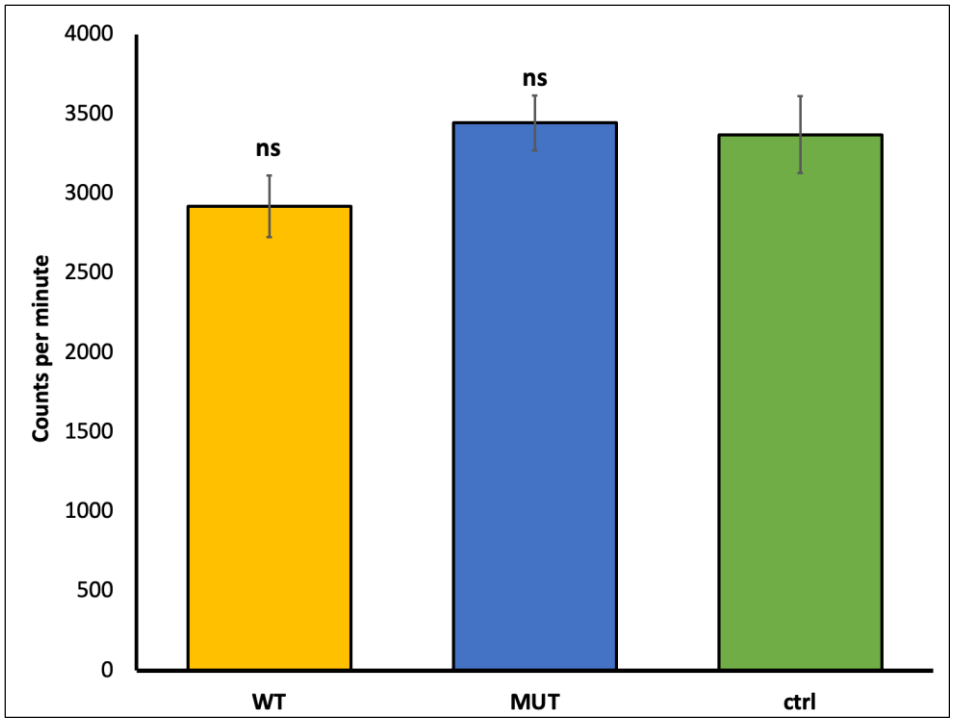

Figure 37: HDAC activity assay in input (whole cell lysates) samples:

*Enzymatic activity measured in input lysates prior to downstream processing. Bars show mean activity (counts per minute, CPM) for each sample (C8-ctrl, G9-ctrl, C5-MUT, E11-MUT, 3F8-WT, 4G7-WT); error bars indicate variability between replicates (SD). Overall, input activities were broadly comparable across samples. Statistical significance was indicated as follows: ns, p > 0.05; *, p < 0.05; **, p < 0.01; ***, p < 0.001; ****, p < 0.0001 vs. ctrl (one-way ANOVA).*

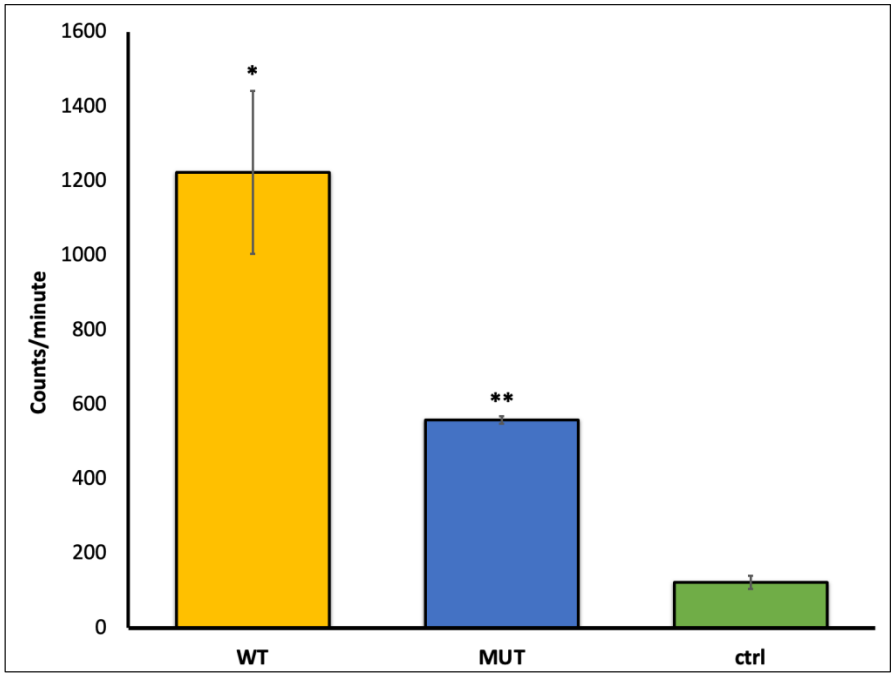

Figure 38: HDAC activity assay in FLAG-immunoprecipitated (FLAG-IP) samples:

*Enzymatic activity measured in FLAG-immunoprecipitated samples (FLAG-IP). Bars show mean activity (cpm) for each sample (C8-ctrl, G9-ctrl, C5-MUT, E11-MUT, 3F8-WT, 4G7-WT); error bars indicate variability between replicates (SD). FLAG-IP samples showed low background activity in controls, intermediate activity in MUT clones, and higher activity in WT clones, consistent with enrichment of FLAG-tagged HDAC1 activity in the IP fraction. Statistical significance was indicated as follows: ns, p > 0.05; *, p < 0.05; **, p < 0.01; ***, p < 0.001; ****, p < 0.0001 vs. ctrl (one-way ANOVA).*

3.2.4 Sequencing of the CRISPR/Cas9 clones

To confirm the presence or absence of the point mutation in the catalytic center of clones carrying FLAG-tagged HDAC1 isoforms, nested PCR followed by Sanger sequencing was performed together with lab rotation student Mia Vican on isolated genomic DNA. Given the design of the primers employed, amplification was restricted to the region encompassing the HDAC1 catalytic center.

Successful amplification by nested PCR was first assessed by agarose gel electrophoresis of the PCR amplicons (**Figure 39**, **Figure 40**).

Following the first PCR reaction, multiple bands were observed across all lanes, including the water negative control (**Figure 39**). The non-specific banding pattern is a result of the long-range primer pair ~2900 bp, whose reverse primer anneals to a genomic region outside the vector construct. At this scale, the primers inevitably bind to multiple non-specific sites across the genome, generating spurious amplicons alongside the target band. The bands observed in the water negative control are attributable to primer dimer formation, a common artefact in first-round PCR reactions, particularly with longer primers, whereby in the absence of a DNA template the primers preferentially anneal to each other to form short artifactual products. This behavior is inherent to the nested PCR strategy, in which the first reaction serves as a broad, permissive enrichment step and specificity is conferred by the internal primer pair in the second reaction.

Accordingly, the second PCR reaction gave notably cleaner results (**Figure 40**). The water negative controls from both rounds of PCR produced no detectable bands, confirming the absence of contamination. Negative control clones 1G3G9 and 1G3C8 likewise produced no detectable bands, confirming the absence of a FLAG-tagged HDAC1 insert in these clones. All remaining clones yielded a single band of the expected size of 314 bp, confirming specific and successful amplification.

The sequencing results for each clone were subsequently aligned with the *Mus musculus* WT HDAC1 reference sequence (NCBI: NM_008228.3) using Nucleotide BLAST (**Figure 41A**, **Figure 42A**), and chromatogram data were inspected using SnapGene Viewer (**Figure 41B**, **Figure 42B**). Clones 4G7 and 3F8 showed 100% sequence identity with the WT HDAC1 reference sequence, and their chromatograms displayed sharp, distinct peaks with minimal background noise, supporting high sequence reliability (**Figure 41**). All clones expressing H141A HDAC1 showed 99% sequence identity with the reference sequence, with the single nucleotide deviation corresponding to the intended point mutation, and their chromatograms displayed sharp, distinct peaks with minimal background noise, supporting high sequence reliability. In the chromatograms, each peak represents the fluorescent signal of a dye-labelled dideoxynucleoside incorporated during the sequencing reaction, with each nucleotide assigned a distinct color (A, green; C, blue; G, black; T, red). The well-resolved peak morphology and minimal background signal observed across all clones confirmed reliable base calling and thus the integrity of the sequencing data.

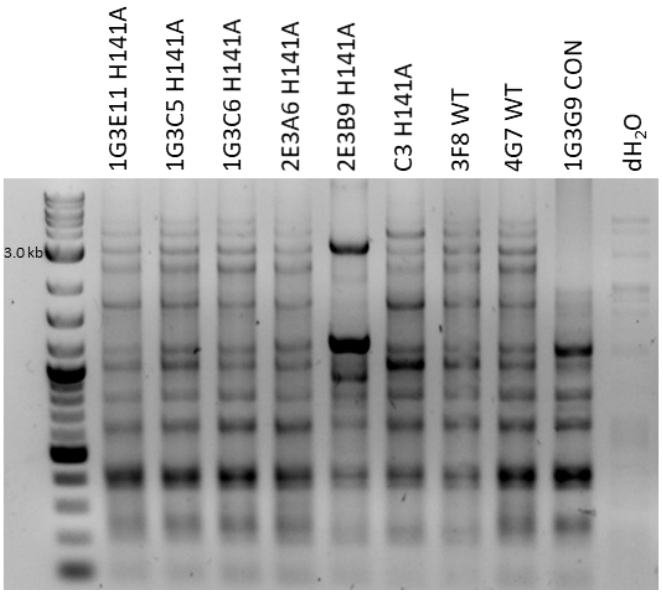

Figure 39: Gel electrophoresis analysis of amplicons from the first PCR reaction of a nested PCR.

Genomic DNA was extracted from CRISPR/Cas9 generated cell lines expressing FLAG-tagged WT or H141A HDAC1, as well as from a control cell line expressing only endogenous HDAC1. As a negative control, dH2O was used instead of the DNA template. The resulting amplicons of 2900 bp were separated on a 1.5% agarose gel by running the electrophoresis for 45 min at 90 V. WT – clones expressing FLAG-tagged WT HDAC1; H141A – clones expressing FLAG-tagged H141A catalytically inactive HDAC1; CON – control clones expressing only endogenous HDAC1; dH2O – a negative control in which dH2O of the first PCR reaction was used instead of DNA template.

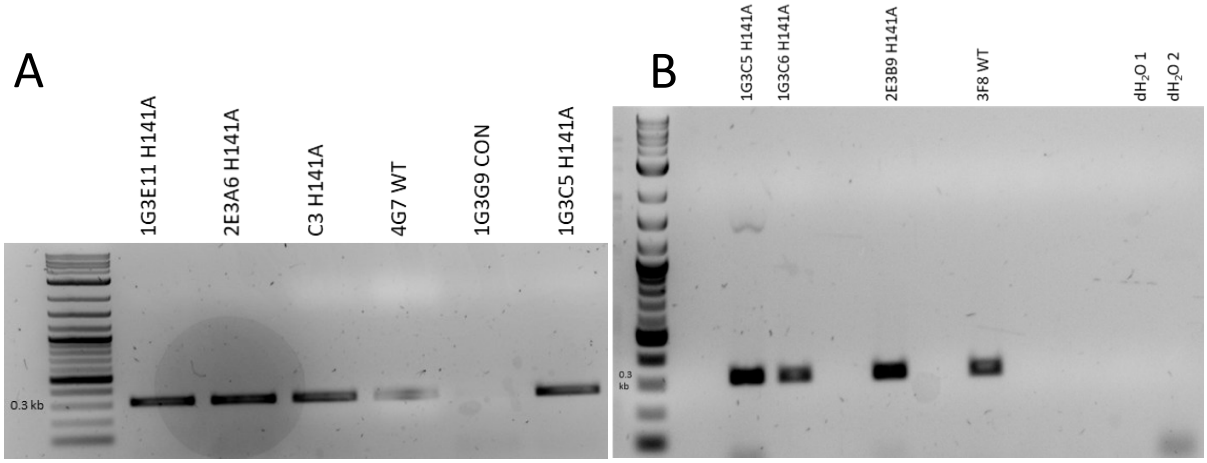

Figure 40: Gel electrophoresis analysis of amplicons from the second PCR reaction of a nested PCR.

Genomic DNA was extracted from CRISPR/Cas9 generated cell lines expressing FLAG-tagged WT or H141A HDAC1, as well as from a control cell line expressing only endogenous HDAC1. As negative controls, dH_2O of both PCR reactions were used instead of the DNA template. The resulting final amplicons of 314 bp were separated on a 1.5% agarose gel by running the electrophoresis for 45 min at 90 V. WT – clones expressing FLAG-tagged WT HDAC1; H141A – clones expressing FLAG-tagged H141A catalytically inactive HDAC1; CON – control clones expressing only endogenous HDAC1; dH_2O 1– a negative control in which dH_2O of the first PCR reaction was used instead of DNA template; dH_2O 2 – a negative control in which dH_2O of the second PCR reaction was used instead of DNA template

A

Score	Expect	Identities	Gaps	Strand
488 bits(264)	4e-134	264/264(100%)	0/264(0%)	Plus/Plus

```
Query  1    ATTCAATGTTGGTGAGGACTGTCCGGTGTTTGATGGCTTGTTTGAGTTCTGTCAGTTGTC  60
            ||||||||||||||||||||||||||||||||||||||||||||||||||||||||||||
Sbjct  373  ATTCAATGTTGGTGAGGACTGTCCGGTGTTTGATGGCTTGTTTGAGTTCTGTCAGTTGTC  432

Query  61   CACGGGAGGCTCTGTCGCAAGTGCTGTGAAGCTTAATAAGCAGCAGACGGACATCGCTGT  120
            ||||||||||||||||||||||||||||||||||||||||||||||||||||||||||||
Sbjct  433  CACGGGAGGCTCTGTCGCAAGTGCTGTGAAGCTTAATAAGCAGCAGACGGACATCGCTGT  492

Query  121  GAACTGGGCCGGGGGCCTGCACCATGCAAAGAAGTCTGAAGCTTCTGGCTTCTGTTACGT  180
            ||||||||||||||||||||||||||||||||||||||||||||||||||||||||||||
Sbjct  493  GAACTGGGCCGGGGGCCTGCACCATGCAAAGAAGTCTGAAGCTTCTGGCTTCTGTTACGT  552

Query  181  CAATGACATCGTCCTGGCCATCCTGGAACTGCTAAAGTACCACCAGAGGGTGCTCTATAT  240
            ||||||||||||||||||||||||||||||||||||||||||||||||||||||||||||
Sbjct  553  CAATGACATCGTCCTGGCCATCCTGGAACTGCTAAAGTACCACCAGAGGGTGCTCTATAT  612

Query  241  TGACATTGATATTCACCATGGCGA  264
            ||||||||||||||||||||||||
Sbjct  613  TGACATTGATATTCACCATGGCGA  636
```

B

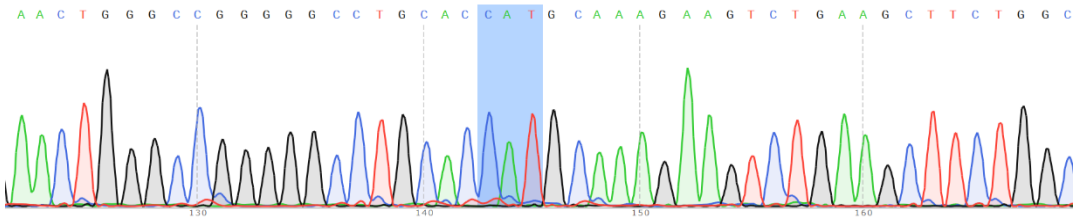

Figure 41: Exemplary analysis of Sanger sequencing results for a clone expressing the Flag-tagged WT HDAC1

(A) Alignment of the clone sequence (Query) with WT Mus musculus HDAC1 sequence, NCBI: NM_008228.3 (Sbjct) was performed using Nucleotide BLAST. The catalytic trinucleotide coding for the WT His residue is framed in red. (B) Segment of the analyzed chromatogram depicting the clone sequence around the catalytic trinucleotide.

A

Score	Expect	Identities	Gaps	Strand
468 bits(253)	5e-128	259/262(99%)	0/262(0%)	Plus/Plus

```
Query  1    TCAATGTTGGTGAGGACTGTCCGGTGTTTGATGGCTTGTTTGAGTTCTGTCAGTTGTCCA  60
            ||||||||||||||||||||||||||||||||||||||||||||||||||||||||||||
Sbjct  375  TCAATGTTGGTGAGGACTGTCCGGTGTTTGATGGCTTGTTTGAGTTCTGTCAGTTGTCCA  434

Query  61   CGGGAGGCTCTGTCGCAAGTGCTGTGAAGCTTAATAAGCAGCAGACGGACATCGCTGTGA  120
            ||||||||||||||||||||||||||||||||||||||||||||||||||||||||||||
Sbjct  435  CGGGAGGCTCTGTCGCAAGTGCTGTGAAGCTTAATAAGCAGCAGACGGACATCGCTGTGA  494

Query  121  ACTGGGCCGGGGGCCTGCACGCCGCAAAGAAGTCTGAAGCTTCTGGCTTCTGTTACGTCA  180
            |||||||||||||||||||| ||||||||||||||||||||||||||||||||||||||||
Sbjct  495  ACTGGGCCGGGGGCCTGCACCATGCAAAGAAGTCTGAAGCTTCTGGCTTCTGTTACGTCA  554

Query  181  ATGACATCGTCCTGGCCATCCTGGAACTGCTAAAGTACCACCAGAGGGTGCTCTATATTG  240
            ||||||||||||||||||||||||||||||||||||||||||||||||||||||||||||
Sbjct  555  ATGACATCGTCCTGGCCATCCTGGAACTGCTAAAGTACCACCAGAGGGTGCTCTATATTG  614

Query  241  ACATTGATATTCACCATGGCGA  262
            |||||||||||||||||||||||
Sbjct  615  ACATTGATATTCACCATGGCGA  636
```

B

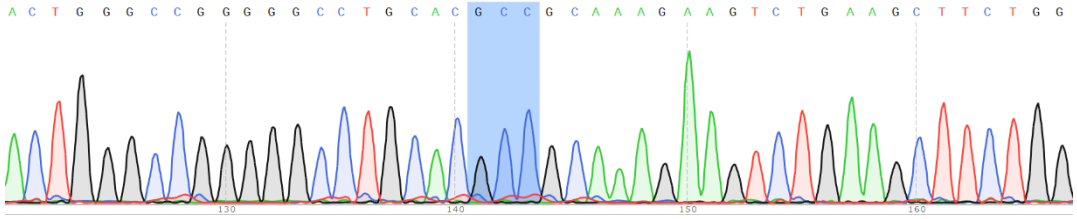

Figure 42: Exemplary analysis of Sanger sequencing results for a clone expressing the Flag-tagged H141A HDAC1

(A) Alignment of the clone sequence (Query) with WT Mus musculus HDAC1 sequence, NCBI: NM_008228.3 (Sbjct) was performed using Nucleotide BLAST. The mutated catalytic trinucleotide coding for the Ala residue is framed in red. (B) Segment of the analysed chromatogram depicting the clone sequence around the mutated catalytic trinucleotide.

3.3 Characterization of HDAC1 knock-in clones under steady state and lipid-inducing conditions

3.3.1 Immunofluorescent staining

Previous experiments showed that lipogenic stimulation with insulin+TO901317 and class I HDAC inhibition with MS-275 increased lipid accumulation in SZ95 sebocytes. To determine whether these treatments also altered the abundance of selected proteins in the generated clones expressing catalytic inactive HDAC1, lipid related protein expression was compared across the clones by immunofluorescence staining under different conditions.

Following stimulation of clonal cells with different conditions to induce lipid droplet formation, immunofluorescence staining was performed using the indicated antibodies to compare treatment-dependent changes in protein levels and/or signal intensity across the different clone backgrounds.

3.3.1.1 H2BK5ac and H3K27ac staining

Previous work using SZ95 sebocytes indicated that perturbation of class I HDAC function can induce transcriptional programs linked to lipogenesis. To assess whether the generated transgenic clones exhibited global changes in chromatin acetylation compared to negative control cells, immunostaining was performed for the histone acetylation marks H2BK5ac and H3K27ac. Both marks have been shown to increase upon HDAC1 inhibition or degradation [39] and are associated with active enhancers and promoters, being commonly enriched in open, transcriptionally active chromatin.

Cells from the transgenic catalytically inactive populations (#1G3E11, #1G3C5) and the negative controls (#1G3G9, #2E3B4) were fixed and stained with antibodies against H2BK5ac and H3K27ac, followed by fluorescence imaging under identical acquisition settings. Representative images showed comparable nuclear staining patterns and signal intensities across all groups, with no detectable differences between transgenic and control cells.

Overall, these results suggested that introduction of the transgene did not induce overt global alterations in these activation-associated histone acetylation marks under the tested conditions.

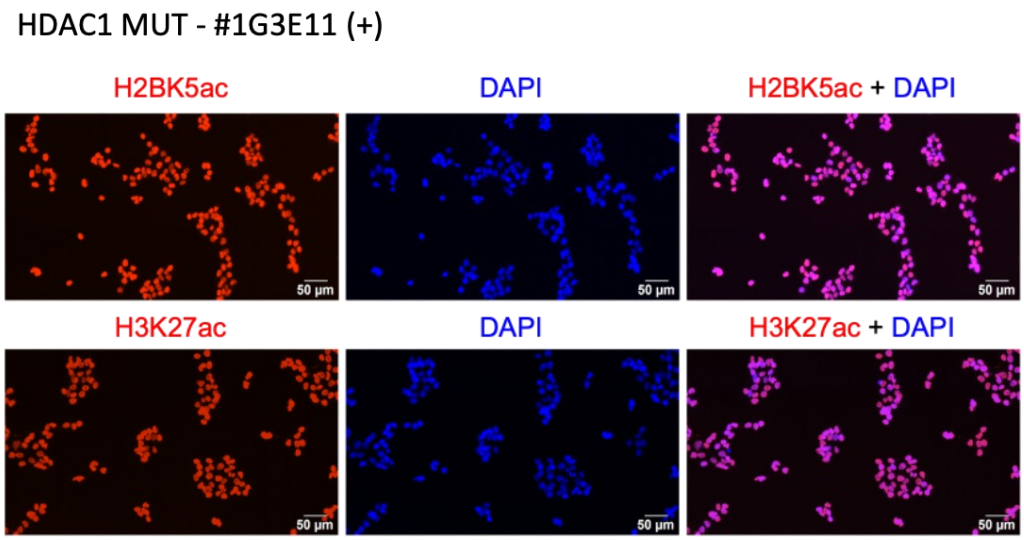

Figure 43: Immunofluorescence staining of histone acetylation markers in the 1G3E11 catalytically inactive clone:

Representative images of 1G3E11 cells stained for H2BK5ac (top row) and H3K27ac (bottom row), two nuclear histone acetylation markers. Histone acetylation signal is shown in red, nuclei are counterstained with DAPI (blue), and merged images (marker + DAPI) are shown on the right, highlighting the nuclear localization of the markers. Scale bar: 50 µm.

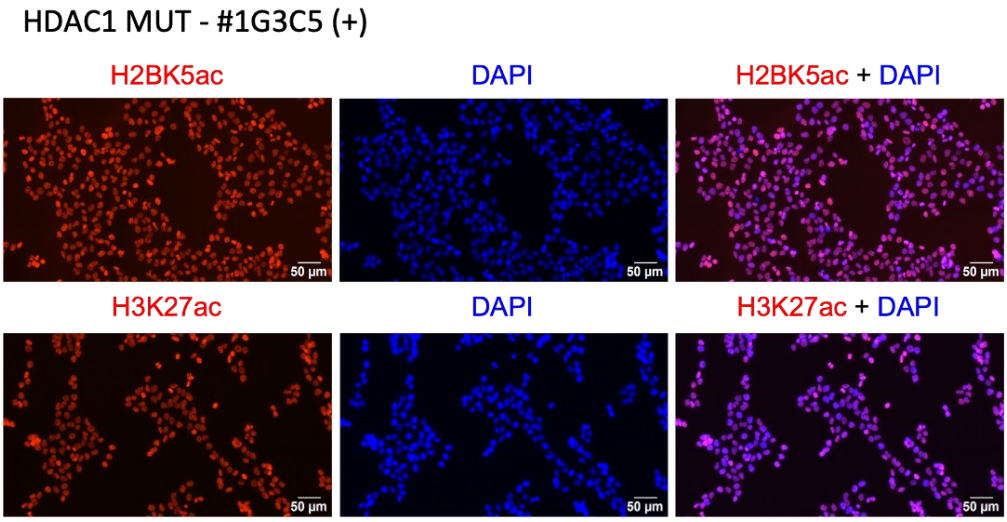

Figure 44: Immunofluorescence staining of histone acetylation markers in the 1G3C5 catalytically inactive clone:

Representative images of 1G3C5 cells stained for H2BK5ac (top row) and H3K27ac (bottom row), two nuclear histone acetylation markers. Histone acetylation signal is shown in red, nuclei are counterstained with DAPI (blue), and merged images (marker + DAPI) are shown on the right, highlighting the nuclear localization of the markers. Scale bar: 50 µm.

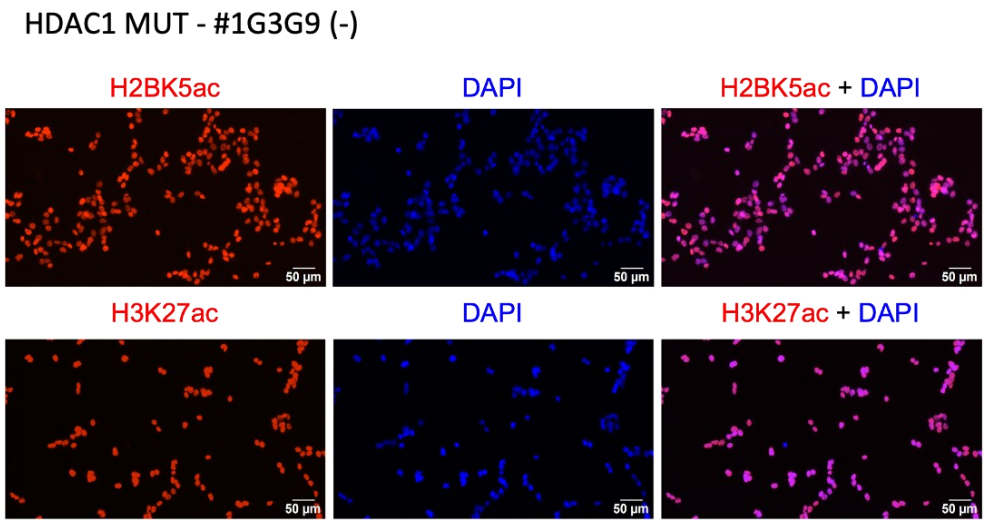

Figure 45: Immunofluorescence staining of histone acetylation markers in the 1G3G9 negative control clone: *Representative images of 1G3G9 cells stained for H2BK5ac (top row) and H3K27ac (bottom row), two nuclear histone acetylation markers. Histone acetylation signal is shown in red, nuclei are counterstained with DAPI (blue), and merged images (marker + DAPI) are shown on the right, highlighting the nuclear localization of the markers. Scale bar: 50 µm.*

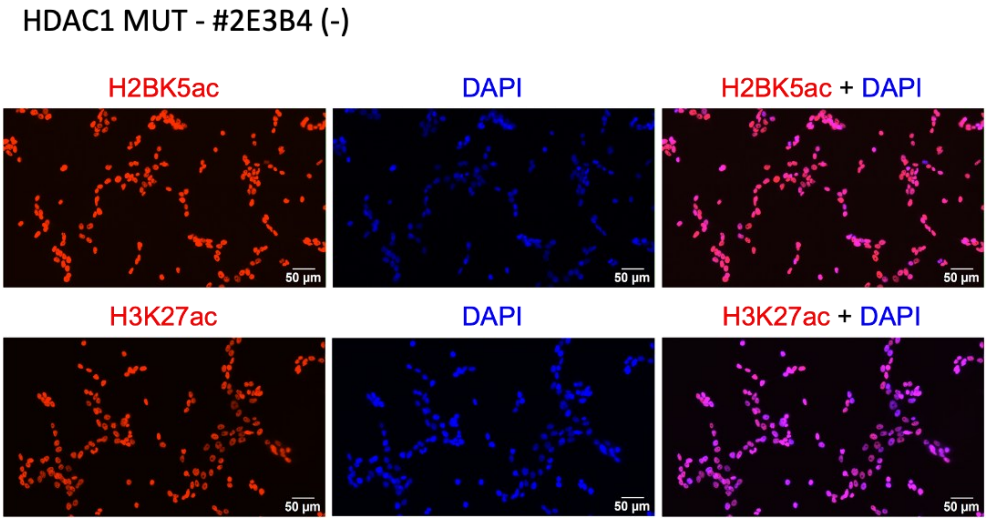

Figure 46: Immunofluorescence staining of histone acetylation markers in the 2E3B4 negative control clone: *Representative images of 2E3B4 cells stained for H2BK5ac (top row) and H3K27ac (bottom row), two nuclear histone acetylation markers. Histone acetylation signal is shown in red, nuclei are counterstained with DAPI (blue), and merged images (marker + DAPI) are shown on the right, highlighting the nuclear localization of the markers. Scale bar: 50 µm.*

3.3.1.2 FAS staining

To test whether fatty acid synthase (FAS) protein expression responded to these treatments in the generated cell populations, FAS immunostaining was compared across stimulation and inhibition conditions on the catalytically inactive populations (#1G3E11, #1G3C5) and the negative control (#1G3G9, #2E3B4).

Cells were treated with DMSO (control), insulin+TO901317, MS-275, or the combined insulin+TO901317+MS-275 condition and then processed for FAS immunofluorescence. No detectable FAS signal was observed in the negative control population. In the cell lines expressing catalytic inactive HDAC1 H141A (HDAC1 MUT), FAS staining was weakest under DMSO, increased under insulin+TO901317and under MS-275 alone, and was most pronounced under the combined insulin+TO901317+MS-275 treatment.

Overall, these staining patterns indicated that FAS protein expression in H141A HDAC1 cells is increased in response to lipogenic stimulation and HDAC inhibition, with the strongest induction observed when both treatments were combined, consistent with enhanced activation of the lipogenic program under these conditions *and in response to catalytic inhibition of HDAC1*

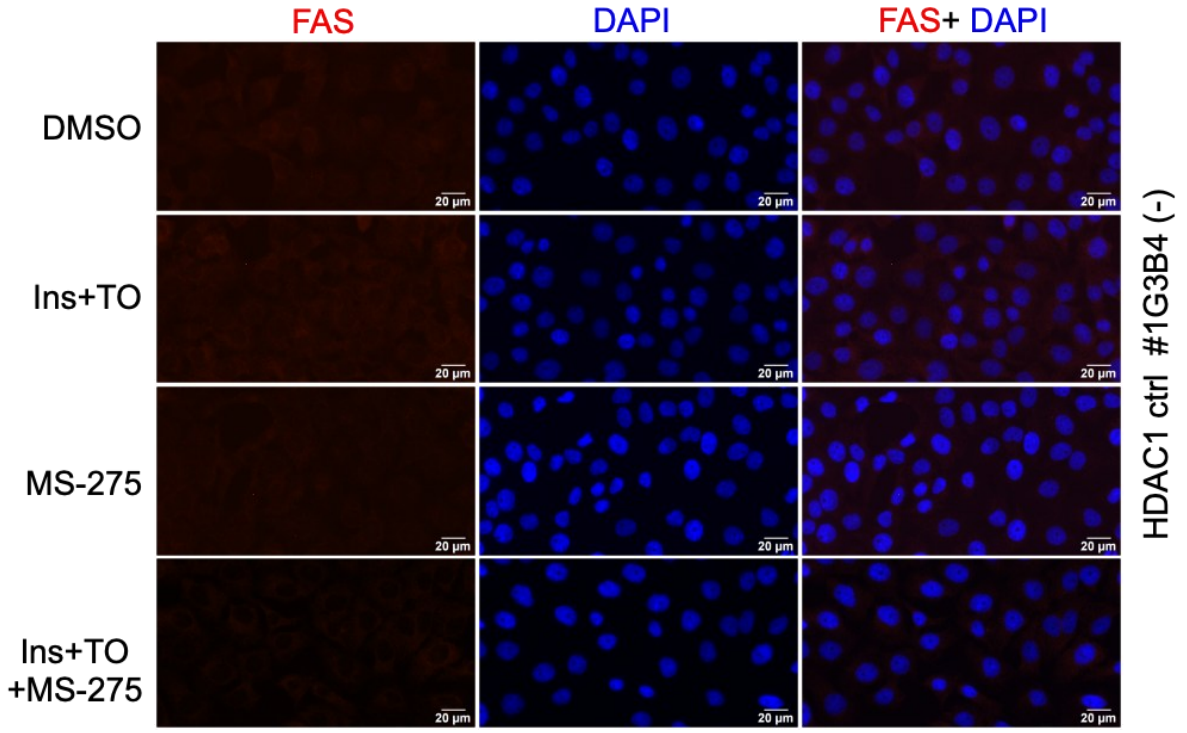

Figure 47: Immunofluorescence staining of histone acetylation markers in the #1G3B4 negative control clone
Representative images of 1G3B4 cells stained for FAS under DMSO (1:1000; first row), insulin+TO901317 (ins+TO; second row), MS-275 (third row) and insulin+TO901317+MS-275 (ins+TO+MS-275; bottom row) treatment conditions. FAS signal (expected in red) was not detected in this negative control clone. Nuclei were counterstained with DAPI (blue), and merged images (FAS+DAPI) are shown on the left. Scale bar: 50 µm.

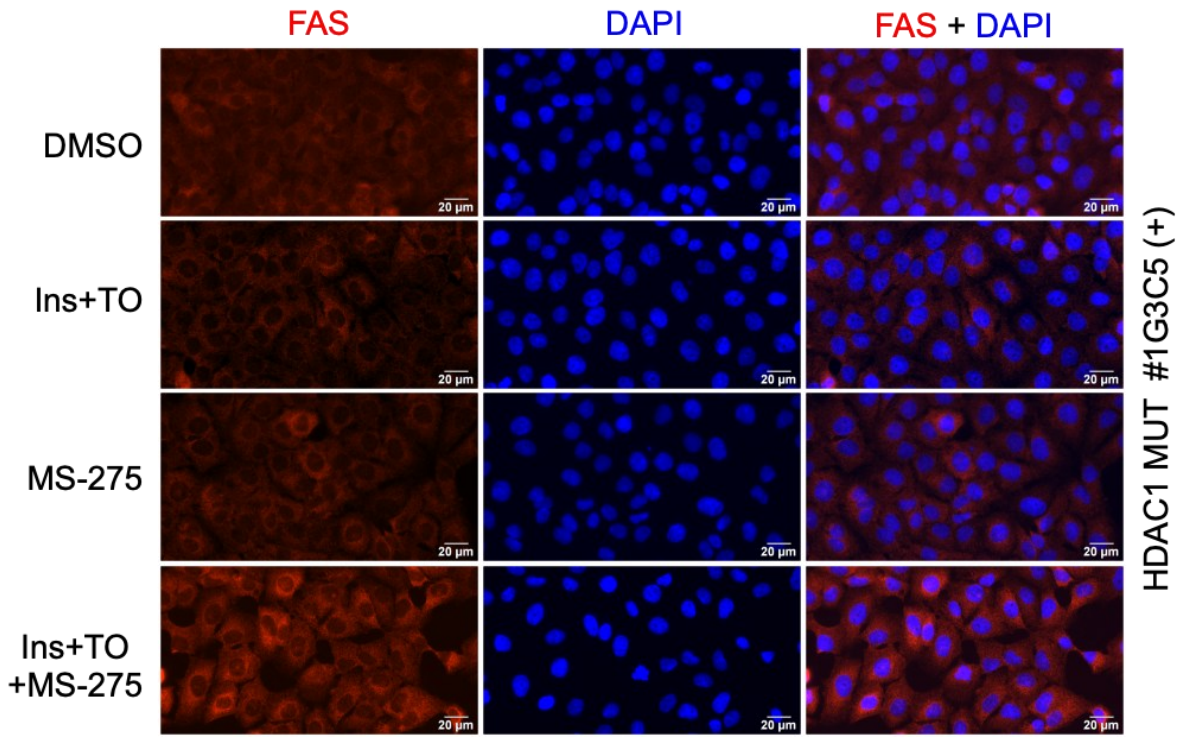

Figure 48: Immunofluorescence staining of histone acetylation markers in the #1G3C5 catalytically inactive clone

Representative images of 1G3C5 cells stained for FAS under DMSO (1:1000; first row), insulin+TO901317 (ins+TO; second row), MS-275 (third row) and insulin+TO901317+MS-275 (ins+TO+MS-275; bottom row) treatment conditions. FAS signal is shown in red, nuclei were counterstained with DAPI (blue), and merged images (FAS+DAPI) are shown on the left, highlighting the cytoplasmic localization of FAS. Scale bar: 50 µm.

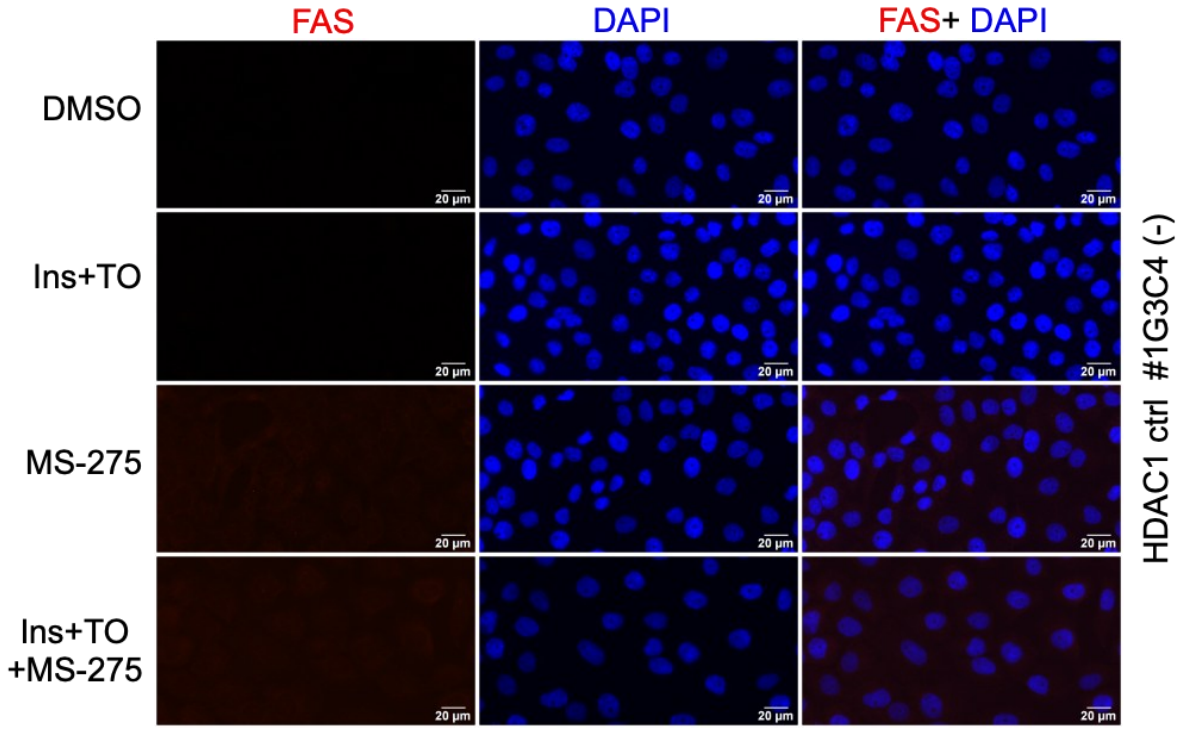

Figure 49: Immunofluorescence staining of histone acetylation markers in the #1G3C4 negative control clone

Representative images of 1G3C4 cells stained for FAS under DMSO (1:1000; first row), insulin+TO901317 (ins+TO; second row), MS-275 (third row) and insulin+TO901317+MS-275 (ins+TO+MS-275; bottom row) treatment conditions. FAS signal (expected in red) was not detected in this negative control clone. Nuclei were counterstained with DAPI (blue), and merged images (FAS+DAPI) are shown on the left. Scale bar: 50 µm.

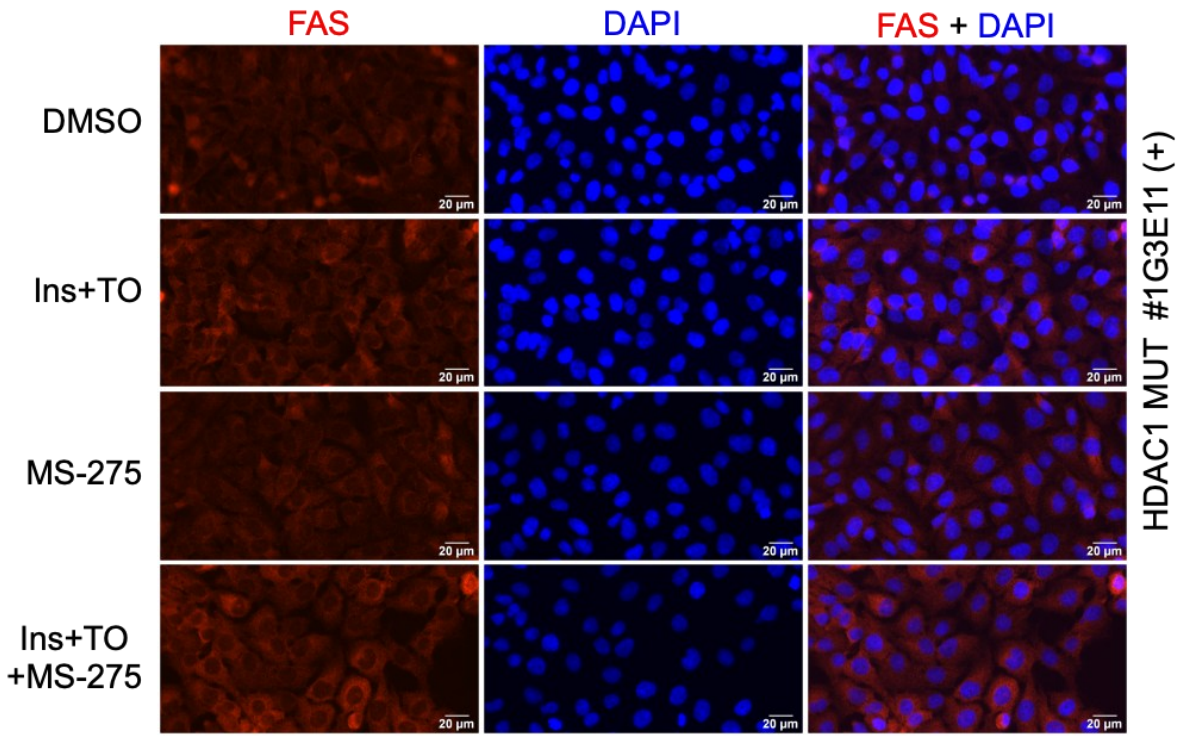

Figure 50: Immunofluorescence staining of histone acetylation markers in the #1G3E11 catalytically inactive clone

Representative images of 1G3E11 cells stained for FAS under DMSO (1:1000; first row), insulin+TO901317 (ins+TO; second row), MS-275 (third row) and insulin+TO901317+MS-275 (ins+TO+MS-275; bottom row) treatment conditions. FAS signal is shown in red, nuclei were counterstained with DAPI (blue), and merged images (FAS+DAPI) are shown on the left, highlighting the cytoplasmic localization of FAS. Scale bar: 50 µm.

3.3.2 Evaluation of the siRNA-mediated knockdown of HDAC1 and HDAC2 in the clones and subclones

Previous experiments suggested that class I HDAC perturbation influences lipid metabolism and that HDAC1 and HDAC2 can compensate for each other. To test whether endogenous HDAC1 could be depleted while preserving the catalytically inactive FLAG-tagged HDAC1 knock-in (KI) allele siRNA-mediated HDAC1 knockdown was performed and evaluated by Western blotting. In addition, HDAC2 knockdown was performed in the catalytically inactive HDAC1 H141A (MUT) clones to assess whether HDAC1 would be upregulated in this background as part of a compensatory response.

Western blot analysis showed that HDAC1 siRNA reduced both the endogenous HDAC1 band and the catalytically inactive KI HDAC1 band, indicating that the knockdown did not discriminate between the two HDAC1 protein pools. β-actin was used as the loading control for normalization. Consistent with prior observations, HDAC1 knockdown was accompanied by increased HDAC2 protein levels, showing compensatory upregulation even under these conditions. Conversely, HDAC2 knockdown led to a reciprocal increase in HDAC1, including in the catalytically inactive HDAC1 H141A (MUT) clones, indicating that compensatory regulation of HDAC1 can still occur even when the KI allele lacks catalytic activity.

Overall, these data indicated that the attempted strategy to selectively remove endogenous HDAC1 while retaining the catalytically inactive KI allele was not successful, and that HDAC1/HDAC2 compensation remained a relevant confounding factor in knockdown-based experiments.

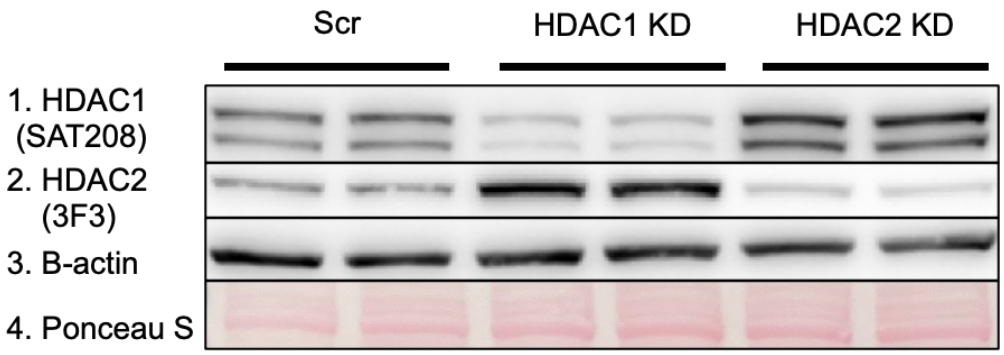

Figure 51: Evaluation of HDAC1 and HDAC2 knockdown in 1G3C5 H141A mutant clones:
Western blot analysis of lysates from FLAG-positive 1G3C5 SZ95 cells expressing the catalytically inactive HDAC1 H141A, that undergo siRNA-mediated knockdown of HDAC1 or HDAC2, with scrambled siRNA(scr) as negative control. β-actin and Ponceau S staining were used as a loading control.

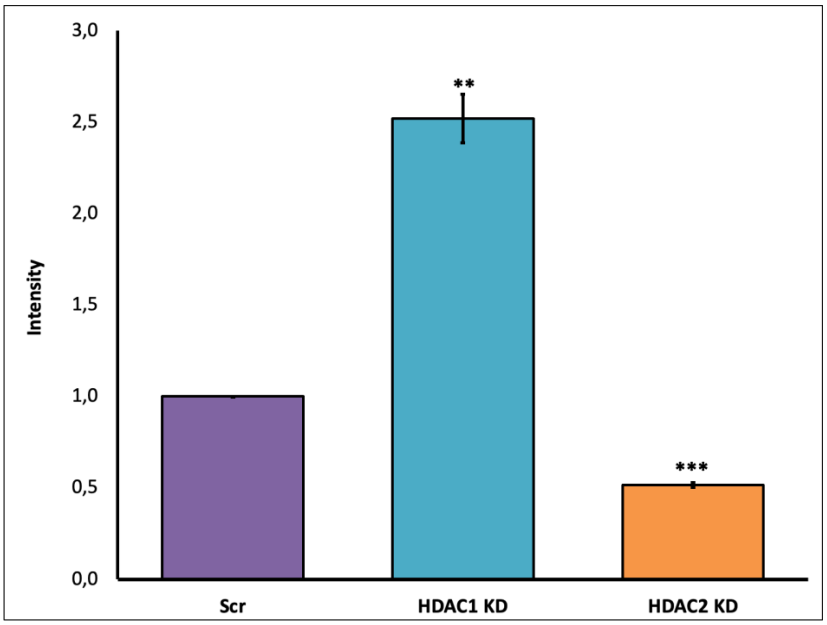

Figure 52 Quantification of HDAC2 protein levels by Western blot analysis following HDAC1 and HDAC2 knockdown in 1G3C5 H141A mutant clones:
*Densitometric analysis of Western blot data showing HDAC2 protein levels in FLAG-positive 1G3C5 SZ95 cells treated with siRNA targeting HDAC1, HDAC2, or scrambled control (scr). HDAC2 protein levels were reduced upon HDAC2 knockdown and increased upon HDAC1 knockdown compared to control conditions. Data are presented as mean intensity values ± standard deviation (SD). Statistical significance was defined as ns, $p > 0.05$; *, $p < 0.05$; **, $p < 0.01$; ***, $p < 0.001$; ***, $p < 0.0001$ vs. scr (one-way ANOVA).*

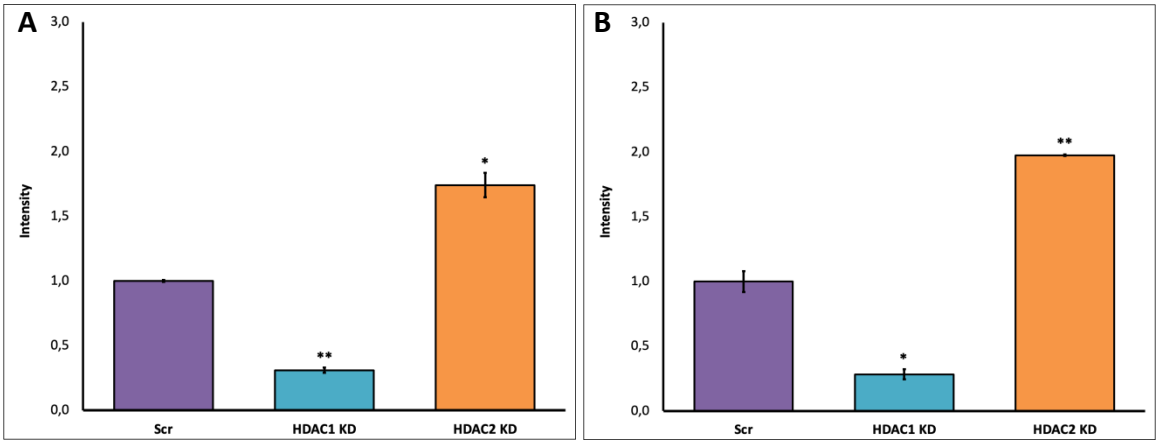

Figure 53: Quantification of endogenous (A) and catalytically inactive (B) HDAC1 protein levels following HDAC1 and HDAC2 knockdown in 1G3C5 H141A mutant clones:

*Densitometric analysis of Western blot data showing HDAC1 protein levels for the endogenous (A) and the catalytically inactive H141A allele (B) in FLAG-positive 1G3C5 SZ95 cells treated with siRNA targeting HDAC1, HDAC2, or scrambled control (scr). HDAC1 protein levels were increased upon HDAC2 knockdown and reduced upon HDAC1 knockdown for both the endogenous (A) and mutant (B) forms compared to control conditions. Data are presented as mean intensity values ± standard deviation (SD). Statistical significance was defined as ns, $p > 0.05$; *, $p < 0.05$; **, $p < 0.01$; ***, $p < 0.001$; ***, $p < 0.0001$ vs. scr (one-way ANOVA).*

3.1 Assessment of co-repressor complex formation with HDAC1 isoforms

To verify whether the H141A mutation affects the structural role of HDAC1 in co-repressor complex formation, Western blot analysis was performed together with lab rotation student Mia Vican on total cell lysates and FLAG immunoprecipitation (IP) samples derived from the generated clones.

In whole-cell lysates, the negative control clone displayed a single HDAC1 band corresponding to endogenous HDAC1. In contrast, H141A clones showed two bands: the endogenous HDAC1 at lower molecular weight and the FLAG-tagged HDAC1H141A at a slightly higher molecular weight, reflecting the additional FLAG tag. This confirmed successful expression of the CI allele alongside the endogenous protein.

In the FLAG immunoprecipitation, no HDAC1 signal was detected in the IP fraction of the negative control clone, confirming pull-down specificity for FLAG-tagged proteins. In KI clones, both the FLAG-tagged and endogenous HDAC1 were detected in the IP fraction, with endogenous HDAC1 bands (red arrows) visible just below the heavier FLAG-tagged isoforms. This indicates that both forms are incorporated into the same protein complexes and that FLAG-based immunoprecipitation captures associated endogenous HDAC1 through these interactions.

Co-repressor complex components (Sin3A, CoREST, MTA2, and Sap30) and HDAC2 were successfully co-immunoprecipitated with FLAG-tagged HDAC1 isoforms, demonstrating that the HDAC1 H141A isoforms efficiently form stable co-repressor complexes.

These results indicate that endogenous HDAC1 co-immunoprecipitants with co-repressor complex components (Sin3A, CoREST, MTA2, and Sap30) as well as HDAC2, demonstrating that both the FLAG-tagged and endogenous HDAC1 isoforms are incorporated into the same co-repressor complexes. Overall, these findings confirm that HDAC1H141A is properly integrated into native HDAC1-containing complexes similar than HDAC1WT and that FLAG-

based immunoprecipitation captures the associated endogenous HDAC1 through these shared interactions.

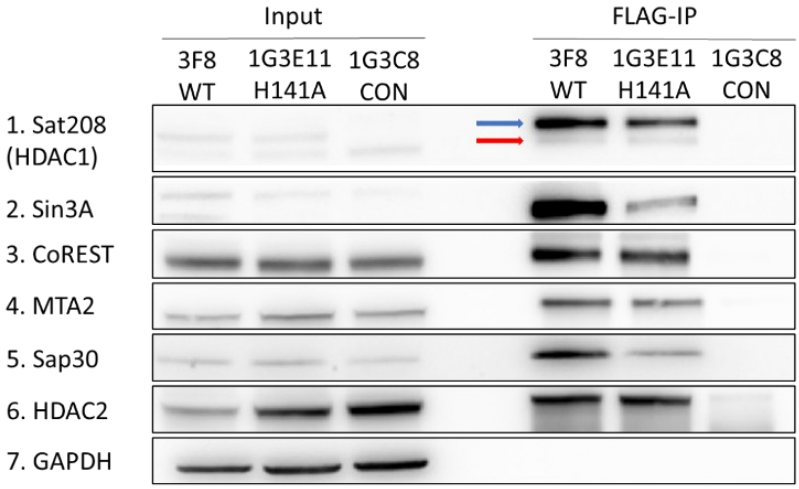

Figure 54: Input and FLAG immunoprecipitation (FLAG-IP) analysis of KI HDAC1 clones

Western blot analysis of CRISPR/Cas9 generated cell lines expressing FLAG-tagged WT or H141A HDAC1, alongside a control cell line expressing only endogenous HDAC1. Blue arrow – FLAG-tagged HDAC1 isoform; red arrow – endogenous HDAC1; WT – clones expressing FLAG-tagged WT HDAC1; H141A – clones expressing FLAG-tagged H141A catalytically inactive HDAC1; CON – control cell lines expressing only the endogenous HDAC1.

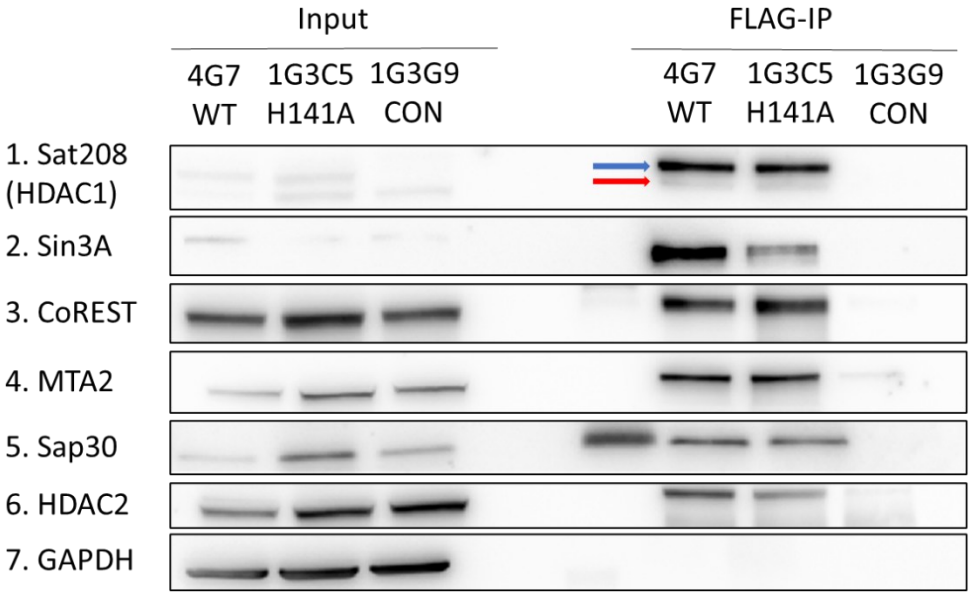

Figure 55: Input and FLAG immunoprecipitation analysis of KI HDAC1 clones

Western blot analysis of CRISPR/Cas9 generated cell lines expressing FLAG-tagged WT or H141A HDAC1, alongside a control cell line expressing only endogenous HDAC1. Blue arrow – FLAG-tagged HDAC1 isoform; red arrow – endogenous HDAC1; WT – clones expressing FLAG-tagged WT HDAC1; H141A – clones expressing FLAG-tagged H141A catalytically inactive HDAC1; CON – control cell lines expressing only the endogenous HDAC1.

3.1.1 Lipid gene expression in clones after insulin and LXR agonist stimulation

Previous experiments showed that chemical inhibition of class I HDACs with MS-275 promotes lipid accumulation and upregulation of lipid-associated proteins in SZ95 sebocytes. To test whether catalytic inactivation of HDAC1 similarly enhances lipid protein expression upon lipogenic stimulation, Western blot analysis was performed comparing negative control clones with clones carrying the catalytically inactive HDAC1 KI allele.

Cells were treated with DMSO (1:1000; control) or insulin + TO901317, followed by protein extraction and Western blotting for FAS, PEPCK, and HDAC1. β-actin was used as a loading control for normalization.

Without stimulation, FAS protein levels were found to similar between control cells and HDAC1 H141A cells. However, after stimulation with insulin and LXR-agonist, HDAC1 H141A clones showed moderately increased FAS protein levels, suggesting that expression of catalytically inactive HDAC1 may further enhance FAS expression to some extent. In contrast, HDAC1 protein levels did not show notable differences across treatment conditions or between clone types.

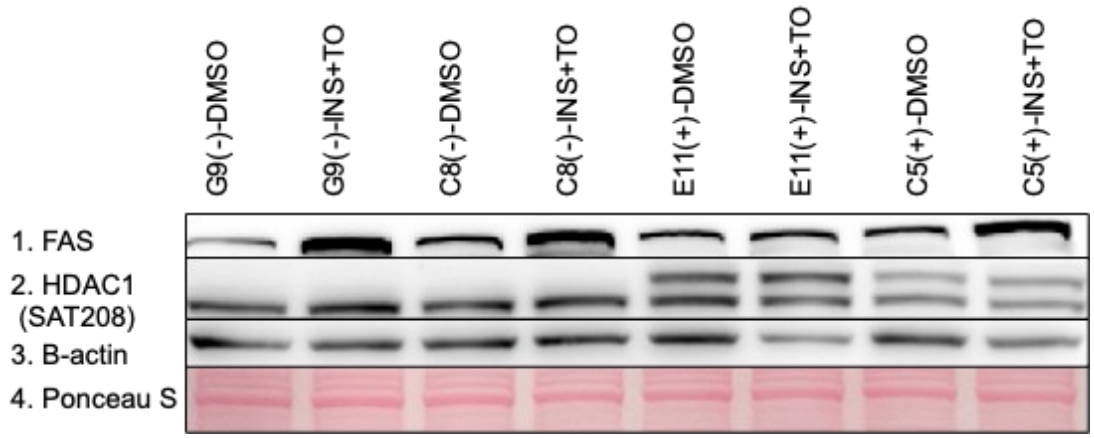

Figure 56: Evaluation of lipid induction genes in cataleptically inactive and wild-type clones: *Western blot analysis of lysates from FLAG-negative 1G3G9, 1G3C8, and FLAG-positive 1G3E11,1G3C5 SZ95 cells expressing the wild-type and respectively the catalytically inactive HDAC1 H141A, that undergo insulin+ TO901317 (ins+TO) treatment, with DMSO as negative control. β-actin and Ponceau S staining were used as a loading control.*

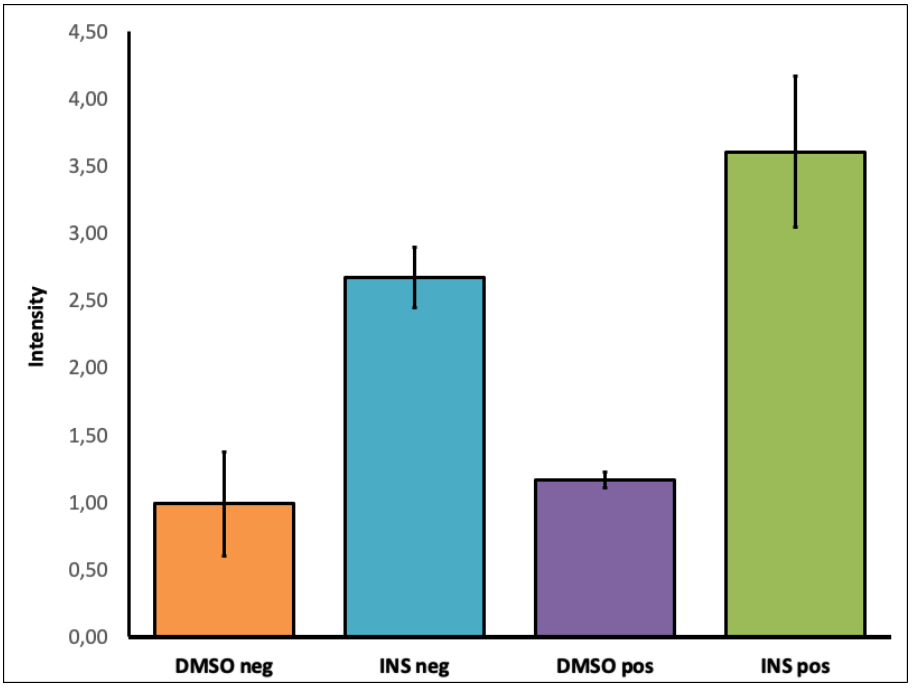

Figure 57: Quantification of FAS protein levels following the insulin+TO901317 treatment in cataleptically inactive and wild-type clones:

Densitometric analysis of Western blot data showing FAS protein levels in FLAG-negative 1G3G9, 1G3C8 (neg), and FLAG-positive 1G3E11,1G3C5 (pos) SZ95 cells expressing the wild-type and respectively the catalytically inactive HDAC1 H141A treated with insulin+TO901317 (INS), or DMSO as control (DMSO). FAS protein levels were increased upon insulin+TO901317 treatment in both the negative and the positive clones, and with a higher increase in the positively transfected cells. Data are presented as mean intensity values ± standard deviation (SD).

4 DISCUSSION

4.1 Effects of insulin, LXR-agonist (TO901317), and MS-275 on the expression of lipid-associated proteins

In our experimental system, insulin treatment consistently upregulates sebocyte lipogenesis. Mechanistically, this response was interpreted within the established model in which insulin activated the insulin receptor (IR) and, at higher concentrations, also engaged IGF-1 receptor (IGF-1R) signaling on sebocytes [54,57,63,73]. Activation of these receptors leads to the activation of the PI3K/Akt/mTOR pathway, promoting phosphorylation of FoxO1 and its nuclear export, thereby reducing nuclear FoxO1 availability [57,60,73]. Reduced nuclear FoxO1 promotes induction of SREBP-1, a master lipogenic transcription factor that switches on the enzymes for *de novo* lipogenesis [57,63]. In line with this, increased SREBP-1 protein levels were observed in our WB analyses (e.g. **Figure 10**). The increased lipid phenotype was observed in ORO staining, where insulin-treated cells showed increased neutral lipid accumulation (e.g. **Figure 11**). Consistent with SREBP-1 pathway activation, elevated levels of FAS protein were also detected in multiple WB (e.g. **Figure 56**), further supporting induction of lipogenesis machinery. Although perilipin 2 (PLIN2) would have provided an additional marker of lipogenesis, it could not be evaluated reliably because the tested antibody did not output detectable signal under our conditions.

The LXR agonist TO901317 further enhanced the lipogenic response and therefore was, together with insulin, an in vitro lipogenesis-inducing stimulus in sebocytes [63,68]. TO901317 was shown to bind to and activates LXRα/β, which directly promotes SREBP-1 expression and its downstream lipogenic targets like FAS and ACCα, thereby amplifying insulin-mediated signaling at the transcriptional level [34,54]. At the same time, the combined insulin+TO901317 treatment was determined to increase p300 expression, leading to increased histone H3 and H4 acetylation at promoter regions of lipogenic genes such as *SREBF-1* and *FASN* [34]. This further facilitates transcriptional activation of the lipogenesis and production of sebum-associated lipids.

Previous experiment from our lab showed that the inhibition of class I HDACs by using MS-275, either alone or in combination with insulin and the LXR agonist TO901317, induced the formation of lipid droplets and increased the expression of many lipid-associated genes, including the transcription factor *SREBF1*. Using a similar experimental setup, results from the present thesis also confirmed that the two important lipid-associated proteins, SCD and SREBP1, where upregulated at the protein level after stimulation with insulin and TO901317. When MS-275 was additionally applied, protein expression was further enhanced, indicating that, for these genes, changes at the RNA level are also reflected at the protein level. Normally HDACs act as negative regulators that suppress SREBP1, but when HDACs are inhibited, the suppression is released, promoting the lipid accumulation [34,74]. When combined with insulin+TO901317, MS-275 sustains the hyperacetylated chromatin by preventing deacetylation, thereby reinforcing transcriptional activation already promoted by p300 [34]. In conclusion, insulin+TO901317+MS-275 functioned as a strong positive-control condition in our experiments, because it engaged the canonical Akt/mTORC1/SREBP-1 lipogenic axis and strengthened promoter acetylation-dependent transcription.

4.2 The effects of the p300 inhibitor A485 on the generation of neutral lipids

Akt signaling is known to propagate lipogenic responses in sebocytes, in part through activation of mTORC1, which can phosphorylate and activate the histone acetyltransferase p300 [55]. This provides a direct link between extracellular metabolic cues, such as insulin stimulation, to chromatin-based regulation of gene expression [55]. p300 functions as a central transcriptional coactivator that promotes histone acetylation and facilitates an open chromatin state at target loci, thereby enabling transcription of genes involved in lipid metabolism [34,51].

In sebocyte lipid metabolism, p300 plays a key role in driving lipogenesis through regulation of the master transcription factor SREBP1 and its downstream targets, including FAS, through enhanced histone acetylation at their promoters [34]. Consistently, lipogenic stimulation with insulin and LXR agonists has been shown to increase p300 activity and expression, further supporting its role as a mediator of hormonally induced lipid production [34,51].

To assess the functional contribution of p300 to the MS-275-induced lipogenic phenotype observed in our system, cells were treated with the selective p300/CBP catalytic inhibitor A-485 in combination with insulin+TO901317+MS-275. ORO staining (**Figure 11**) and quantification of lipid droplet area per nucleus (**Figure 12**) showed that addition of A-485 reduced lipid accumulation to levels comparable to those observed under insulin+TO901317 treatment alone, effectively reversing the additional induction conferred by MS-275. This indicates that the enhanced lipogenesis produced by class I HDAC inhibition is dependent on histone acetylation and p300 catalytic activity.

These findings establish that p300 and class I HDACs act as opposing epigenetic regulators of sebocyte lipid metabolism. While MS-275 promotes lipogenesis by preventing histone deacetylation and maintaining chromatin at lipogenic gene loci in a transcriptionally permissive state, A-485 reduces histone acetylation and attenuates the lipogenesis. The partial rescue (lipid accumulation returns to insulin+TO901317 levels rather than to DMSO control levels) suggests that p300 catalytic activity is specifically required for the HDAC inhibition-driven component of lipid induction, while the baseline lipogenic response to insulin and LXR agonism operates through additional mechanisms that are not p300-dependent.

Taken together, these data support a model in which the balance between histone acetylation, mediated by p300, and deacetylation, mediated by class I HDACs including HDAC1, constitutes a key epigenetic switch governing the magnitude of sebocyte lipid synthesis.

4.3 Knockdown of HDAC1, HDAC2 and HDAC3 by siRNA and consequences for generation of neutral lipids

Since it was showed that MS-275 inhibits all class I HDACs (HDAC1, HDAC2, and HDAC3) [39], siRNA-mediated knockdown experiments were designed to identify which family members are individually responsible for the observed effects on lipid droplet formation by sebocytes. HDAC1, HDAC2, and HDAC3 were therefore knocked down individually and in combination, and lipid accumulation was assessed by ORO staining.

Western blot analysis confirmed successful knockdown at the protein level. However, knockdown of HDAC1 resulted in elevated HDAC2 protein levels, while HDAC2 knockdown produced a reciprocal increase in HDAC1 (**Figure 13** and **Figure 15**), a pattern that has been reported previously in the literature [75,76].

The mechanistic basis of this compensatory upregulation is thought to be rooted in the mutual dependence between HDAC1 and HDAC2 and their multi-protein co-repressor complexes[76]. On one hand, isolated HDAC1 and HDAC2 require incorporation into Sin3, NuRD, or CoREST to deacetylate chromatin efficiently, as these scaffolds provide the necessary DNA/chromatin-recognition motifs [76]. On the other hand, the complexes themselves depend on HDAC1 and HDAC2 for structural integrity, loss of either enzyme destabilizes and promotes degradation of key subunits including Sin3A, MTA1, and MTA2[41,48]. Consequently, when one paralog is lost, unoccupied binding sites arise within these scaffolds, and the remaining paralog is more readily recruited and retained within the assembled complex, protecting it from degradation. This mechanism predicts that protein levels of the remaining paralog rise without a corresponding increase in mRNA, suggesting that the free, uncomplexed pool of these enzymes is subject to constitutive degradation and that complex incorporation is the primary determinant of their steady-state abundance [44,47].

Quantitative proteomic analyses in mouse embryonic stem cells have shown that approximately 92% of cellular HDAC1 is localized within three complexes, NuRD (49%), CoREST (28%), and Sin3 (15%), highlighting the degree to which these enzymes are complex-dependent and showing how disruptive single-paralog loss would be to co-repressor stoichiometry [76,77].

ORO quantification (**Figure 20**) revealed that knockdown of HDAC2 and combined knockdown of HDAC1 and HDAC2 resulted in statistically significant increases in lipid content compared to the scrambled control but they are very small, and knockdown of HDAC1 alone or HDAC3 alone did not produce significant changes in lipid accumulation relative to the scrambled control. These results have two non-exclusive mechanistic explanations. First, the reciprocal stabilization loop itself acts as a partial buffer: loss of one paralog elevates the other, sustaining partial complex activity and potentially masking the lipogenic effect. Second, HDAC1 and HDAC2 often affect the same genes because they work together in the same protein complexes. As a result, removing one may not reveal new regulatory regions beyond those already affected by removing the other.

Taken together, these observations indicate that simple knockdown of class I HDAC family members is insufficient to dissect their individual contributions to lipid regulation, likely because of mutual stabilization and functional redundancy within shared complexes. This limitation motivated a change in experimental strategy: a catalytically inactive point mutant (HDAC1 H141A) was introduced to selectively reduce deacetylase activity while preserving protein levels and complex integration.

4.4 Establishment of CUT&RUN

Experiment from previous and present theses using SZ95 sebocytes have shown that treatment with the class I HDAC inhibitor, with and without additional stimulation by insulin and TO901317, results in transcriptional upregulation of many lipid-associated genes and their gene products (i.e. proteins). This indicates that these genes are normally being repressed by histone deacetylase activity of class I HDACs. To investigate the genome-wide binding sites of HDAC1 and to determine the dynamic of changes in key histone modification marks during induction of lipids, one aim of the thesis was to establish a new method in the lab: Cleavage Under Target & Release Using Nuclease (CUT&RUN). Therefore, in the first set of experiments using this method, only the genome wide pattern of the active promotor mark histone H3K5me3 was assessed in cells treated with two conditions: DMSO as control and a combination of insulin, TO0901317 and MS-275. After NGS and bioinformatic processing, several interesting observations could be made: At the *SREBF1* locus, CUT&RUN profiling

revealed two spatially distinct H3K4me3 enriched regions upon combination treatment. A promoter-proximal peak was present under both DMSO and treated conditions, consistent with constitutive activity at the canonical *SREBP-1a* promoter. In addition, a second upstream peak was specifically induced upon insulin+TO901317+MS-275 treatment which was absent under control conditions. The induction of this second peak is consistent with TO901317 mediated activation of LXR, which binds to liver X receptor response elements (LXREs) within the *SREBP-1c* alternative promoter and drives its transcription [34,66,68]. This observation is mechanistically significant because SREBP-1c is the predominant lipogenic isoform in sebocytes, and its LXR-dependent induction represents a key transcriptional amplification step in the lipogenic cascade [66]. Further experiments will show whether the higher H3K5me3 occupancy at the SREBP-1c promotor after lipid induction also results in upregulation of the SREBP-1c mRNA splice variant.

At the of fatty acid synthase (*FASN*) locus, H3K4me3 signal was detected under both DMSO and combination treatment conditions, indicating that the *FASN* promoter is active in SZ95 sebocytes even under basal conditions. Upon combination treatment, H3K4me3 signal intensity was increased above this already elevated baseline, with a broader and higher peak profile reproducible across both replicates. This pattern is indicative of enhanced promoter activation rather than *de novo* activation and is mechanistically consistent with *FASN* being a downstream target of multiple lipogenic pathways [65]. The *FASN* promoter contains a specific LXRE that allows for direct transcriptional activation by LXR, even in the absence of SREBPs [65]. Simultaneously, LXR activation strongly induces the transcription of the *SREBF1-1c* gene itself by binding to LXREs within its alternative promoter, increasing the pool of SREBP-1c precursors available for lipogenic signaling [65–67].

At the ATP-Binding Cassette Subfamily A Member 1 (*ABCA1*) locus, H3K4me3 occupancy was near-absent under DMSO conditions, indicating minimal basal promoter activity. In contrast, combination treatment induced a sharp, well-defined H3K4me3 peak at the *ABCA1* promoter region, reproducible across both biological replicates confirming signal specificity. This pattern represents the clearest example of *de novo* promoter activation among the loci profiled in this study, a transition from an inactive to an active chromatin state rather than enhancement of pre-existing activity. Mechanistically, *ABCA1* is a well-characterized direct transcriptional target of LXR signaling, and its activation is consistent with TO901317-mediated LXR binding to LXREs in the *ABCA1* promoter, with HDAC inhibition by MS-275 likely facilitating chromatin accessibility at this locus [31,67,76,77]. *ABCA1* encodes a cholesterol efflux transporter, and its induction under conditions of enhanced lipid synthesis may reflect a compensatory response to prevent intracellular cholesterol overload as lipogenesis increases [55,67,78]. Alternatively, ABCA1-mediated lipid efflux may contribute to the secretory output of the sebaceous gland, given that cholesterol and its esters constitute a functionally relevant proportion of human sebum [55,58].

At the Stearoyl-CoA desaturase (*SCD*) locus, a prominent H3K4me3 peak was detected at the 5’ promoter region under both DMSO and combination treatment conditions, with the DMSO condition already exhibiting a notably strong basal signal. This high basal H3K4me3 enrichment is consistent with *SCD* being highly expressed in sebocytes, reflecting the central role of Δ9-desaturation in sebaceous lipid synthesis [58]. Upon combination treatment, H3K4me3 signal was further increased above this elevated baseline, although the relative magnitude of this increase was more modest compared to the *ABCA1* and *SREBF1* loci, consistent with an already active promoter with limited capacity for further chromatin-level induction [78]. This result suggests that *SCD* expression in SZ95 sebocytes is subject to an epigenetic activation under basal conditions, and that the combination of treatment produces

further enhancement. From a translational perspective, *SCD* upregulation in the context of HDAC1 inactivation and LXR/insulin co-stimulation is relevant to sebum composition, as SCD-catalyzed monounsaturated fatty acid production contributes to the lipid profile associated with the acne-like sebocyte phenotype [55,58,65,78].

To further evaluate the specificity of the observed H3K4me3 changes, three additional loci were examined: *DLX2*, *ZNF713*, and *EOLA2*. In contrast to the lipogenic target genes, all three loci displayed reduced H3K4me3 signal under combination treatment relative to DMSO. None of these genes have established roles in sebocyte lipid metabolism or the lipogenic regulatory network, and their inclusion was therefore not motivated by mechanistic expectation but rather by their value as specificity controls for the CUT&RUN assay. The observation that H3K4me3 changes were not globally positive across all profiled loci argues against a non-specific or artifactual genome-wide increase in this mark under the treatment conditions used. Instead, it supports the interpretation that the H3K4me3 enrichment observed at *SREBF1*, *FASN*, *SCD*, and *ABCA1* reflects targeted, biologically relevant chromatin remodeling at lipogenic gene loci, rather than a consequence of technical noise or indiscriminate chromatin opening.

4.5 Generation and characterisation of the SZ95 sebocyte cell lines expressing catalytic inactive HDAC1H141A

Since siRNA-mediated knockdown resulted in compensatory upregulation of HDAC2 and only a minor increase of lipid droplet formation, a CRISPR/Cas9-mediated knock-in strategy was used to generate SZ95 sebocyte cell lines that express catalytically inactive HDAC1 (HDAC1 A141A) and HDAC1 wildtype as control. A similar strategy has been used to generate transgenic mice expressing catalytic inactive HDAC1 and HDAC2 and resulted in significantly reduced HDAC activity and a transdominant negative effect, respectively 76. Using FuGene as a transfection reagent, constructs harboring FLAG-tagged HDAC1 variants were integrated into the AAVS1 safe-harbor locus of SZ95 sebocytes, enabling stable exogenous expression, as confirmed by Western blotting (**Figure 33**, **Figure 35**). In total, 20 cell lines were successfully generated. According to a PubMed literature search, this is the first report of SZ95 sebocyte cell lines engineered to stably express a gene of interest.

4.5.1 Investigation of co-repressor complex formation and histone deacetylase activity in cell lines expressing catalytically inactive HDAC1

Functional validation of the knock-in clones by FLAG immunoprecipitation coupled with the deacetylase activity assay was used to investigate the catalytic activity of different HDAC1 variants. FLAG-IP samples from WT clones displayed the highest activity, consistent with enrichment of a competently catalytically active FLAG-tagged HDAC1 protein, while FLAG-negative control clones showed only background-level signal in the IP, consistent with the absence of a FLAG-tagged HDAC1 for immunoprecipitation. FLAG-IP samples from catalytically inactive H141A clones displayed intermediate activity, reduced relative to WT clones but detectably above background, rather than the complete absence of activity that would be expected if the H141A allele were the only HDAC1 species present (**Figure 37**, **Figure 38**). This intermediate activity directly reflects the heterozygous nature of the cellular system used: in addition to HDAC1H141A, the endogenous catalytically active HDAC1 allele as well as HDAC2 were co-immunoprecipitated by Flag IP, thereby contributing to residual deacetylase activity. Additionally, deacetylase activity assays performed on total extracts revealed no significant differences in activity between cell lines expressing HDAC1 wildtype, HDAC1 H141A and

control cell lines (**Figure 37**). This indicates, that although inactive HDAC1 is present, its presence is not sufficient to cause significant changes in overall cellular HDAC activity, which may reflect the combined activity from endogenous HDAC1, HDAC2 and perhaps HDAC3.
Western blot analysis of FLAG IP revealed that Sin3A, CoREST, MTA2, and Sap30 (three distinct co-repressor scaffolds) were co-precipitated with the FLAG-H141A protein (**Figure 54**, **Figure 55**). Critically, the extent of co-precipitation was comparable between H141A and wild-type clones, indicating that substitution of the catalytic histidine residue does not destabilize complex assembly or reduce the affinity of HDAC1 for its co-repressor partners. This is an important mechanistic distinction from genetic knockout strategies, in which complete loss of HDAC1 protein has been shown to destabilize complex subunits including Sin3A, MTA1, and MTA2, thereby confounding the interpretation of downstream phenotypes 41. By preserving complex integrity while selectively abolishing deacetylase activity, the H141A knock-in strategy ensures that any phenotypic differences observed between H141A and wild-type clones in lipid accumulation, lipid related genes expression, or chromatin state, can be attributed specifically to the loss of HDAC1 catalytic function, rather than to broader disruption of co-repressor stoichiometry or complex-dependent gene regulatory functions.

4.5.2 Investigation of global changes of histone acetylation

Previous work in our lab showed that inhibition of class I HDACs by MS-275 or expression of catalytically inactive HDAC1 in HAP1 cells leads to global increases in histone acetylation, including H2BK5ac and H3K27ac 39. To determine whether this also occurs in sebocytes, two independent cell lines expressing HDAC1 H141A were compared with control cell lines lacking transgene expression. Immunofluorescence analyses of H2BK5ac and H3K27ac revealed no significant increase in basal levels of signal intensity in HDAC1 H141A-expressing sebocytes (**Figure 44**, **Figure 45**, **Figure 46**). These results indicate that expression of one allele of catalytically inactive HDAC1 is not sufficient to induce global changes in histone acetylation in sebocytes. To further increase the effect of catalytic inactive HDAC1, additional knockdown of endogenous HDAC1 or knockdown of HDAC2 would be possible options.
The absence of detectable differences in H2BK5ac and H3K27ac signal between catalytically inactive KI clones and FLAG-negative control clones is consistent with the heterozygous nature of the knock-in system. Since one endogenous catalytically active HDAC1 allele is retained in the KI clones, total cellular HDAC1 deacetylase activity is only partially reduced rather than abolished, and any resulting changes in histone acetylation at specific genomic loci are unlikely to be of sufficient magnitude to produce a detectable shift in global bulk acetylation levels as assessed by immunofluorescence. The absence of overt global acetylation changes does not argue against a functional role for HDAC1 catalytic activity at lipogenic loci but rather highlights the needed superior resolution of CUT&RUN over immunofluorescence for detecting locus-specific chromatin changes in this experimental system.

4.5.3 Analysis of endogenous HDAC1 and HDAC2 as well as lipid-associated proteins in transgenic sebocyte cell lines

Western blot analysis of the generated clones confirmed that this strategy was effective in generating the heterozygous clones. In contrast to the reciprocal upregulation consistently observed following siRNA-mediated HDAC1 knockdown, HDAC2 protein levels were comparable across FLAG-positive catalytically inactive clones and FLAG-negative control clones under basal conditions (**Figure 33** and **Figure 35**), indicating that introduction of the HDAC1H141A allele did not trigger compensatory HDAC2 upregulation. This result directly demonstrates that the compensatory response is driven by loss of HDAC1 protein and its

associated complex occupancy rather than by loss of HDAC1 catalytic activity and validates the catalytic knock-in system as a tool that separates the enzymatic function from the structural role. Consequently, phenotypic differences observed between catalytically inactive and control clones in downstream experiments can be attributed specifically to the reduction of HDAC1 deacetylase activity, rather than to secondary effects arising from co-repressor complex destabilization.

When protein levels of cell lines expressing different HDAC1 variants were compared WT clones displaying stronger FLAG-tagged HDAC1 signal than the catalytically inactive clones. This likely reflects that the WT and H141A clones were independently selected for clonal populations derived from separate transfection events. Differences in transgene expression between clones most likely reflect clonal heterogeneity or the epigenetic state at the AAVS1 locus at the time of selection, rather than any intrinsic property of the H141A mutation. Alternatively, clones expressing high levels of HDAC1 H141A may have been negatively selected, as the catalytically inactive form could be harmful to the cell, particularly when expressed at elevated levels.

Fatty acid synthase (FAS) protein levels increased upon insulin+TO901317 stimulation in both FLAG-negative control and FLAG-positive catalytically inactive clones (**Figure 56**), confirming that, following the generation of SZ95 cell lines, which includes selection and propagation of cell clones for at least 20 - 25 doublings after clonal dilution, retain lipogenic competence and treatment responsiveness. This is a necessary prerequisite for attributing any downstream phenotypic differences to the H141A allele rather than to a general impairment of lipid metabolism.

The magnitude of FAS induction upon insulin+TO901317 treatment appeared bigger in the FLAG-positive catalytically inactive clones than in the FLAG-negative control clones, this difference being further corroborated by immunofluorescent staining (**Figure 47**, **Figure 48**, **Figure 49**, **Figure 50**). In FLAG-negative control clones, FAS signal was close to absent across all treatment conditions, whereas FLAG-positive H141A clones displayed a considerably stronger signal that was also treatment-dependent (weakest under DMSO, moderately increased under insulin+TO901317 or MS-275 alone, and most pronounced under the combined insulin+TO901317+MS-275 condition), consistent with the activation of the lipogenic program under hormonal stimulation and HDAC inhibition. This pattern closely mirrors the lipid accumulation observed by ORO quantification and the FAS protein induction detected by Western blot analysis in parental SZ95 sebocytes, supporting the interpretation that the KI clones faithfully recapitulate the lipogenic responsiveness of the parental cell line and that the treatment-dependent chromatin and transcriptional changes observed in this system reflect a biologically relevant activation of the FASN-dependent lipogenic program. Together, these observations suggest that the partial reduction in HDAC1 catalytic activity conferred by the H141A knock-in allele is sufficient to amplify the transcriptional activation of FASN under lipogenic conditions, and that complete pharmacological inhibition of residual class I HDAC activity by MS-275 drives this further, producing the maximal induction observed under the triple combination.

5 CONCLUSION AND OUTLOOK

The present study investigated the role of HDAC1 catalytic activity in the epigenetic regulation of lipid metabolism in human SZ95 sebocytes, combining chemical perturbation, genetic engineering, and chromatin-level profiling to address this question across three complementary experimental levels.

At the chemical level, combined treatment with insulin, the LXR agonist TO901317, and the class I HDAC inhibitor MS-275 produced the strongest induction of lipid droplet accumulation and upregulation of lipid-associated proteins, including SREBP-1, SCD, and FAS, consistent with convergent activation of the canonical insulin/PI3K/Akt/mTORC1/SREBP-1 lipogenic axis and epigenetic reinforcement through class I HDAC inhibition. The partial rescue of lipid accumulation by the p300 HAT inhibitor A-485 demonstrated that p300 catalytic activity is required, at least in part, for the MS-275-associated lipogenic phenotype, suggesting that the balance between p300-mediated acetylation and HDAC1-mediated deacetylation at lipogenic gene promoters represents a functionally relevant regulatory axis in SZ95 sebocytes. siRNA-mediated knockdown of HDAC1, HDAC2, and HDAC3 was confirmed to be effective at the protein level, with significant reductions in each target achieved individually and in combination. However, assessment of lipid accumulation by ORO staining revealed only a minor increase in lipid droplet formation, without the pronounced effect observed following MS-275 treatment. This blunted response is likely attributable to the co-repressor complex dependency discussed above: loss of one paralog stabilizes the other through increased incorporation into co-repressor complexes, thereby partially sustaining deacetylase activity within Sin3, NuRD, and CoREST scaffolds even under combined knockdown conditions. Together, these observations highlight a fundamental limitation of knockdown-based approaches for isolating isoform-specific catalytic contributions in this context and motivated a change in experimental strategy. Rather than depleting HDAC1 protein, which perturbs complex stoichiometry and triggers compensatory responses, heterozygous HDAC1 H141A knock-in SZ95 cells were generated to selectively diminish catalytic activity while preserving protein levels and co-repressor complex integrity.

At the chromatin level, CUT&RUN profiling of H3K4me3 in SZ95 cells revealed treatment-dependent changes in promoter-associated chromatin states at key lipogenic loci. At the SREBF1 locus, combination treatment induced a second upstream H3K4me3 peak in addition to the constitutively active canonical promoter signal, consistent with activation of the LXR-responsive alternative SREBP-1c promoter. At the FASN and SCD loci, H3K4me3 signal was enhanced above an already active baseline, indicative of further transcriptional activation through convergent LXR and SREBP-1 mediated signaling inputs. At the ABCA1 locus, combination treatment induced a sharp de novo H3K4me3 peak from a nearly absent baseline, representing the clearest example of treatment-dependent promoter activation and consistent with direct LXR target regulation. In contrast, the loci DLX2, ZNF713, and EOLA2 did not display increased H3K4me3 signal under combination treatment, supporting the specificity of the chromatin changes observed at lipogenic gene loci.

To overcome these limitations, stable SZ95 cell lines expressing FLAG-tagged wild-type HDAC1 or the catalytically inactive HDAC1 H141A variant were generated via CRISPR/Cas9-mediated knock-in at the AAVS1 safe-harbor locus. Functional validation by FLAG immunoprecipitation and deacetylase activity assays confirmed that WT clones retained robust HDAC1 enzymatic activity, while H141A clones displayed reduced but not abolished activity, consistent with the heterozygous nature of the knock-in and retention of the endogenous catalytically active HDAC1 allele. Importantly, the compensatory HDAC2 upregulation observed upon siRNA-mediated HDAC1 knockdown was not triggered by the catalytically inactive HDAC1 allele

under basal conditions, supporting the interpretation that compensation is driven by loss of HDAC1 protein rather than loss of its catalytic activity.

Taken together, these findings support a convergent epigenetic model in which HDAC1 catalytic activity normally restrains promoter-associated histone acetylation at lipogenic gene loci in human sebocytes. Perturbation of this activity through chemical inhibition, siRNA-mediated knockdown, or partial catalytic inactivation via the H141A allele, allow p300-dependent acetylation to persist at these loci, thereby facilitating a transcriptionally permissive chromatin state that supports activation of the SREBP-1-driven lipogenic program. The concurrent activation of LXR signaling by TO901317 provides an additional transcriptional input at a subset of these loci, including SREBF1 and ABCA1, amplifying the chromatin-level response. This model positions HDAC1 as an epigenetic gatekeeper of sebaceous lipogenesis, whose partial inactivation is sufficient to shift the balance toward a hyperacetylated, pro-lipogenic chromatin state at key regulatory loci.

Several important questions remain to be addressed to extend and validate these findings. The heterozygous nature of the HDAC1 H141A KI represents a central limitation of the current system, as the retained endogenous WT allele provides residual catalytic activity that partially buffers chromatin-level changes and complicates the attribution of observed phenotypes specifically to loss of HDAC1 enzymatic function. Generation of homozygous HDAC1 H141A KI clones would be an essential next step to fully separate catalytic from structural contributions and to determine whether complete inactivation of HDAC1 enzymatic activity is sufficient to drive the lipogenic phenotype in the absence of pharmacological HDAC inhibition. Additionally, transcriptome-wide RNA-seq analysis in WT and H141A clones under lipogenic stimulation would allow validation of the chromatin changes observed by CUT&RUN at the transcriptional output level and would provide an assessment of the full gene expression program regulated by HDAC1 catalytic activity in this system. Lipidomic profiling of HDAC1 H141A versus HDAC1 WT clones under treatment conditions would further allow assessment of whether the observed transcriptional and chromatin changes translate into compositional differences in sebaceous lipid output, which is directly relevant to the pathogenesis of sebaceous gland disorders such as acne vulgaris. Together, these experiments would consolidate the mechanistic model proposed here and establish the translational relevance of HDAC1-dependent epigenetic regulation of sebaceous lipogenesis as a potential therapeutic target axis in sebaceous gland pathology.

6 BIBLIOGRAPHY

1. Goldberg, A. D., Allis, C. D. & Bernstein, E. Epigenetics: A Landscape Takes Shape. *Cell* vol. 128 635–638 Preprint at https://doi.org/10.1016/j.cell.2007.02.006 (2007).
2. Gibney, E. R. & Nolan, C. M. Epigenetics and gene expression. *Heredity* vol. 105 4–13 Preprint at https://doi.org/10.1038/hdy.2010.54 (2010).
3. Chakrabarti, S. K. & Chattopadhyay, D. Expanding Role of Epigenetics in Human Health and Disease. *Explor. Res. Hypothesis Med.* **000**, 000–000 (2024).
4. Felsenfeld, G. A brief history of epigenetics. *Cold Spring Harb. Perspect. Biol.* **6**, (2014).
5. Buljubasic, A. M. & Abu-Shamma, R. Epigenetics. *Yale Journal of Biology and Medicine* **98**, 77–78 (2025).
6. Shi, Y. Taking Epigenetics Center Stage. *Cell* **128**, 639–640 (2007).
7. Waddington, C. H. The epigenotype. 1942. *Int. J. Epidemiol.* **41**, 10–3 (2012).
8. Surani, M. A., Hayashi, K. & Hajkova, P. Genetic and Epigenetic Regulators of Pluripotency. *Cell* vol. 128 747–762 Preprint at https://doi.org/10.1016/j.cell.2007.02.010 (2007).
9. Mueller, S. A., Merondun, J., Lečić, S. & Wolf, J. B. W. Epigenetic variation in light of population genetic practice. *Nature Communications* **16**, (2025).
10. Agbleke, A. A. *et al.* Advances in Chromatin and Chromosome Research: Perspectives from Multiple Fields. *Molecular Cell* vol. 79 881–901 Preprint at https://doi.org/10.1016/j.molcel.2020.07.003 (2020).
11. Laxmi Narayan Mishra, Christophe Thiriet & Dileep Vasudevan. Chromatin structure and function. *Frontiers in Genetics and Frontiers in Cell and Developmental Biology* https://doi.org/10.3389/978-2-83250-785-8 (2022) doi:10.3389/978-2-83250-785-8.
12. Cavalli, G. & Heard, E. Advances in epigenetics link genetics to the environment and disease. *Nature* vol. 571 489–499 Preprint at https://doi.org/10.1038/s41586-019-1411-0 (2019).
13. Etier, A., Dumetz, F., Chéreau, S. & Ponts, N. Post-Translational Modifications of Histones Are Versatile Regulators of Fungal Development and Secondary Metabolism. *Toxins* vol. 14 Preprint at https://doi.org/10.3390/toxins14050317 (2022).
14. McGinty, R. K. & Tan, S. Nucleosome structure and function. *Chemical Reviews* vol. 115 2255–2273 Preprint at https://doi.org/10.1021/cr500373h (2015).
15. Romanò, A., Pagiatakis, C., Gornati, R., Bernardini, G. & Papait, R. Epigenetics: A link between toxicants and diseases. *iScience* vol. 28 Preprint at https://doi.org/10.1016/j.isci.2025.112613 (2025).
16. Ostaiza-Cardenas, J. *et al.* Epigenetic modulation by life–style: advances in diet, exercise, and mindfulness for disease prevention and health optimization. *Front. Nutr.* **12**, (2025).
17. Bernstein, B. E., Meissner, A. & Lander, E. S. The Mammalian Epigenome. *Cell* vol. 128 669–681 Preprint at https://doi.org/10.1016/j.cell.2007.01.033 (2007).
18. Bowman, G. D. & Poirier, M. G. Post-translational modifications of histones that influence nucleosome dynamics. *Chemical Reviews* vol. 115 2274–2295 Preprint at https://doi.org/10.1021/cr500350x (2015).
19. Patel, A. B., He, Y. & Radhakrishnan, I. Histone acetylation and deacetylation – Mechanistic insights from structural biology. *Gene* **890**, (2024).
20. Betts J. Gordon *et al. Anatomy and Physiology*.

21. Sokolova, V., Sarkar, S. & Tan, D. Histone variants and chromatin structure, update of advances. *Computational and Structural Biotechnology Journal* vol. 21 299–311 Preprint at https://doi.org/10.1016/j.csbj.2022.12.002 (2023).
22. Biterge, B. A Mini Review on Post-Translational Histone Modifications. *MOJ Cell Science & Report* **3**, (2016).
23. Su, Z. & Denu, J. M. Reading the Combinatorial Histone Language. *ACS Chemical Biology* vol. 11 564–574 Preprint at https://doi.org/10.1021/acschembio.5b00864 (2016).
24. Bilokapic, S., Strauss, M. & Halic, M. Structural rearrangements of the histone octamer translocate DNA. *Nat. Commun.* **9**, (2018).
25. Sadakierska-Chudy, A. & Filip, M. A Comprehensive View of the Epigenetic Landscape. Part II: Histone Post-translational Modification, Nucleosome Level, and Chromatin Regulation by ncRNAs. *Neurotoxicity Research* vol. 27 172–197 Preprint at https://doi.org/10.1007/s12640-014-9508-6 (2015).
26. Liu, R. *et al.* Post-translational modifications of histones: Mechanisms, biological functions, and therapeutic targets. *MedComm* vol. 4 Preprint at https://doi.org/10.1002/mco2.292 (2023).
27. Yang, S., Chen, L., Lin, M., Shen, C. & Reheman, A. Histone Modifications as Individual-Specific Epigenetic Regulators: Opportunities for Forensic Genetics and Postmortem Analysis. *Genes* vol. 16 Preprint at https://doi.org/10.3390/genes16080940 (2025).
28. Liu, R. *et al.* Post-translational modifications of histones: Mechanisms, biological functions, and therapeutic targets. *MedComm* vol. 4 Preprint at https://doi.org/10.1002/mco2.292 (2023).
29. Chen, H. P., Zhao, Y. T. & Zhao, T. C. *Histone Deacetylases and Mechanisms of Regulation of Gene Expression (Histone Deacetylases in Cancer)*.
30. Xu, L. *et al.* Decoding Epigenetic Switches: How Histone Acetylation/Deacetylation Regulates Mononuclear/Macrophage Fate in Bone Disorders. *International Journal of Biological Sciences* vol. 22 601–617 Preprint at https://doi.org/10.7150/ijbs.125544 (2026).
31. Park, S. Y. & Kim, J. S. A short guide to histone deacetylases including recent progress on class II enzymes. *Experimental and Molecular Medicine* vol. 52 204–212 Preprint at https://doi.org/10.1038/s12276-020-0382-4 (2020).
32. Carrier, F. & Marlene, S. *Chromatin Modulation by Histone Deacetylase Inhibitors: Impact on Cellular Sensitivity to Ionizing Radiation*. *Mol Cell Pharmacol* vol. 5 (2013).
33. Zhao, M., Tao, Y. & Peng, G. H. The role of histone acetyltransferases and histone deacetylases in photoreceptor differentiation and degeneration. *International Journal of Medical Sciences* vol. 17 1307–1314 Preprint at https://doi.org/10.7150/ijms.43140 (2020).
34. Shin, H. S., Zouboulis, C. C., Kim, M. K., Lee, D. H. & Chung, J. H. Minocycline suppresses lipogenesis via inhibition of p300 histone acetyltransferase activity in human SZ95 sebocytes. *Journal of the European Academy of Dermatology and Venereology* **36**, 1325–1333 (2022).
35. Filippakopoulos, P. *et al.* Histone Recognition and Large-Scale Structural Analysis of the Human Bromodomain Family. *Cell* **149**, 214–231 (2012).
36. Josling, G. A., Selvarajah, S. A., Petter, M. & Duffy, M. F. The Role of Bromodomain Proteins in Regulating Gene Expression. *Genes (Basel).* **3**, 320–343 (2012).

37. Eberharter, A. & Becker, P. B. *Review Histone Acetylation: A Switch between Repressive and Permissive Chromatin Second in Review Series on Chromatin Dynamics*. (2002).
38. Hess, L., Moos, V. & Seiser, C. Development of a Cellular Model Mimicking Specific HDAC Inhibitors. in *Methods in Molecular Biology* vol. 2589 51–73 (Humana Press Inc., 2023).
39. Hess, L. *et al.* A toolbox for class I HDACs reveals isoform specific roles in gene regulation and protein acetylation. *PLoS Genet.* **18**, (2022).
40. Seto, E. & Yoshida, M. Erasers of histone acetylation: The histone deacetylase enzymes. *Cold Spring Harb. Perspect. Biol.* **6**, (2014).
41. Winter, M. *et al.* Divergent roles of HDAC1 and HDAC2 in the regulation of epidermal development and tumorigenesis. *EMBO Journal* **32**, 3176–3191 (2013).
42. Chiocca, S. & Segré, C. V. Regulating the regulators: The post-translational code of class i HDAC1 and HDAC2. *Journal of Biomedicine and Biotechnology* vol. 2011 Preprint at https://doi.org/10.1155/2011/690848 (2011).
43. Ma, P. & Schultz, R. M. HDAC1 and HDAC2 in mouse oocytes and preimplantation embryos: Specificity versus compensation. *Cell Death Differ.* **23**, 1119–1127 (2016).
44. Brunmeir, R., Lagger, S. & Seiser, C. Histone deacetylase 1 and 2-controlled embryonic development and cell differentiation. *International Journal of Developmental Biology* vol. 53 275–289 Preprint at https://doi.org/10.1387/ijdb.082649rb (2009).
45. Curcio, A., Rocca, R., Alcaro, S. & Artese, A. The Histone Deacetylase Family: Structural Features and Application of Combined Computational Methods. *Pharmaceuticals* vol. 17 Preprint at https://doi.org/10.3390/ph17050620 (2024).
46. Bhaskara, S. Histone deacetylases 1 and 2 regulate DNA replication and DNA repair: Potential targets for genome stability-mechanism-based therapeutics for a subset of cancers. *Cell Cycle* **14**, 1779–1785 (2015).
47. Jurkin, J. *et al.* Distinct and redundant functions of histone deacetylases HDAC1 and HDAC2 in proliferation and tumorigenesis. *Cell Cycle* vol. 10 406–412 Preprint at https://doi.org/10.4161/cc.10.3.14712 (2011).
48. Hagelkruys, A. *et al.* A single allele of Hdac2 but not Hdac1 is sufficient for normal mouse brain development in the absence of its paralog Europe PMC Funders Group. *Development* **141**, 604–616 (2014).
49. Lotfollahi, Z. The anatomy, physiology and function of all skin layers and the impact of ageing on the skin. *Wound Practice and Research* vol. 32 6–10 Preprint at https://doi.org/10.33235/wpr.32.1.6-10 (2024).
50. Yousef Hani; Alhajj Mandy; Fakoya Adegbenro O. ; Sharma Sandeep. *Anatomy, Skin (Integument), Epidermis*.
51. Lim, K. M. Skin epidermis and barrier function. *International Journal of Molecular Sciences* vol. 22 1–3 Preprint at https://doi.org/10.3390/ijms22063035 (2021).
52. Lefèvre-Utile, A., Braun, C., Haftek, M. & Aubin, F. Five functional aspects of the epidermal barrier. *Int. J. Mol. Sci.* **22**, (2021).
53. El-Safadi, S., Dreyer, T., Oehmke, F. & Muenstedt, K. Management of adult primary vulvar Langerhans cell histiocytosis: review of the literature and a case history. *European Journal of Obstetrics & Gynecology and Reproductive Biology* **163**, 123–128 (2012).
54. Zouboulis Christos C. Sebaceous gland receptors. (2009).

55. Mosca, S., Ottaviani, M., Briganti, S., Di Nardo, A. & Flori, E. The Sebaceous Gland: A Key Player in the Balance Between Homeostasis and Inflammatory Skin Diseases. *Cells* vol. 14 Preprint at https://doi.org/10.3390/cells14100747 (2025).
56. Hoover Ezra; Aslam Sanah; Krishnamurthy Karthik. *Physiology, Sebaceous Glands*.
57. Okoro, O. E., Camera, E., Flori, E. & Ottaviani, M. Insulin and the sebaceous gland function. *Front. Physiol.* **14**, (2023).
58. Picardo Mauro, O. M. C. E. M. A. Sebaceous gland lipids. (2009).
59. Tóth, B. I. *et al.* Transient Receptor Potential Vanilloid-1 Signaling as a Regulator of Human Sebocyte Biology. *Journal of Investigative Dermatology* **129**, 329–339 (2009).
60. Törőcsik, D. *et al.* Genome wide analysis of TLR1/2- and TLR4-activated SZ95 sebocytes reveals a complex immune-competence and identifies serum amyloid A as a marker for activated sebaceous glands. *PLoS One* **13**, e0198323 (2018).
61. Zouboulis, C. C., Seltmann, H., Neitzel, H. & Orfanos, C. E. *Establishment and Characterization of an Immortalized Human Sebaceous Gland Cell Line (SZ95) 1*. *J Invest Dermatol* vol. 113 (1999).
62. Xia, L., Zouboulis, C. C. & Ju, Q. Culture of human sebocytes in vitro. *Dermatoendocrinol.* **1**, 92–95 (2009).
63. Mosca, S., Ottaviani, M., Briganti, S., Di Nardo, A. & Flori, E. The Sebaceous Gland: A Key Player in the Balance Between Homeostasis and Inflammatory Skin Diseases. *Cells* vol. 14 Preprint at https://doi.org/10.3390/cells14100747 (2025).
64. Miner, K. *et al.* Lipid Dysregulation in Sebaceous Gland Disorders and the Impact of Sphingolipid Metabolism on Acne Pathogenesis. *Cureus* https://doi.org/10.7759/cureus.82463 (2025) doi:10.7759/cureus.82463.
65. Horton, J. D., Goldstein, J. L. & Brown, M. S. SREBPs: activators of the complete program of cholesterol and fatty acid synthesis in the liver. *Journal of Clinical Investigation* **109**, 1125–1131 (2002).
66. DeBose-Boyd, R. A. & Ye, J. SREBPs in Lipid Metabolism, Insulin Signaling, and Beyond. *Trends in Biochemical Sciences* vol. 43 358–368 Preprint at https://doi.org/10.1016/j.tibs.2018.01.005 (2018).
67. Xu, X., So, J. S., Park, J. G. & Lee, A. H. Transcriptional control of hepatic lipid metabolism by SREBP and ChREBP. *Semin. Liver Dis.* **33**, 301–311 (2013).
68. Shin, H. S. *et al.* Histone deacetylase 1 reduces lipogenesis by suppressing srebp1 transcription in human sebocyte cell line sz95. *Int. J. Mol. Sci.* **22**, (2021).
69. Hemmings, B. A. & Restuccia, D. F. PI3K-PKB/Akt pathway. *Cold Spring Harb. Perspect. Biol.* **4**, (2012).
70. He, Y. *et al.* Targeting PI3K/Akt signal transduction for cancer therapy. *Signal Transduction and Targeted Therapy* vol. 6 Preprint at https://doi.org/10.1038/s41392-021-00828-5 (2021).
71. Semple, R. K., Chatterjee, V. K. K. & O'Rahilly, S. PPARγ and human metabolic disease. *Journal of Clinical Investigation* vol. 116 581–589 Preprint at https://doi.org/10.1172/JCI28003 (2006).
72. Ahmadian, M. *et al.* Pparγ signaling and metabolism: The good, the bad and the future. *Nat. Med.* **19**, 557–566 (2013).
73. Melnik, B. C. Acne Transcriptomics: Fundamentals of Acne Pathogenesis and Isotretinoin Treatment. *Cells* vol. 12 Preprint at https://doi.org/10.3390/cells12222600 (2023).
74. Lasko, L. M. *et al.* Discovery of a selective catalytic p300/CBP inhibitor that targets lineage-specific tumours. *Nature* **550**, 128–132 (2017).

75. Kan Guerreiro Do Rosario, A. *Tthe Mechanisms Involved in the Downregulation of Host Histone Deacetylase 1 and 2 during Influenza a Virus Infection*. https://ourarchive.otago.ac.nz/esploro/outputs/graduate/The-mechanisms-involved-in-the-downregulation/9926503773901891 (2023).
76. Hagelkruys, A. *et al.* Essential Nonredundant Function of the Catalytic Activity of Histone Deacetylase 2 in Mouse Development. *Mol. Cell. Biol.* **36**, 462–474 (2016).
77. Kelly, R. D. W. & Cowley, S. M. The physiological roles of histone deacetylase (HDAC) 1 and 2: Complex co-stars with multiple leading parts. in *Biochemical Society Transactions* vol. 41 741–749 (2013).
78. Nunn, A. D. G. *et al.* The histone deacetylase inhibiting drug Entinostat induces lipid accumulation in differentiated HepaRG cells. *Sci. Rep.* **6**, (2016).